D I P L O M A R B E I T

Finite Element Simulation of Berkovich Indentation in Bone

ausgeführt zum Zwecke der Erlangung des akademischen Grades eines Diplom-Ingenieurs
unter der Leitung von

Univ. Prof. Dipl.-Ing. Dr. techn. Philippe K. Zysset
Institut für Leichtbau und Struktur-Biomechanik, E317

eingereicht an der Technischen Universität Wien
Fakultät für Maschinenwesen und Betriebswissenschaften

von

Johann Jakob Schwiedrzik

Wien, am 18.8.2010

Abstract

Research on the mechanical properties of bone tissue has been done since the first half of the 20th century. In recent years, the interest in the micromechanical properties of bone has increased due to the development of depth-sensing nanoindentation. Modern preventive and therapeutic methods for diseases like osteoporosis rely on the results of the research on micromechanics of bone and its influence on cell-mediated adaption processes. Osteoporosis is a severe disease affecting the strength of the skeleton. According to Statistik Austria, one out of four women above the age of 60 suffers from osteoporosis. Nanoindentation offers the possibility to inspect elastic and post-yield properties of bone tissue. The main aim of this study is to determine the influence of the material behavior of the tested specimen on the accuracy of the experimental results. A finite element (FE) model of a conical and a Berkovich indentation were developed and validated. Different material models were defined and subsequently indented by a rigid indenter. The elastic properties were extracted from the indentation curves, allowing to quantify the systematic error made when using the method of Oliver and Pharr [OP92] assuming intact unloading elasticity. Also, the influence of the accumulation of microdamage was assessed by using an elasto-plastic material model with damage [Zys94] for bone. A user subroutine defining the constitutive behavior was implemented in Fortran. Time and rate dependent effects such as viscosity were neglected in the course of this study. Detailed and extensive verification showed that the developed FE models are able to simulate indentations in a wide range of different material models with sufficient accuracy.

The results of this study indicate that the indentation modulus is insensitive to indentation depth for elastic materials. The method of Oliver and Pharr does not account for finite tip radii. However, this effect diminishes with increasing indentation depth. There is a stiffening effect based on the Poisson ratio reported by Poon [PRR08b]. He implemented an empirical formula that coincides with the data of this study. This effect is also described by Hay et al [HBP99]. According to Hay, there is a systematic error due to radial displacements of the surface points inside the contact area not accounted for in the data analysis. For materials featuring plasticity there is clear indication in the data that the indentation depth has an effect on the measured indentation modulus. For elastic ideal plastic materials the initial unloading phase is purely elastic [PRR08b]. However, there is a serious overestimation of the indentation modulus due to material pile-up. Bolshakov et al reported similar results [BP98] for materials with a ratio h_f/h_{max} larger than 0.7. In this study, h_f/h_{max} was larger than 0.7 for all elasto-plastic bone models. Poon was able to show that the error of the measured modulus is smaller and a function of the Poisson ratio if the contact area is known. This suggests that the remaining error is due to residual stresses in the plastic imprint [PRR08b] and radial displacements of the surface points in the contact area [HBP99]. A model of the 3D geometry of the Berkovich indenter was developed. It was shown that while the conical indenter is an excellent model for the Berkovich indenter in the far stress field and the structural response, the near stress and strain fields differ significantly. Also, damage accumulation was considered in an anisotropic elasto-plastic bone model. The shape of the indentation curves were qualitatively similar to experimental results of indentations on bone. However, the measured indentation modulus was considerably smaller than expected (45 to 51% in modulus depending on the indentation direction and hardening function). The cumulated damage ranged from 25% to 99%. The ratio h_f/h_{max} was smaller than 0.7 for all simulations. Bolshakov et al. [BP98] reported that the method of Oliver and Pharr works accurately for isotropic elastic ideal plastic materials if the ratio h_f/h_{max} is smaller than 0.7. This is not the case in the presence of damage. The assumption of intact unloading elasticity is not justified as the results of this study showed large damaged areas with a cumulated damage D of 0.32 to 0.99. The shape of the stress and damage fields were qualitatively similar to the results reported by Zheng et al [ZMKO10] for an isotropic elasto-plastic continuum damage model of bone. However, time- and rate dependent effects were not accounted for, therefore the indentation curves did not show creep behavior as reported for bone [ZEGEH$^+$99]. Further investigations featuring rate-dependent material models and tuning of the continuum damage models for bone are needed to get a better correlation to experimental results for bone tissue and a better understanding of the decisive processes.

Zusammenfassung

Seit der ersten Hälfte des 20. Jahrhunderts beschäftigt sich die Forschung mit den mechanischen Eigenschaften von Knochen. In den letzten Jahren hat das Interesse an der Erforschung der mikromechanischen Eigenschaften von Knochen aufgrund der Entwicklung der instrumentierten Nanoindentation stark zugenommen. Moderne Methoden zur Prävention und Therapie von Krankheiten wie Osteoporose basieren auf Kenntnissen über das mikromechanische Verhalten von Knochen und seinen Einfluss auf zellgesteuerte Adaptionsprozesse. Osteoporose ist eine schwere Krankheit, von der jede vierte Frau über 60 betroffen ist. Das Ziel dieser Studie besteht in der Bestimmung des Einflusses des Materialverhaltens der Probe auf die Genauigkeit der Messergebnisse bei der Nanoindentation. Finite Elemente (FE) Modelle eines konischen sowie eines Berkovich Indenters wurden erstellt und validiert. Verschiedene Materialmodelle wurden definiert. Die elastischen Eigenschaften wurden mit Hilfe der Indentationskurven auf Basis der Methode von Oliver und Pharr [OP92] bestimmt. Die FE Methode erlaubte so die Quantifizierung des Messfehlers aufgrund der Annahme einer intakten Elastizität in der Entlastungsphase. Durch Verwendung eines elasto-plastischen Materialmodells mit Schädigung für Knochen [Zys94] wurde der Einfluss dieses Phänomens bestimmt. Eine Subroutine wurde in Fortran implementiert. Zeit- und ratenabhängige Effekte wurden in dieser Studie vernachlässigt. Ausführliche und detaillierte Verifizierung des Modells zeigte, dass das Finite Elemente Modell Indentationen für eine Reihe von Materialien ausreichend genau zu simulieren.

Die Ergebnisse dieser Studie zeigen, dass der Indentationsmodul für elastische Materialien unabhängig von der Indentationstiefe ist. Die Methode von Oliver und Pharr vernachlässigt den Einfluss von endlichen Spitzenradien. Dieser Effekt verschwindet jedoch mit zunehmender Indentationstiefe. Weiters scheint eine Versteifung aufgrund eines Effektes der Poissonkonstante aufzutreten, der von Poon [PRR08b] in einer empirischen Formel implementiert wurde. Diese stimmt mit den Daten dieser Studie überein. Dieser Effekt wurde auch von Hay et al. beschrieben [HBP99]. Laut Hay gibt es einen systematischen Messfehler aufgrund der Vernachlässigung von radialen Verschiebungen der Punkte der Kontaktfläche zwischen Indenter und Material in der Datenanalyse. Für elasto-plastische Knochenmodelle gibt es klare Anzeichen, dass die Indentationstiefe auf den gemessenen Indentationsmodul Einfluss hat. Für elasto-plastische Materialien ist die Entlastungsphase laut Poon elastisch [PRR08b]. Allerdings tritt eine starke Überschätzung des Indentationsmoduls aufgrund von Materialanhäufungen auf. Bolshakov et al [BP98] machten ähnliche Beobachtungen für Materialien mit einem Verhältnis h_f/h_{max} grösser als 0.7. In dieser Studie lag das Verhältnis h_f/h_{max} sowohl im isotropen als auch im anisotropen Fall deutlich über 0.7. Poon zeigte, dass der Messfehler deutlich kleiner und eine Funktion der Poissonkonstante ist, wenn die Kontaktfläche bekannt ist. Das zeigt, dass die Materialanhäufungen ein wichtiger Faktor für die Überschätzung des Indentationsmoduls sind. Der verbleibende Fehler ist vermutlich durch Eigenspannungen im Abdruck [PRR08b] und radiale Verschiebungen der Punkte der Kontaktfläche [HBP99] zu erklären. Im Laufe dieser Studie wurde ein dreidimensionales Modell der Berkovichspitze entwickelt. Es konnte gezeigt werden, dass der konische Indenter eine sehr gute Annäherung der strukturellen Antwort liefert. Weiters wurde Schadensakkumulation in einem anisotropen elasto-plastischen Knochenmodell berücksichtigt. Der gemessene Indentationsmodul war deutlich geringer als erwartet. Die Unterschätzung lag bei 45% bis 51% je nach Indentationsrichtung und Verfestigungsfunktion. Der kumulierte Schaden lag zwischen 25% und 99%. Das Verhältnis h_f/h_{max} war deutlich kleiner als 0.7 in allen Simulationen. Bolshakov et al [BP98] berichteten, dass die Methode von Oliver und Pharr für isotrope elastische ideal plastische Materialien mit grosser Genauigkeit funktioniert, wenn h_f/h_{max} kleiner als 0.7 ist. Dies ist bei Schädigung des Materials nicht der Fall, wie die Ergebnisse dieser Studie zeigen. Die Annahme einer intakten Elastizität bei der Entlastung ist bei der Präsenz von starker Schädigung unter der Spitze nicht haltbar. Diese lag in dieser Studie bei bis zu 99% direkt unter der Spitze. Die Form des Spannungs- und Schädigungsfeldes war qualitativ vergleichbar mit den Ergebnissen von Zheng et al [ZMKO10] für ein isotropes elasto-plastisches Schadensmodell für Knochen. Zeit- und ratenabhängige Effekte wurden in dieser Studie vernachlässigt, weshalb die Indentationskurven kein viskoses Verhalten zeigten, das für Knochen charakteristisch ist [ZEGEH+99]. Weitere Studien unter Berücksichtigung von zeitabhängigen Materialgesetzen und Identifikation von Materialparametern für die Schädigungsmodelle sind notwendig, um eine bessere Korrelation zu experimentellen Ergebnissen an Knochen und ein tieferes Verständnis der ablaufenden Vorgänge zu erreichen.

Contents

List of Figures

List of Tables

Chapter 1

Introduction

1.1 Motivation

Research on the mechanical properties of bone tissue has been done since the first half of the 20th century, as modern medicine started to demand a more scientific approach on skeletal mechanics. Since that time, the research yielded some essential results. The mineralization and orientation of the collagen fibres influence the anisotropic tissue hardness in the bone structural unit. Also, the tissue hardness is not changed due to effects of aging or osteoporosis [ZEGEH+99]. In recent years, the interest in the micromechanical properties of bone was regained. This is due to the development of depth-sensing nanoindentation, which allows a systematic investigation of micromechanical properties at the lamellar and the bone structural unit level. The macroscopic mechanical properties of the bone tissue are influenced by composition, structure, microstructure and nanostructure [ZEGEH+99]. Modern preventive and therapeutic methods for skeletal diseases like osteoporosis rely highly on the results of the research on the micromechanics of bone and its influence on cell-mediated adaption processes [Zys09]. Osteoporosis is a severe disease affecting the strength of the skeleton. People affected by it have a highly elevated fracture risk. According to Statistik Austria, one out of four women above the age of 60 suffers from osteoporosis. Therefore a lot of effort is made to find therapies for this disease. There are other experimental methods to study the micromechanics of bone tissue, e.g. ultrasound microscopy. It has a considerably higher data throughput than nanoindentation. However, unlike ultrasound microscopy, nanoindentation offers the possibility to inspect not only elastic, but also post-yield properties of the bone tissue ([DCVV+01],[ZNO08]). This is a big advantage of this method in comparison to other methods. Therefore this field of research has been growing rapidly in the last two decades.

1.2 Nanoindentation

Nanoindentation is an important experimental technique to determine the micromechanical properties of surfaces, thin films and materials. It has also become increasingly popular in the examination of biological materials [Zys09]. In traditional mechanical testing, macroscopic specimens are fixed to a device and tested. The size of the tested volume and its characteristic lengths are very similar to the specimen size. On the other hand, in nanoindentation a diamond tip is pushed into the surface of the material. The tip displacement and the force response are measured simultaneously by the testing device. The sample volume is usually multiple scales larger than the tested volume. This makes the determination of local mechanical properties possible in contrast to homogenizing over a large sample volume. This is especially important, as the mechanical properties of biological mate-

rials may vary widely depending on the scale of the experiment (macro, meso, micro or even nano) due to hierarchical structures and inhomogeneities. A typical nanoindentation machine has four main components: A xyz-table with a sample holder that allows exact positioning of the sample, a microscope to examine the specimen, choose appropriate indentation spots and postexperimental examination, a transducer and the indenter tip. Fig. 1.1 shows a typical testing setup of the CSM Nanohardness Tester (CSM Instruments SA, Peseux, Switzerland) with a specimen mounted on the nanoindentation machine.
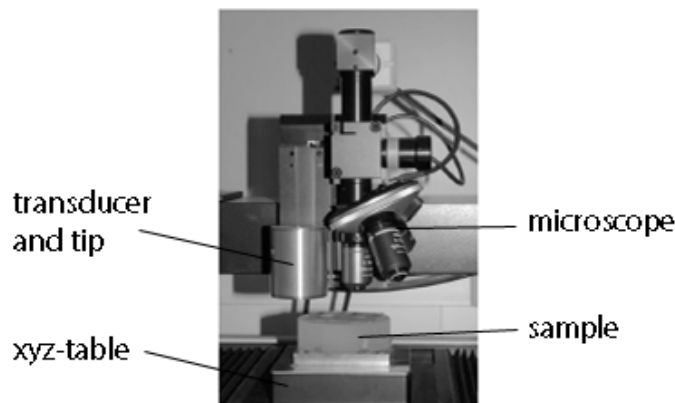
Figure 1.1: Typical testing setup of a nanoindentation experiment on the CSM Nanohardness Tester

In order to make accurate measurements, the exact position of the specimen in space has to be determined before the test. The indentation head is lowered to the surface of the specimen. It acts as a frame of reference during the experiment. Fig. 1.2 shows a scheme of the indenter head.
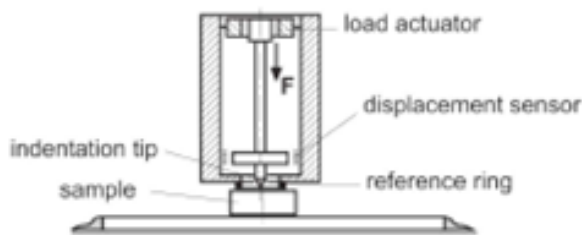
Figure 1.2: Scheme of the indenter head of the CSM Nanohardness Tester

When the tip comes into contact with the surface and performs the indentation, the material underneath deforms. Depending on the material properties, different indentation shapes will form. Therefore distinct measures are introduced that help to uniquely identify the shape of the indentation site. Fig. 1.3 shows a scheme of the deformation of the surface during the indentation experiment and the measures defining the indentation shape.
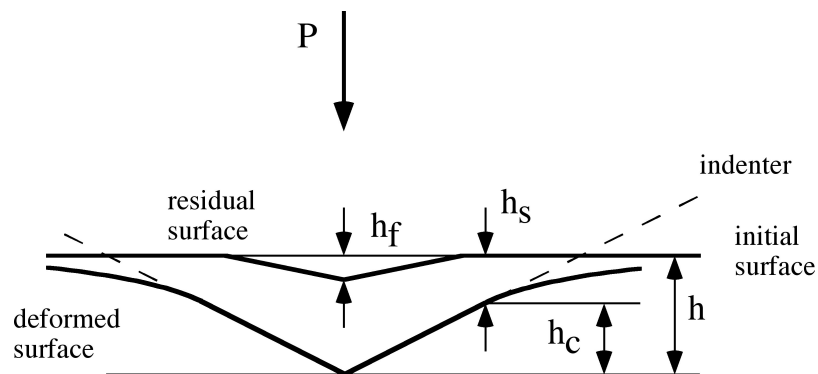
Figure 1.3: Scheme of an indentation

For the indentation of an axisymmetric body of arbitrary shape into an isotropic linearly elastic halfspace, an analytical solution was found by Sneddon [Sne48]. It can be used directly to obtain the elastic modulus if the material's Poisson's ratio is known a priori. Sneddon found that there is a quadratic relationship between the reaction force and the indentation depth. Many materials cannot be modeled as purely linear elastic solids, though. Therefore experimental techniques had to be developed in order to extract elastic properties from indentation experiments. For bone, the testing protocol usually involves a linear loading phase in load control, a hold phase with constant loading in order to minimize viscous effects on the measurements [Zys09] and a linear unloading phase. Fig. 1.4 shows a typical load-displacement curve of a nanoindentation experiment on bone.
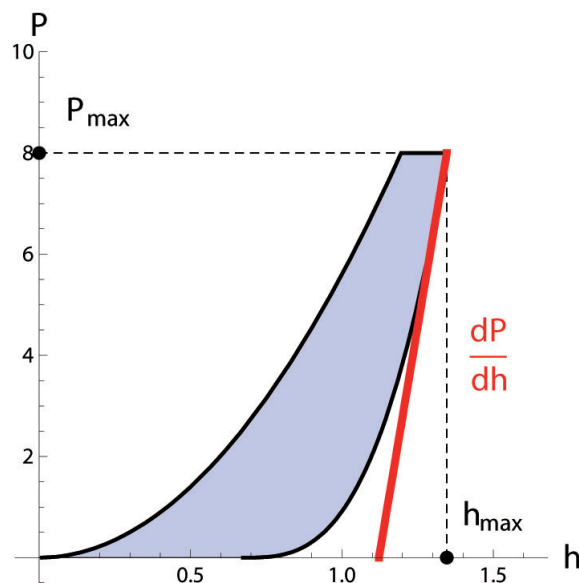
Figure 1.4: Typical load-displacement curve of an indentation experiment

One can see clearly the response of the material in the three phases of the experiment. There is a nonlinear response during the loading phase followed by creep deformation during the hold phase. This is a viscous effect that is common for bone. The unloading phase is nonlinear again. The shape of a load-displacement curve of an indentation experiment can be described by a set of

shape factors as described by Mullins et al [MBM09]. The combination of four shape factors, e.g. maximum force, maximum indentation depth, dissipated energy and the gradient dP/dh at h_{max} is usually enough to uniquely identify one indentation curve. It is however very difficult to extract unique nonlinear postelastic mechanical properties from one indentation curve, as the indentation in multiple materials with significantly different properties might result in very similar experimental indentation curves. This effect was described by Chen et al [COZC07], who speaks of mystical materials, as unique nonlinear properties cannot be extracted. Therefore, the following method aims at finding the elastic properties of the tested material without considering any nonlinear effects.

For elasto-plastic materials, plastic deformation takes place during the loading phase. The extent of the plastic deformation depends on the indenter shape. For sharp indenters like conical or Berkovich indenters, the onset of plasticity is immediate. Therefore there is a superposition of local elastic and plastic material behaviour under the indenter tip. It is very hard to distinguish the two effects in the load-displacement curve. However, it is believed that the beginning of the unloading curve is purely elastic (as stated by Oliver and Pharr [OP92]). Therefore it is possible to extract unique elastic properties from this part of the indentation curve. The equations required to extract the elastic modulus are presented in the following chapter describing the existing analytical solutions of the Boussinesq problem.

1.3 Rigid punch on an elastic halfspace

1.3.1 Isotropic material

The analytical solution to a penetration of an elastic halfspace by a rigid punch whose profile is described by the function $f(x)$ was found by Sneddon [Sne48]. The total force needed to penetrate to a depth of h_e is given by the equation

$$P = \frac{4Ga}{1-\nu} \int_0^{h_e} \frac{x^2 f'(x) dx}{\sqrt{1-x^2}} \tag{1.1}$$

In the special case of a conical indenter this equation becomes

$$P = \frac{2E \tan \alpha}{\pi(1-\nu^2)} h_e^2 \tag{1.2}$$

The method used by Oliver and Pharr [OP92] to extract the isotropic elastic modulus of a material with known Poisson ratio is based on this analytical solution. Differentiating this relationship, we get

$$\frac{dP}{dh_e} = \frac{4E \tan \alpha}{\pi(1-\nu^2)} h_e \tag{1.3}$$

The indentation depth h_{max} consists of two parts h_c and h_s as defined in Fig. 1.3:

$$h_{max} = h_c + h_s \tag{1.4}$$

The deflection at the contact perimeter h_s can be calculated by using Sneddon's expression for the deformed surface outside the area of contact [Sne48]:

$$h_s = \frac{\pi - 2}{\pi}(h - h_f) \tag{1.5}$$

Sneddon's solution only applies to purely elastic problems, therefore $(h - h_f)$ has to be used rather than h. From Sneddon's force-displacement relation, the following expression can be derived:

$$h - h_f = 2\frac{P}{dP/dh} \tag{1.6}$$

Substituting eq. (1.6) in eq. (1.5), the following relationship for h_s is obtained:

$$h_s = \frac{2(\pi - 2)}{\pi} \frac{P}{dP/dh} = \chi \frac{P}{dP/dh} \tag{1.7}$$

The contact depth of the indenter as defined in Fig. 1.3 can therefore be calculated by the following relationship:

$$h_c = h_{max} - \chi \frac{P|_{h_{max}}}{dP/dh_e|_{h_{max}}} \tag{1.8}$$

with $\chi = 0.72$ for a conical indenter. According to Oliver and Pharr [OP92], the projected contact area therefore becomes

$$A = \pi \tan^2 \alpha h_c^2 = 24.5 h_c^2 \tag{1.9}$$

Assuming linear elastic material behaviour, the elastic modulus for an isotropic material can be calculated from an indentation curve by the relationship

$$E = \frac{1}{2\beta} \frac{dP}{dh_e} \frac{\sqrt{\pi}}{\sqrt{A}} (1 - \nu^2) \tag{1.10}$$

In this case, β is an empirical correction factor that depends on the tip geometry. It is 1.0 for a conical indenter and 1.034 for a Berkovich indenter. Following the suggestions of Oliver and Pharr [OP92], the elastic modulus is extracted with the help of the gradient of the unloading curve dP/dh at the maximum indentation depth h_{max}. A curve is fitted to the experimental data in order to obtain a smooth function. Then the gradient is computed at the maximum indentation depth. Thus a good approximation of the isotropic elastic modulus may be found if the Poisson ratio is known a priori. The indentation modulus can be extracted with this technique as well using the formula

$$E_{ind} = \frac{1}{2\beta} \frac{dP}{dh_e} \frac{\sqrt{\pi}}{\sqrt{A}} \tag{1.11}$$

If the indenter is not completely rigid, the measured modulus is equal to the reduced modulus E_r. It is defined by the combination of the indenter and the specimen stiffness:

$$\frac{1}{E_r} = \frac{1 - \nu_{specimen}^2}{E_{specimen}} + \frac{1 - \nu_{indenter}^2}{E_{indenter}} \tag{1.12}$$

The elastic modulus of the specimen can be computed, if the mechanical properties of the indenter are known. In this study, the indenter will be modeled as rigid and the reduced modulus E_r is therefore equal to the modulus of the specimen E_{spec}. The shape of the indentation is given by the following expression in a cylindrical coordinate system for the analytical solution of Sneddon [Sne48] as a function of z [HBP99]:

$$r(z) = z \tan \phi + \frac{1 - 2\nu}{4 - 4\nu} z (ln \frac{z \tan \phi/a}{1 + \sqrt{1 - (z \tan \phi)^2/a^2}} - \frac{1 - \sqrt{1 - (z \tan \phi)^2/a^2}}{(z \tan \phi)^2/a^2} \tag{1.13}$$

with a being the radius of the circle of contact. It is related to the contact depth h_c by

$$a = h_c \tan \phi \tag{1.14}$$

It should be noted that this shape potentially differs from the shape of an indentation of a rigid cone into an elastic half-space as stated by Hay et al [HBP99] depending on the indenter angle ϕ and the Poisson ratio of the indented material.

1.3.2 Anisotropic material

Biological tissues are mostly not isotropic continuous media, but highly hierarchical structures with anisotropic material properties. Therefore the assumption of isotropy needed for equation (1.6) to yield proper results can provide a first approximation of the elastic properties only. In order to be able to extract elastic properties from indentation experiments on anisotropic materials, Swadener and Pharr [SP01] developed a new mathematical framework that allows the use of the Oliver and Pharr method [OP92].

When indenting an anisotropic material, the contact perimeter around the indenter has different depths depending on the orientation of the elastic tensor. Fig. 1.5 shows the scheme of an indentation of a conical tip into an anisotropic material.
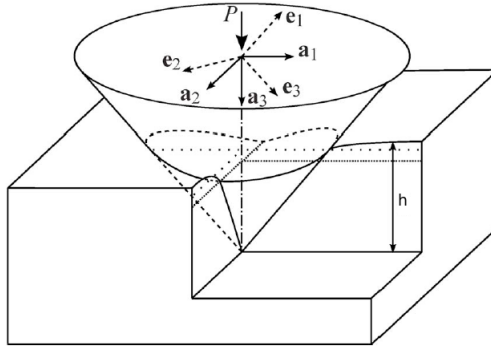
Figure 1.5: Scheme of the indentation into an anisotropic material, from Franzoso et al. [FZ09]

Therefore, according to Swadener and Pharr [SP01], for an anisotropic material the shape of the contact area is assumed to be elliptical. The area is defined as:

$$A = \pi a_1 a_2. \tag{1.15}$$

In order for the conical indentation to be self-similar, it must be proportional to h_e^2. Therefore, the contact stiffness S is linear in respect to the indentation depth in linear elasticity and the total force needed to penetrate to a depth of h_e is

$$P = \frac{M}{\pi^{1/2}} h_e A^{1/2} \tag{1.16}$$

In the anisotropic case, the following relationship is true:

$$h_e = \frac{\pi}{2} (a_1 a_2)^{1/2} \cot \alpha \tag{1.17}$$

Therefore the following relationship holds true:

$$A^{1/2} = (\pi a_1 a_2)^{1/2} = \frac{2 h_e}{\sqrt{\pi} \cot \alpha} \tag{1.18}$$

The total force needed to penetrate the halfspace to a depth of h_e becomes

$$P = \frac{2}{\pi} M \tan \alpha h_e^2 \tag{1.19}$$

Again, there is a quadratic relationship between the reaction force and the indentation depth. M is the indentation modulus. It is defined as:

$$M = \frac{4\pi}{\int_0^{2\pi} (a_{3i} B_{ij}^{-1}(\gamma) a_{3j}/((a_1/a_2)\cos^2\gamma + (a_1/a_2)\sin^2\gamma)^{1/2})d\gamma} \tag{1.20}$$

where a_{3i} is the indentation vector containing the direction cosines with the normal to the surface. B_{ij} is a Barnett-Lothe tensor defined by

$$\boldsymbol{B(t)} = \frac{1}{2\pi}\int_0^{2\pi}((\boldsymbol{mn})_{ik}(\boldsymbol{nn})_{kl}^{-1}(\boldsymbol{nm})_{lj} - (\boldsymbol{mm})_{ij})d\phi \tag{1.21}$$

according to Swadener and Pharr [SP01]. The vectors $\boldsymbol{m},\boldsymbol{n}$ and $\boldsymbol{t}$ form a right-hand orthogonal coordinate system. While $\boldsymbol{m}$ and $\boldsymbol{n}$ need to be unit vectors, this is not necessary for $\boldsymbol{t}$ according to Franzoso et al. [FZ09]. The second order tensors $(\boldsymbol{ab})_{ij}$ are defined as

$$(\boldsymbol{ab})_{jk} = \boldsymbol{a}_i \mathbb{S}_{ijkl} \boldsymbol{b}_l$$

where $\mathbb{S}_{ijkl}$ are the components of the stiffness tensor $\mathbb{S}$. Instead of using equation (1.6) to extract the isotropic elastic modulus, in the anisotropic case the indentation modulus E_{ind} is extracted using equation (1.7). Depending on the material symmetry there will be different indentation moduli for each direction. For anisotropic materials, there is an infinite number of moduli. In the case of transverse isotropy, the maximum of the modulus distribution will be in axial direction. In the isotropic transverse plane, the indentation modulus will be constant.

1.4 Nanoindentation in bone

Bone is a natural composite of living cells surrounded by non-living extra cellular matrix (ECM) with a hierarchical structure. It is designed to provide mechanical support, protect vital organs, store bone marrow and metabolize calcium. It features at least 6 levels of organisation making up the global mechanical response of the skeleton [Zys09]. The different levels are:

- Mineralized collagen fibrils (MCF)
- Lamellae
- Bone Structural Unit (BSU)
- Cortical shell and trabeculae
- Trabecular bone
- Organ

The characteristic length scale of the different levels varies widely from about 200nm for the MCF to multiple cm for the whole organ. While biomechanical testing of bone has been performed on the macroscale for more than a century, there are still many challenges due to spatial, inter-subject and age variation of mechanical properties. Micromechanical analysis of bone as a hierarchical composite is a new and rapidly developing field in biomechanics. Very little is known about the exact mechanisms dominating the micro-scale mechanical behaviour of bone at the moment. Fig. 1.6 shows the structure of compact bone as described by Kristic [Kri91].
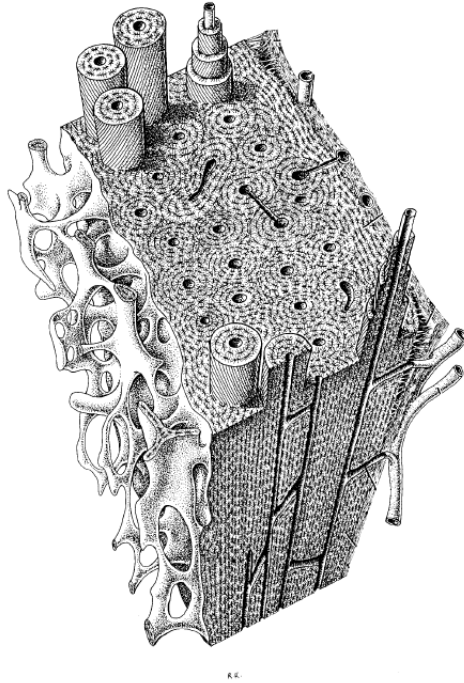
Figure 1.6: Structure of trabecular and compact bone, from Kristic [Kri91]

Nanoindentation in bone aims at characterizing the mechanical properties on the lamellar or BSU level. The characteristic length scale of this structure is about 2-7μm on the lamellar and 60μm on the BSU level. It is therefore an excellent choice in order to determine local distributions of micromechanical properties. The instrumentation needs to be extremely precise in order to yield reasonable results due to the extremely small forces and displacements involved.

The method originates in the hardness testing of materials which was developed in the 19th century. On the macroscopic and microscopic level, indenters were pressed into the specimens and the force was measured. The contact area was then estimated by optical measurement of the remaining plastic imprint after unloading. The main disadvantages of this method are that the indentation depth could not be measured and that the residual imprint might be considerably smaller than the contact area during indentation due to elastic recovery of the material.

Now, with the development of depth-sensing nanoindentation, this experimental technique has become more and more important in determining the mechanical properties of bone tissue on the lamellar and BSU level [ZEGEH$^+$99]. Measuring the indentation depth at a high accuracy gives the possibility to approximate the actual contact area at a given depth with the help of the indenter shape function. This method is potentially much more precise than the optical measurement of the imprint. A calibration of the system determining the shape function and system compliance is done by indenting fused silica specimens. A resolution of 1nm in depth measurement and 0.01mN in force measurement are realistic at this point. The work done by of Sneddon [Sne48], Oliver and Pharr [OP92] and Swadener and Pharr [SP01] allows us now not only to determine the hardness but also to extract elastic properties of the tissue on the lamellar and BSU level depending on the indentation depth [HGZG05].

Recent studies seem to indicate that the assumption of a purely elastic-plastic deformation of the

14

bone tissue under the indenter is erroneous. The high stress concentration leads to the formation of micro-cracks. This can be described with the help of damage mechanics. The assumptions of an unloading phase with intact elasticity and the insensitivity of the extracted modulus to the indentation depth seem not to hold true for the testing of bone tissue. Due to the complex mechanical problem arising in the context of nanoindentation featuring both nonlinear material behaviour and geometric nonlinearities in a combination with contact mechanics, many recent studies rely on numerical simulations and discretization of the mechanical problem instead of using analytical solutions for a simplified system (see Zhang et al. [ZNO08] and [ZMKO10], Mullins et al. [MBM09], Chen et al. [COZC07]). Attempts have been made to explain the shape of the indentation experiments by using constitutive models accounting for elasto-plasticity and damage accumulation. Thorough studies in this field have been done by Zhang et al. [ZMKO10] using the finite element method in order to show the influence of damaged bone on the shape of the indentation curve. However, the material definition was isotropic in the case of Zhang et al.

1.5 Aims of this study

The main aim of this study is to determine the influence of the material constitutive behaviour in the tested specimen on the accuracy of the experimental results. A finite element model of a conical and a Berkovich indentation will be developed and validated. Different material models will be defined and subsequently indented by a rigid indenter. The elastic properties will be extracted from the indentation curves, thus enabling us to quantify the systematic error made when using the methods of Oliver and Pharr [OP92] for isotropic or Swadener and Pharr [SP01] for anisotropic materials. The Finite Element (FE) method especially allows us to quantify the measurement error made due to the assumption of an unloading phase with intact elasticity and the independence of the measured modulus from indentation depth. Also, the influence of the accumulation of microdamage will be assessed by using an elasto-plastic material model with damage. As this material model is not included in the Abaqus library, a user subroutine UMAT defining the constitutive mechanical behaviour will be implemented in Fortran. Potentially, the error made might be rather large, as the theory used to extract the elastic constants does not account for damage accumulation in the vicinity of the indenter tip and assumes an elasto-plastic material with intact unloading elasticity. Time and rate dependent effects such as viscosity will be neglected in the course of this study.

Chapter 2

Model

The finite element (FE) simulations were performed using the commercial FE solver Abaqus/Standard. The preprocessing was done in Abaqus/CAE, the postprocessing in Abaqus Viewer. Two finite element models were developed. The first model features a conical indenter, the second one a Berkovich indenter.

2.1 Geometry

2.1.1 Conical indenter

The conical indenter was modeled as an analytical rigid body of revolution. The semivertical angle was chosen to be 70,3°. The conical indenter with this particular semivertical angle was found to have the same projected area as a Berkovich indenter, which makes this a good model of an actual indentation experiment. The tip of the cone was rounded with a radius of 100nm. This coincides with a realistic tip geometry of common indenters. The elastic halfspace was modeled by a sufficiently large hexahedron with the dimensions $2r_s \times 2r_s \times h_s$. As stated by Poon [PRR08b], the stiffness of the mechanical response of the system is a function of the size of the modeled region. To be more precise, the following conditions have to be fulfilled in order to get a converged mechanical system response:

$$r_s \geq h_s \tag{2.1}$$

and

$$h_s/h_{max} \geq 100 \tag{2.2}$$

In this case, h_{max} is the maximum indentation depth. Only one quarter of the bone region of interest was modeled and symmetry boundary conditions were applied in x and y direction in order to save computation time. Following the suggestions of Poon [PRR08b], a cube with a side length of 100μm was used to simulate the elastic halfspace.

2.1.2 Berkovich indenter

The Berkovich Indenter was modeled as a discrete rigid body in Abaqus CAE. The finite tip radius was set to 100nm, which coincides with usual tip geometries. As stated in the last section, the stiffness of the mechanical response of the halfspace is a function of the size of the modeled region. A hexahedron with the dimensions $200\mu m \times 100\mu m \times 100\mu m$ was modeled. The model fulfills

the convergence criteria formulated by Poon [PRR08b]. Only one half of the halfspace had to be modeled due to material and geometric symmetries.

2.2 Mesh

2.2.1 Conical indenter

Linear hexahedral elements with reduced integration and enhanced hourglass control (C3D8R) were used to mesh the halfspace. This choice of elements was made following the suggestions in the Abaqus manual for simulations involving contact and large deformations. The reduced integration makes the problem computationally less expensive as well. In order to allow nonlinear analysis of large deformations, NLGEOM was activated. The full Newton algorithm was used to solve the nonlinear equation system. In order to avoid numerical problems due to element distortion, arbitrary Lagrangian Eulerian (ALE) remeshing was activated. In this technique, the displacement is mapped in the Lagrangian, the eulerian and the ALE domain. The displacement increments take place in the Lagrangian configuration. In order to avoid excessive mesh distortion, the nodes are allowed to move with respect to the material during mesh sweeps. An advection step is then performed in the eulerian domain to map the solution from the old to the new mesh. This technique is computationally more expensive than a purely Lagrangian problem. However, the mesh sweeps can be performed automatically and at high frequencies, which keeps the number of equilibrium iterations low and the accuracy of the solution at a high level. Enhanced hourglass control is required by the ALE algorithm. Therefore it was used in this model. The undeformed mesh of the whole model may be seen in Fig. 2.1.
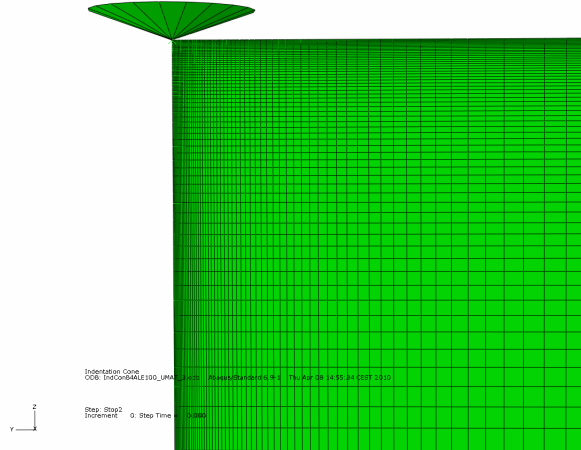
Figure 2.1: Side view of the undeformed mesh of the whole FE model

The model contains 216000 elements. The modeled region is very big compared to the region of interest in order to fulfill the convergence criteria by Poon. Also, the gradients of the field variables are comparatively large near the tip and very small at some distance to the indentation. Therefore the edges of the cube were seeded with a clear bias towards the site of the indentation. This allowed to have a fine mesh with a characteristic element length of about 150nm near the indenter tip while maintaining a relatively small number of elements.
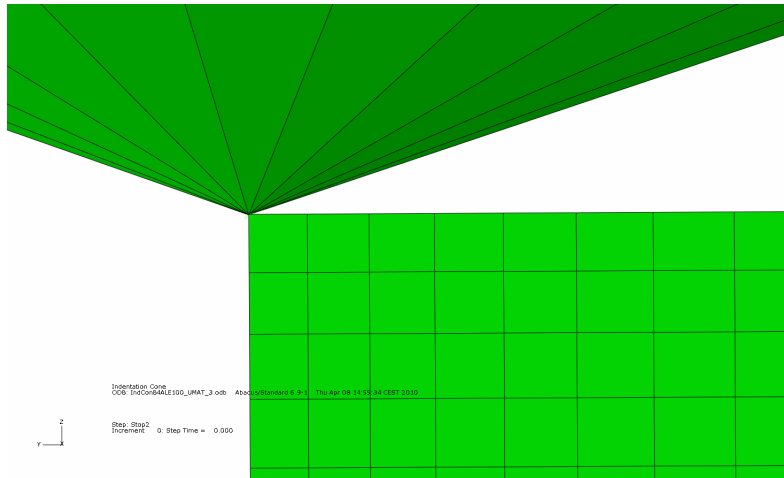
Figure 2.2: Side view of the undeformed mesh at the region of interest near the conical tip

As can be seen in Fig. 2.2, even though the mesh is relatively fine near the tip, it is too coarse to show the exact deformation at the rounded tip. However, the influence of the finite tip radius diminishes with increasing indentation depth. Therefore the chosen level of discretization seemed to be a good compromise between exactness of the solution and computational cost.

2.2.2 Berkovich indenter

Linear hexahedral elements with full integration (C3D8) were used to mesh the halfspace. This choice of elements was made, as hourglassing problems were encountered when using reduced integration elements as suggested in the Abaqus manual for simulations involving contact and large deformations. Fully integrated elements are more sensible to element distortion and have a higher computational cost than reduced integrated elements which were used for the conical indenter. In order to allow nonlinear analysis of large deformations, NLGEOM was activated. The full Newton method was used to solve the nonlinear equation system. In order to avoid numerical problems due to element distortion, arbitrary Lagrangian eulerian (ALE) remeshing was activated. The Berkovich indenter was modeled as a discrete rigid body and its surface meshed with rigid tri-node shell elements. The undeformed mesh of the whole model may be seen in Fig. 2.3.
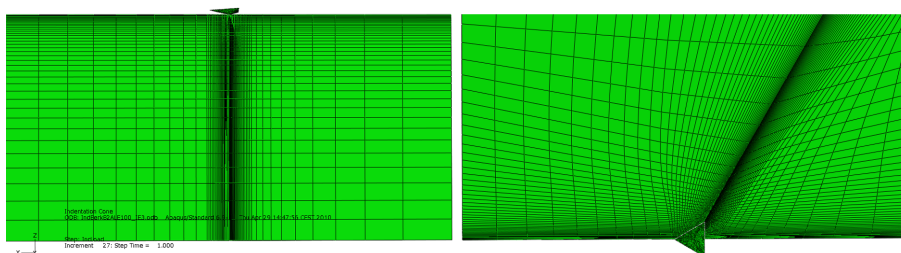
Figure 2.3: Side and top view of the undeformed mesh of the whole FE model

The model contains 147000 deformable elements. The model was partitioned at an angle of 60˚at the indentation site in order to align the element edges with the projection of the edge of the Berkovich tip. The modeled region is big compared to the region of interest in order to fulfill the

18

convergence criteria by Poon. Also, the gradients of the field variables are comparatively large near the tip and very small at some distance to the indentation. Therefore the edges of the cube were seeded with a strong bias towards the site of the indentation. This allowed for a fine mesh with a characteristic element length of about 100nm near the indenter tip while maintaining a relatively small number of elements.
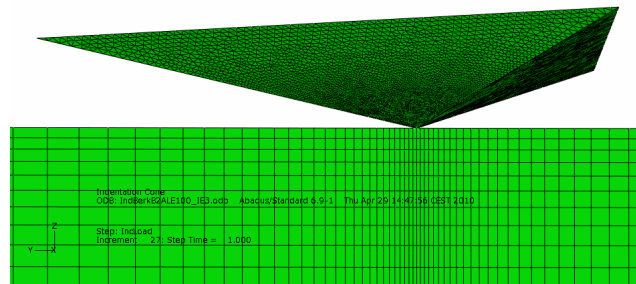
Figure 2.4: Side view of the undeformed mesh at the region of interest near the Berkovich tip

As can be seen in Fig. 2.4, even though the mesh is relatively fine near the tip, it is too coarse to show the exact deformation at the rounded tip. However, the influence of the finite tip radius diminishes with increasing indentation depth. Therefore the chosen level of discretization seemed to be again a good compromise between exactness of the solution and computational cost.

2.3 Boundary conditions

2.3.1 Conical indenter

Only one quarter of the tested specimen is discretized. Symmetry boundary conditions in x-direction constrain the body in the y-z-plane. Furthermore, in y-direction there are symmetry boundary conditions constraining the in the x-z plane. This makes sure that the specimen deforms naturally, even though the body was cut to a quarter of its original size to reduce the computational cost of the numerical model. The specimen is further constrained on the bottom of the specimen in axial direction, in which the specimen is tested. The conical indenter is modeled as an analytical rigid body and has a reference point defined at its tip. The degrees of freedom (DOFs) 1, 2 and 4 to 6 are locked for the indenter tip. Contact is defined between the conical tip and the surface of the tested bone specimen. The rigid tip acts as master surface, the bone surface as slave. In direction normal to the surfaces, hard contact is defined. There is no friction in tangential direction. The DOF 3 of the conical tip is used to perform the indentation experiment. The numerical experiments are run in displacement control.

2.3.2   Berkovich indenter

Only one half of the tested specimen is modeled. Symmetry boundary conditions in x-direction constrain the body in the y-z-plane. The nodes at the middle of the modeled halfspace are locked in y-direction in order to constrain rigid body motion in this direction. This makes sure that the specimen deforms naturally, even though the body was cut in half in order to reduce the computational cost of the numerical model. The specimen is further constrained on the bottom of the specimen in axial direction, in which the specimen is tested. The Berkovich indenter is modeled as a discrete rigid body and has a reference point defined at its tip. The DOFs 1, 2, 4, 5 and 6 are locked for the indenter tip. Contact is defined between the Berkovich tip and the surface of the tested bone specimen. The rigid tip acts as the master surface, the bone surface as the slave. In direction normal to the surfaces, hard contact is defined. There is no friction in tangential direction. The DOF 3 of the Berkovich tip is used to perform the indentation experiment. The numerical experiments are run in displacement control.

2.4   Materials

2.4.1   Isotropic linear elasticity

The most simple material model used in this study is isotropic linear elasticity. This type of elasticity shows a linear relationship between stress and strain and leaves no residual strains after a loading cycle. Isotropy means that the material behaviour is independent of the loading direction. The elasticity tensor can therefore be represented by a sphere. Fig. 2.4.1 shows the stress-strain relationship of a linear elastic material.
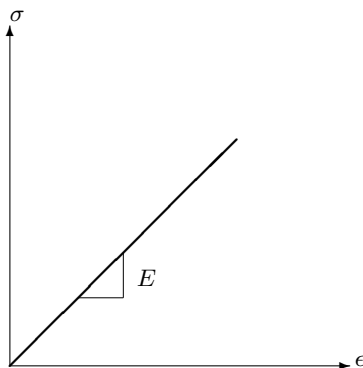
Figure 2.5: Stress vs. strain for linear elasticity

Three different linear elastic materials were defined for this study. Material ILE A represents an isotropic approximation of linear elasticity of bone. The material ILE B has a very low Poisson ratio, ILE C is almost incompressible. Table 2.4.1 shows the parameters of the different materials and the corresponding indentation moduli.

Material	E	ν	E_{ind}
ILE A	20	0.30	21.98
ILE B	20	0.01	20.00
ILE C	20	0.49	26.32

Table 2.1: Elastic material constants and indentation modulus $[GPa]$

2.4.2 Transversely isotropic linear elasticity

Due to its inherent structure, bone shows an anisotropic mechanical behaviour. Anisotropy in this case is the dependency of the mechanical response of the material on the loading direction. A linear elastic transversely isotropic material was defined for this study. Transverse isotropy is a special type of anisotropy. In this case, there is a plane normal to the axial direction in which the material behaviour is isotropic. It is called the transverse plane. However, the elastic constants in axial direction are different than the in-plane properties. Instead of a sphere, the elastic tensor has the form of an ellipsoid. The fabric model by Zysset and Curnier [ZC95] was used to model the transverse isotropic behaviour. Table 2.4.2 shows the parameters used for the fabric model in order to model bone tissue.

E_O	ν_O	G_O	ρ	k	m_1	m_2	m_3	l
12.95	0.3	4.982	1.0	1.0	0.879	0.879	1.243	1.0

Table 2.2: Fabric elasticity parameters for transverse isotropy of bone tissue

The fabric model connects fabric tensors describing microstructures to the fourth-order elasticity tensor. The following relationships hold true for the fabric model:

$$E_{ii} = E_0 \cdot \rho^k \cdot m_i^{2l} \tag{2.3}$$

$$\nu_{ij} = \nu_0 \cdot \rho^k \cdot \frac{m_i^l}{m_j^l} \tag{2.4}$$

$$G_{ij} = G_0 \cdot \rho^k \cdot m_i^l m_j^l \tag{2.5}$$

where m_i are the eigenvalues of the fabric tensor. For more information see Zysset and Curnier [ZC95]. These relationships were used to compute the engineering constants defining the transverse isotropy for this material model of bone. Table 2.4.2 shows the material constants used in the simulation.

E_{11}	E_{22}	E_{33}	ν_{12}	ν_{13}	ν_{23}	G_{12}	G_{13}	G_{23}
10.0	10.0	20.0	0.3	0.212	0.212	3.846	5.439	5.439

Table 2.3: Engineering constants for transverse isotropy of bone tissue

A three-dimensional representation of the elasticity tensor, in this case the distribution of Young's modulus as a function of direction, built with these parameters can be seen in Fig. 2.6.
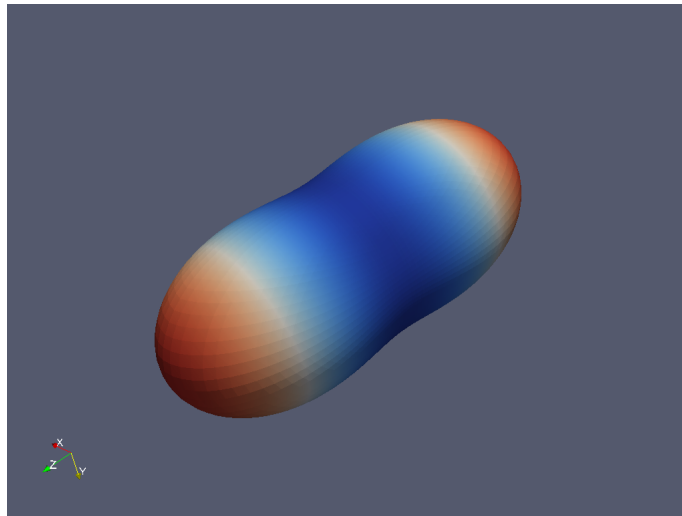
Figure 2.6: 3D representation of the Young's modulus distribution for transverse isotropy of bone

The indentation modulus was computed using the method of Swadener and Pharr [SP01] in axial and transverse direction. It is $18.48 GPa$ in axial direction and $11.99 GPa$ in transverse direction.

2.4.3   Isotropic elasto-plasticity

An isotropic elastic ideal plastic material (IEP) model was implemented using the Mises yield surface. In ideal plasticity, there is no hardening of the material after the yield point is reached. Plastic deformation leads to residual strains after a loading cycle. A scheme of the stress-strain behaviour of ideal elasto-plasticity is shown in Fig. 2.4.3.
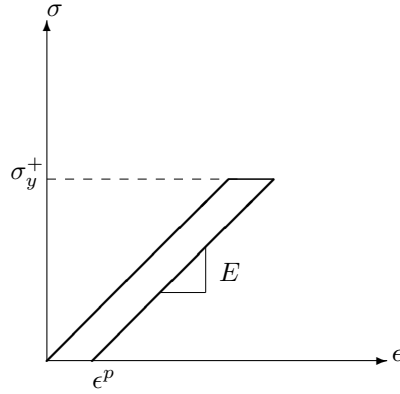
Figure 2.7: Stress vs. strain for ideal elasto-plasticity

A Mises yield surface was chosen. The yield strength in tension σ_y^+ and compression σ_y^- were assumed to be identical in this case. Two different materials were defined. Material IEP A will be used to compare the results to a study by Poon [PRR08b], IEP B is a isotropic elasto-plastic approximation of the mechanical properties of bone. The material constants used for the two materials are shown in Table 2.4.3.

Material	E	ν	σ_y
IEP A	50	0.3	1.0
IEP B	20	0.3	0.175

Table 2.4: Elastic material constants

Both the elastic properties and the post-yield behaviour are isotropic for these two material models. The elastic tensor can be represented by a sphere.

2.4.4 Anisotropic elasto-plasticity

An anisotropic elasto-plastic material (AEP) featuring transversely isotropic ideal Hill plasticity was implemented using the fabric model of Zysset and Curnier [ZC95]. The Hill yield criterion is a simple extension of the isotropic Mises criterion [Hil98]. The Hill criterion models the anisotropic yield behaviour on the basis of a reference yield stress σ_0 with the help of yield stress ratios R_{ij}. Hill's yield function can be expressed in terms of cartesian stress components as

$$f(\sigma) = \sqrt{F(\sigma_{22} - \sigma_{33})^2 + G(\sigma_{33} - \sigma_{11})^2 + H(\sigma_{11} - \sigma_{22})^2 + 2L\sigma_{23}^2 + 2M\sigma_{31}^2 + 2N\sigma_{12}^2} \qquad (2.6)$$

F, G, H, L, M and N are material constants based on the anisotropic material behaviour. They are defined with the help of the yield stress ratios R_{ij}.

$$F = \frac{1}{2}(\frac{1}{R_{22}^2} + \frac{1}{R_{33}^2} - \frac{1}{R_{11}^2})$$
$$G = \frac{1}{2}(\frac{1}{R_{33}^2} + \frac{1}{R_{11}^2} - \frac{1}{R_{22}^2})$$
$$H = \frac{1}{2}(\frac{1}{R_{11}^2} + \frac{1}{R_{22}^2} - \frac{1}{R_{33}^2})$$
$$L = \frac{3}{2R_{23}^2} \qquad M = \frac{3}{2R_{13}^2} \qquad N = \frac{3}{2R_{12}^2} \tag{2.7}$$

The yield stress ratios R_{ij} are defined as

$$R_{ij} = \begin{cases} \frac{\sigma_{ij}}{\sigma_0} = \rho^k m_i^{2l} & \text{if } i = j, \\ \frac{\tau_{ij}}{\tau_0} = \rho^k m_i^l m_j^l & \text{if } i \neq j. \end{cases}$$

Table 2.4.4 shows the elastic constants of the fabric elasticity model defining the transverse isotropic elasticity used in this study in order to approximate the mechanical behaviour of compact bone.

E_O	ν_O	G_O	ρ	k	m_1	m_2	m_3	l
12.2	0.366	4.465	1.0	1.0	0.956	0.956	1.088	1.0

Table 2.5: Fabric elasticity parameters modeling bone

Table 2.4.4 shows the engineering constants derived from the fabric model.

E_{11}	E_{22}	E_{33}	ν_{12}	ν_{13}	ν_{23}	G_{12}	G_{13}	G_{23}
11.15	11.15	14.44	0.366	0.313	0.313	4.081	4.644	4.644

Table 2.6: Engineering constants for transversely isotropic elastic model of compact bone

Fig. 2.8 shows the graphic representation of the elasticity tensor, in this case the distribution of Young's modulus as a function of direction, of the material AEP in 3D.
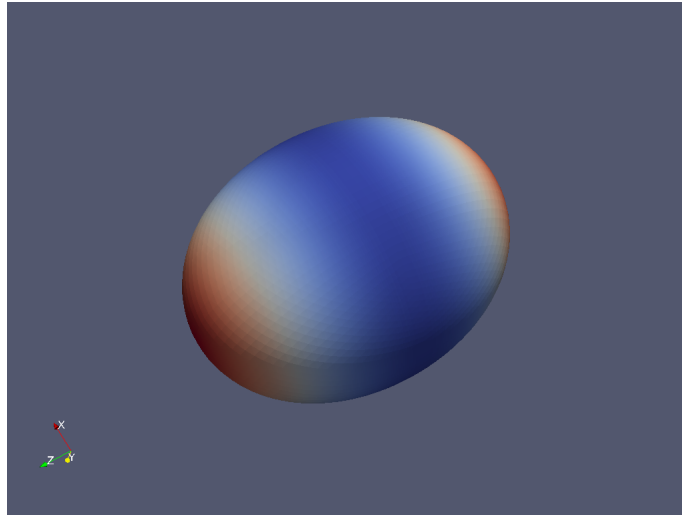
Figure 2.8: 3D Young's modulus distribution for anisotropic elasto-plastic bone model

The user defined reference yield stress was chosen to be $\sigma_0 = 0.138$ GPa. The reference yield shear stress is defined as

$$\tau_0 = \frac{\sigma_0}{\sqrt{3}} \tag{2.8}$$

for Hill plasticity in the Abaqus user's manual. Table 2.4.4 shows the yield stress ratios used to implement the Hill plasticity model for bone in ABAQUS/Standard.

R_{11}	R_{22}	R_{33}	R_{12}	R_{13}	R_{23}
0.914	0.914	1.184	0.914	1.040	1.040

Table 2.7: Yield stress ratios for ideal Hill plasticity model of compact bone

Fig. 2.9 shows a cut through the yield surface in the S_{11} - S_{22} plane.
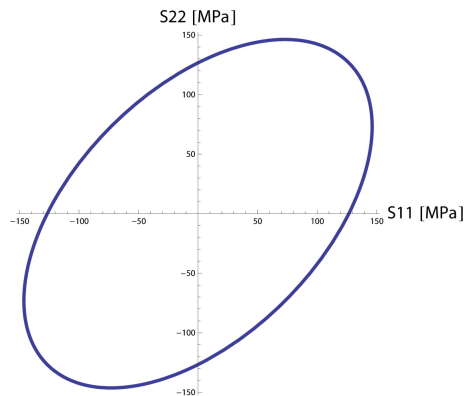
Figure 2.9: Yield surface in the S_{11} - S_{22} plane for Hill plasticity

25

Fig. 2.10 illustrates a cut through the yield surface in the S_{11}-S_{33} plane in the case of an axial symmetric stress state.
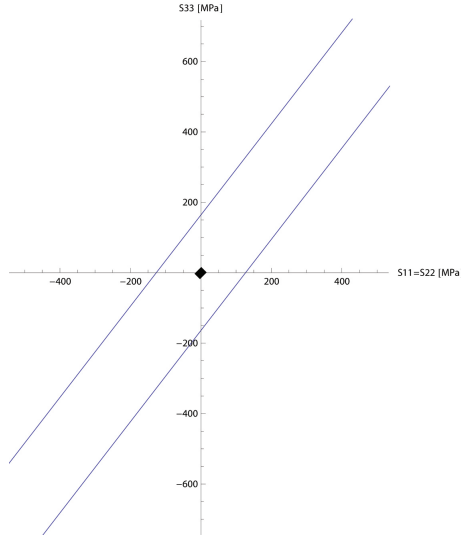
Figure 2.10: Yield surface in the S_{11}-S_{33} plane in the case of an axial symmetric stress state for Hill plasticity

2.4.5 Anisotropic elasto-plasticity and damage

A material AEPD featuring orthotropic elasto-plasticity with isotropic linear hardening and damage was implemented as well. Damage and plastic deformation are simultaneously accumulated when the yield criterion is fulfilled in this model. It is assumed that the damage constitutes itself in microcracks in the material. It decreases the effective stiffness of the specimen. Fig. 2.4.5 shows the scheme of a typical stress-strain relationship for elasto-plasticity and damage.
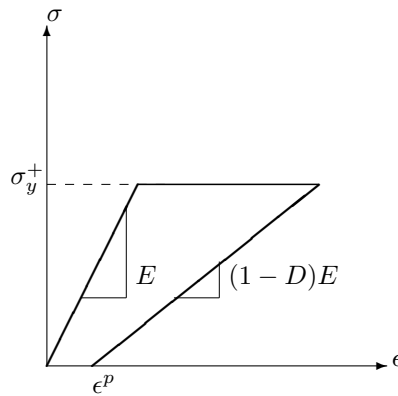
Figure 2.11: Stress vs. strain for ideal elasto-plasticity and damage

For the orthotropic elasticity model of compact bone, the parameters measured by Ashman et al. [ACBR84] were used. They can be seen in Table 2.4.5.

E_{11}	E_{22}	E_{33}	G_{12}	G_{13}	G_{23}	ν_{12}	ν_{13}	ν_{23}	ν_{21}	ν_{31}	ν_{32}
12.0	13.4	20.0	4.53	5.61	6.23	0.376	0.222	0.235	0.422	0.371	0.350

Table 2.8: Engineering constants by Ashman et al. for orthotropic elasticity

Model

The constitutive relationship used was developed by Zysset [Zys94]. It is not included in the Abaqus material library. Therefore a user subroutine defining the mechanical behaviour of the material (UMAT) was implemented in Fortran. It was assumed that compact bone does not yield under a simultaneous homogeneous deformation in all three main material directions. Therefore the symmetric orthotropic stiffness matrix used for this model is decomposed into two parts:

$$\mathbb{S} = \bar{\mathbb{S}} + \mathbb{S}'$$

It consists of a constant part that represents a special eigentensorial state and a damageable part. In order to find the constant part of the decomposition of the stiffness matrix, an eigensystem analysis needs to be performed. The stiffness matrix is of rank 6, which means that is has six eigenvalues $\lambda_{\mathbb{S},i}$ and six corresponding eigenvectors e_{λ_i}. The constant part of the decomposition representing a special eigentensorial state is constructed by multiplying the biggest eigenvalue with the dyadic product of the corresponding eigenvector with itself.

$$\bar{\mathbb{S}} = \lambda_{\mathbb{S},max}(e_{\lambda_{\mathbb{S},max}} \otimes e_{\lambda_{\mathbb{S},max}})$$

The damageable part of the stiffness matrix is the difference of the total stiffness matrix and the constant part of the decomposition.

$$\mathbb{S}' = \mathbb{S} - \bar{\mathbb{S}}$$

The compliance tensor $\mathbb{E}$ is also decomposed into a constant part $\bar{\mathbb{E}}$ and a damageable part $\mathbb{E}'$. An eigensystem analysis of the compliance tensor is done and the constant part of the decomposition is computed by multiplying its smallest eigenvalue with the dyadic product of the corresponding eigenvector with itself.

$$\bar{\mathbb{E}} = \lambda_{\mathbb{E},min}(e_{\lambda_{\mathbb{E},min}} \otimes e_{\lambda_{\mathbb{E},min}})$$

The damageable part of the compliance matrix is the difference of the total compliance matrix and the constant part of the decomposition.

$$\mathbb{E}' = \mathbb{E} - \bar{\mathbb{E}}$$

It should be noted that the eigentensors of the stiffness matrix and the compliance matrix are equivalent. The eigenvalues of the stiffness matrix are the inverse of the eigenvalues of the compliance matrix. For more information on the structure of the stiffness and compliance matrices see Appendix B. The total stress is also decomposed into two parts: The first part results from the the constant part of the decomposition of the stiffness matrix $\bar{\mathbb{S}}$. The second part results from the damaged stiffness matrix $\mathbb{S}'$. It will be called "deviatoric" from now on for the sake of brevity.

$$\boldsymbol{S} = \bar{\boldsymbol{S}} + \boldsymbol{S}' = \bar{\mathbb{S}}(\boldsymbol{E} - \boldsymbol{E}^P) + f(\alpha)\mathbb{S}'(\boldsymbol{E} - \boldsymbol{E}^P)$$

In general, the material stress of the model and its conjugate variable are given by the expressions:

$$\boldsymbol{S} = \bar{\mathbb{S}}(\boldsymbol{E} - \boldsymbol{E}^P) + f(\alpha)\mathbb{S}'(\boldsymbol{E} - \boldsymbol{E}^P)$$

$$S^{\alpha} = -\frac{1}{2} f'(\alpha)(\boldsymbol{E} - \boldsymbol{E}^P) : \mathbb{S}'(\boldsymbol{E} - \boldsymbol{E}^P)$$

The damage variable α is a measure of the cumulated plastic strain with respect to the damageable part of the decomposition of the stiffness tensor:

$$\alpha(t) = \int_0^t \sqrt{\dot{\boldsymbol{E}}^p \mathbb{S}' \dot{\boldsymbol{E}}^p} d\tau$$

Three-dimensional algorithm

The following pages will show the implemented three-dimensional algorithm. A purely elastic trial stress is calculated using the initial state plastic strain and damage:

$$\boldsymbol{S}_T = \bar{\mathbb{S}}(\boldsymbol{E} - \boldsymbol{E}_0^P) + f(\alpha_0)\mathbb{S}'(\boldsymbol{E} - \boldsymbol{E}_0^P)$$

$$S_T^{\alpha} = -\frac{1}{2} f'(\alpha_0)(\boldsymbol{E} - \boldsymbol{E}_0^P) : \mathbb{S}'(\boldsymbol{E} - \boldsymbol{E}_0^P)$$

with the "deviatoric" trial stress $\boldsymbol{S}_T'$

$$\boldsymbol{S}_T' = f(\alpha_0)\mathbb{S}'(\boldsymbol{E} - \boldsymbol{E}_0^P)$$

The yield criterion $y(\boldsymbol{S}; \alpha)$ is defined as

$$y(\boldsymbol{S}; \alpha) = \sqrt{\boldsymbol{S} : \mathbb{E}' \boldsymbol{S}} - g(\alpha)$$

The damage function $f(\alpha)$ is

$$f(\alpha) = e^{-\frac{\alpha}{\alpha_f}}$$

The cumulated damage is defined as

$$D = 1 - f(\alpha)$$

In the undamaged state, D is equal to 0, in the case of complete failure D equals 1. The hardening function $g(\alpha)$ is

$$g(\alpha) = y_{\sigma}$$

for ideal plasticity (Material AEPDI) and

$$g(\alpha) = g_{max}(1 - e^{-\frac{\alpha}{\alpha_g}}) + y_{\sigma}$$

in the case of exponential hardening (Material AEPDE). The material parameters α_f, g_{max}, α_g and y_{σ} were identified by Zysset [Zys94]. They are shown in Table 2.4.5.

α_f	g_{max}	α_g	y_{σ}
0.09898	0.01075	0.02625	0.02277

Table 2.9: Material parameters in $\sqrt{GPa}$

If the yield criterion is

$$y(\boldsymbol{S}_T; \alpha_0) \leq 0$$

28

then

$$\{\boldsymbol{E}^P, \alpha\} = \{\boldsymbol{E}_0^P, \alpha_0\}$$
$$\boldsymbol{S} = \boldsymbol{S}_T$$
$$S^\alpha = S_T^\alpha$$

In the rate independent case, the plastic stress is equal to the total stress:

$$\boldsymbol{S} = \boldsymbol{S}^E = \boldsymbol{S}^{E^p}$$

The tangent stiffness operator in the elastic case is:

$$\mathbb{S}^u = \nabla_E \boldsymbol{S}^E = \bar{\mathbb{S}} + f(\alpha_0)\mathbb{S}'$$

If the yield criterion is

$$y(\boldsymbol{S}_T; \alpha_0) > 0$$

then the implicit projection algorithm is performed. It uses the following set of equations:

$$\boldsymbol{S} = \bar{\mathbb{S}}(\boldsymbol{E} - \boldsymbol{E}^P) + f(\alpha)\mathbb{S}'(\boldsymbol{E} - \boldsymbol{E}^P)$$

$$S^\alpha = -\frac{1}{2}f'(\alpha)(\boldsymbol{E} - \boldsymbol{E}^P) : \mathbb{S}'(\boldsymbol{E} - \boldsymbol{E}^P)$$

$$\boldsymbol{E}^p - \boldsymbol{E}_0^p = \lambda_\alpha \boldsymbol{N}$$

$$\alpha - \alpha_0 = \lambda_\alpha$$

$$y(\boldsymbol{S}; \alpha) = 0$$

with

$$\boldsymbol{N} = \frac{\mathbb{E}'\boldsymbol{S}}{\sqrt{\boldsymbol{S} : \mathbb{E}'\boldsymbol{S}}}$$

This system of five equations can be reduced to the following scalar equation using the right substitutions:

$$h^i(\lambda^i) = (\sqrt{\boldsymbol{S}_T' \mathbb{E}' \boldsymbol{S}_T'} - \lambda^i f(\alpha_0))f(\alpha_0 + \lambda^i) - f(\alpha_0)g(\alpha_0 + \lambda^i)$$

The linearization of these formulas has the following form:

$$h^{i+1} = h^i + (\frac{dh}{d\lambda})^i(\lambda^{i+1} - \lambda^i)$$

with

$$\frac{dh}{d\lambda} = (\sqrt{\boldsymbol{S}_T' \mathbb{E}' \boldsymbol{S}_T'} - \lambda^i f(\alpha_0))f'(\alpha_0 + \lambda^i) - f(\alpha_0)f(\alpha_0 + \lambda) - f(\alpha_0)g(\alpha_0 + \lambda^i)$$

The recurrence formula of the Newton scheme becomes:

$$\lambda^{i+1} - \lambda^i = -\frac{h^i}{(\frac{dh}{d\lambda})^i}$$

After convergence of the Newton algorithm, the final updated internal variables are

$$\alpha = \alpha_0 + \lambda$$

$$\boldsymbol{S}' = \boldsymbol{S}_T' \frac{f(\alpha_0 + \lambda)g(\alpha_0 + \lambda)}{f(\alpha_0)(g(\alpha_0 + \lambda) + \lambda f(\alpha_0 + \lambda))}$$

$$\boldsymbol{E}^P = \boldsymbol{E}^P_0 + \frac{\lambda}{g(\alpha_0 + \lambda)} \mathbb{E}' \boldsymbol{S}'$$

The final total updated stress becomes:

$$\boldsymbol{S} = \bar{\mathbb{S}}(\boldsymbol{E} - \boldsymbol{E}^P) + f(\alpha)\mathbb{S}'(\boldsymbol{E} - \boldsymbol{E}^P)$$

According to Zysset [Zys94], the continuum tanget stiffness operator is provided by the consistency condition

$$\dot{y}(\boldsymbol{S}; \alpha) = 0$$

It is defined as

$$\mathbb{S}^u = \nabla_E \boldsymbol{S}$$

The continuum tangent stiffness operator takes the form of:

$$\mathbb{S}^u = \mathbb{S} - \frac{\mathbb{S}(\mathbb{E}'\boldsymbol{S} \otimes \mathbb{E}'\boldsymbol{S})\mathbb{S}}{\mathbb{E}'\boldsymbol{S} : \mathbb{S}\mathbb{E}'\boldsymbol{S} + c(\alpha)g'(\alpha)\sqrt{\boldsymbol{S} : \mathbb{E}'\boldsymbol{S}}}$$

where

$$c(\alpha) = \frac{f^2(\alpha)}{f^2(\alpha) - f'(\alpha)}$$

The consistent tangent stiffness operator represents the linearization of the incremental backprojection algorithm instead of the continuum rate law. It is defined as

$$\mathbb{S}^u_a = \nabla_{E^{i+1}} \boldsymbol{S}^{i+1}$$

It takes the form of:

$$\mathbb{S}^u_a = \mathbb{S}^i_a - \frac{\mathbb{S}^i_a(\mathbb{E}'\boldsymbol{S}^i \otimes \mathbb{E}'\boldsymbol{S}^i)\mathbb{S}^i_a}{\mathbb{E}'\boldsymbol{S}^i : \mathbb{S}^i_a\mathbb{E}'\boldsymbol{S}^i + c^i g'(\alpha_0 + \lambda^i_\alpha)\sqrt{\boldsymbol{S}^i : \mathbb{E}'\boldsymbol{S}^i}}$$

where

$$\mathbb{S}^i_a = \bar{\mathbb{E}} + \frac{\mathbb{E}'}{f(\alpha_0 + \lambda^i_\alpha)} + \lambda^i_\alpha \frac{\mathbb{E}'(\boldsymbol{S}^i : \mathbb{E}'\boldsymbol{S}^i) - \mathbb{E}'\boldsymbol{S}^i \otimes \mathbb{E}'\boldsymbol{S}^i}{(\boldsymbol{S}^i : \mathbb{E}'\boldsymbol{S}^i)^{\frac{3}{2}}}$$

It should be noted that the tangent operator for this particular material law is symmetric. For more information on the elasto-plastic material law with damage, see the work of Zysset [Zys94]. The Fortran implementation of this algorithm may be seen in Appendix A.

Chapter 3

Verification

3.1 Isotropic linear elasticity

In order to validate the model and verify the results of the simulations, the indentation of a conical indenter into an elastic halfspace was modeled in Abaqus/Standard and the results were compared to the analytical solution by Sneddon. Linear elastic material behaviour with an elastic modulus of 20 GPa was chosen. The simulations were compared to the analytical solution for a range of Poisson ratios from 0.01 to 0.49. The indentation depth of the simulated experiments was 1μm. The numerical results were compared to the analytical solution by Sneddon as well as an empirical formula found by Poon [PRR08a] that takes into account the finite tip radius and stiffening effects due to radial displacements on the contact surface as described by Hay et al. [HBP99].

3.1.1 ILE A

First, a simulation of an indentation of a conical indenter was performed for ILE A, which is an isotropic linear elastic material with an elastic modulus of 20GPa and a Poisson ratio of 0.3. According to the analytical solution for a conical punch into an elastic halfspace, the reaction force on the tip should be proportional to the square of the indentation depth. Poon [PRR08a] found out that the finite radius of the tip changes the mechanical response of the system compared to the solution by Sneddon. Also, he found that there is a stiffening effect with respect to the solution of Sneddon [Sne48] that is a function of the Poisson ratio. This effect was explained by Hay et al [HBP99] with the presence of radial displacements of the surface points inside the contact area in the problem modeled by Sneddon that are not accounted for in the analysis. The size of these radial displacements is dependent on the Poisson ratio and diminishes for incompressible materials. This effect will be addressed further in section 5.1. Fig. 3.1 shows the comparison of the numerical simulation to the analytical solution of Sneddon and the empirical formula by Poon.

Figure 3.1: Force [mN] vs. displacement [μm] for the conical indenter, the analytical solution of Sneddon [Sne48] and the empirical formula by Poon [PRR08b] for $\nu = 0.3$

As can be seen in Fig. 3.1, the mechanical response of the system follows a quadratic relationship between indentation depth and reaction force. This is the expected result and coincides with the form of the analytical solution for this particular problem. The indentation modulus is slightly higher than the one of the analytical solution for the conical punch. Poon found out in a study conducted in 2008 [PRR08a] that there is a considerable stiffening effect due to finite tip radii and radial displacements of the surface points inside the contact area, which are a function of the material's Poisson ratio. He developed an empirical law based on the analytical solution of the Boussinesq problem by Sneddon that has the form of

$$P = (a_1\nu^2 + a_2\nu + a_3)\frac{2E\tan\alpha}{\pi(1-\nu^2)}h(h + c_1\rho^2 + c_2\rho) \tag{3.1}$$

with $a_1 = -0.062$, $a_2 = -0.156$, $a_3 = 1.12$, $c_1 = 1.5 \times 10^{-2}\mu m^{-1}$ and $c_2 = 0.117$. The numerical data of this study correlates very well with the empirical constitutive equation found by Poon. Fig. 3.2 shows the relative error of the reaction force made when comparing the numerical results to the solutions by Sneddon and Poon.

Figure 3.2: Relative error of force response [ ] vs. displacement [μm] with respect to the analytical solution of Sneddon [Sne48] and the empirical formula by Poon [PRR08b] for $\nu = 0.3$

Fig. 3.2 indicates that the error of the numerical solution compared to the analytical solution by Sneddon is small for small deformations and increases to a constant value of about 8% for indentation depths larger than 0.2μm. The relative error with respect to the empirical formula of Poon that corrects the analytical solution for stiffening effects of the finite tip radius and radial displacements which are a function of the Poisson ratio is high in the beginning. The FE analysis and the empirical solution of Poon 2008 [PRR08a] converge with increasing indentation depth.

The indentation modulus was evaluated at every increment in order to verify that the measured modulus is independent of the indentation depth for indentations of isotropic linear elastic materials. Fig. 3.3 shows the elastic moduli measured at different indentation depths.
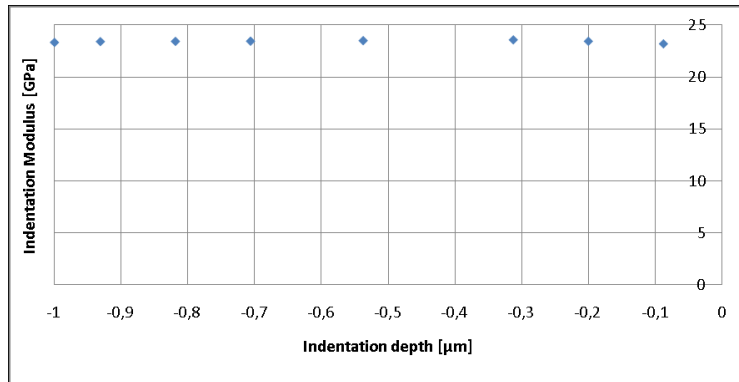
Figure 3.3: Measured indentation modulus [GPa] vs. displacement [μm] for $\nu = 0.3$

Fig. 3.3 clearly indicates that the measured indentation modulus is indeed independent of the indentation depth. This can be seen as the measurements lead approximately to the same modulus for indentation depths larger than 100nm. For very small indentation depths the error is larger, as the mesh is too coarse to properly compute the exact mechanical response. For indentation depths larger than 100nm, the mesh used in these simulations gives us proper results. Fig. 3.4 shows the relative error of the measured indentation moduli as a function of indentation depth.
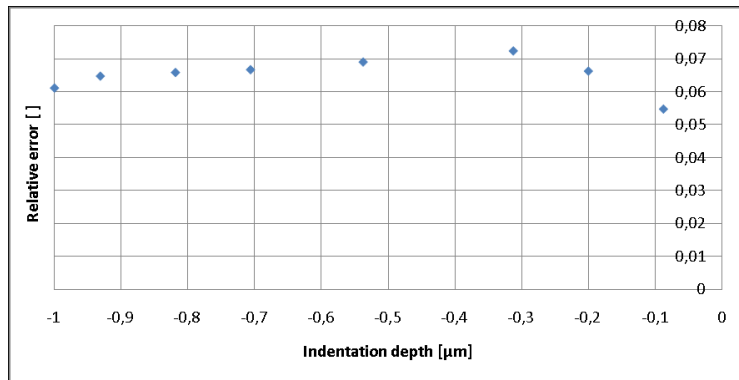
Figure 3.4: Relative measurement error of the indentation modulus [ ] vs. displacement [μm] for $\nu = 0.3$

Another simulation was performed using the Berkovich tip geometry with a finite tip radius of 100nm. The results were compared to the force-displacement data of the conical indenter. Theoretically the curves should be exactly the same, as the projected area of the conical indenter is equal to the one of the Berkovich indenter. The comparison was made in order to verify this assumption. Fig. 3.5 shows the two force-displacement curves.
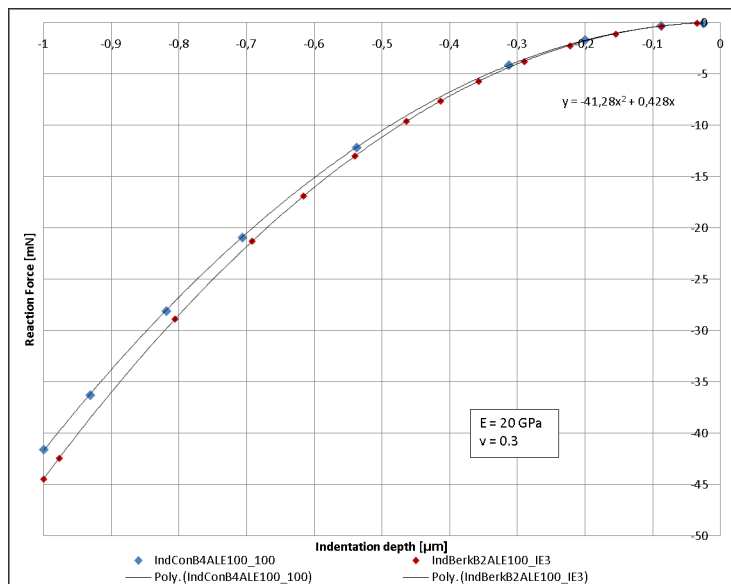
Figure 3.5: Force [mN] vs. displacement [μm] for $\nu = 0.3$ using the Berkovich indenter (red) and the conical indenter (blue)

Fig. 3.6 shows the relative error of the simulation using the conical indenter vs. the Berkovich indenter as a function of indentation depth as well as a comparison to the analytical solution of Sneddon [Sne48] and the empirical solution of Poon [PRR08b].
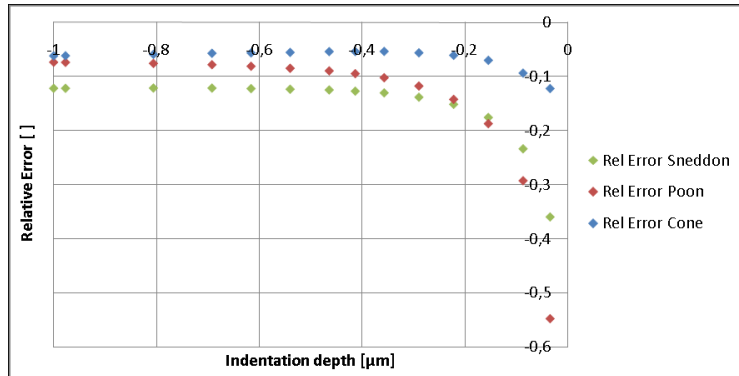
Figure 3.6: Relative error of force response [ ] vs. displacement [μm] for the Berkovich indenter with respect to the conical indenter, the analytical solution of Sneddon [Sne48] and the empirical formula by Poon [PRR08b] for $\nu = 0.3$

As can be seen in Fig. 3.6, there is a constant error with respect to the simulation of the conical indentation of about 6% for indentation depths larger than 200μm. The indentation modulus was evaluated at every increment once more. Fig. 3.7 shows the elastic moduli measured at different indentation depths.
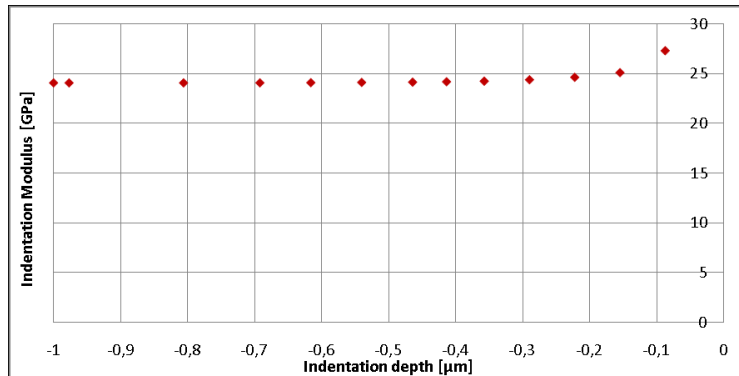
Figure 3.7: Measured indentation modulus [GPa] vs. displacement [μm] for $\nu = 0.3$ using the Berkovich indenter

Fig. 3.7 indicates that the measured elastic modulus is independent of the indentation depth for the Berkovich indenter. This can be seen as the measurements lead to the same moduli for indentation depths larger than 100nm. For very small indentation depths the error is larger, as the mesh is too coarse to properly compute the exact mechanical response. For indentation depths larger than 100nm, the mesh used in these simulations gives us proper results. Fig. 3.8 shows the relative error of the measured elastic moduli as a function of indentation depth.
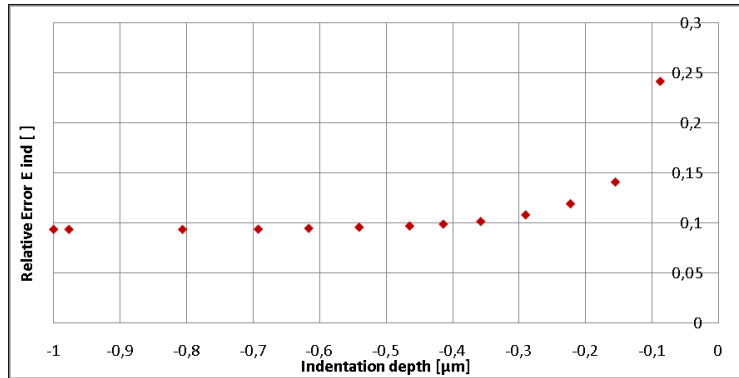
Figure 3.8: Relative error of the measured indentation modulus [ ] vs. displacement [μm] for $\nu = 0.3$ using the Berkovich indenter

The relative error of the measured indentation modulus was high with about 9% compared to the measurements using a conical indenter geometry even though the empirical correction factor of 1.034 [PRR08a] was used in the calculation. Fig. 3.9 shows a contour plot of the von Mises stress distribution around the indentation site for a Berkovich indenter and the material ILE A.
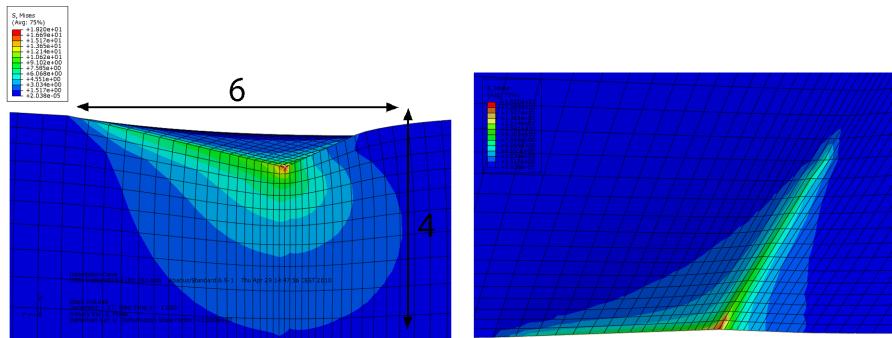
Figure 3.9: Contour plot of von Mises stress [GPa] on the deformed shape at maximum indentation depth (side and top view, Max: 18.2GPa, Min: 1.5GPa)

The maximum von Mises stress under the indenter tip was 18.2GPa. This extraordinarily high value can be explained with the extreme stress concentration under the indenter tip and at the indenter edges in a purely elastic material. The stress at a depth of about 4μm and at a distance of about 3μm to the indentation center was still 1.5GPa. The assumption that the conical indenter is a feasible substitute for the Berkovich geometry in the case of an isotropic linearly elastic material seems to be valid. The relative error of about 6% with respect to the conical indenter is most probably due to the extremely (and theoretically infinitely) high stress concentrations at the indenter tip and edges that are not correctly accounted for by the coarse mesh, which might influence the accuracy of the simulation.

Also, a convergence study was performed with the material ILE A by refining the mesh of the conical indenter by a factor of two. 432000 elements were used instead of 216000. The relative error in the maximum force was 1.02% when compared to the empirical formula of Poon at an indentation depth of 0.6 μm. Therefore there is no significant increase in solution accuracy with decreased element size. The computation time and memory consumption however increased significantly.

Therefore the mesh refinement may be considered reasonable for the given problem.

3.1.2 ILE B

Then, another simulation of an indentation of a conical indenter was performed for ILE B, an isotropic linear elastic material with an elastic modulus of 20GPa and a very low Poisson ratio of 0.01.
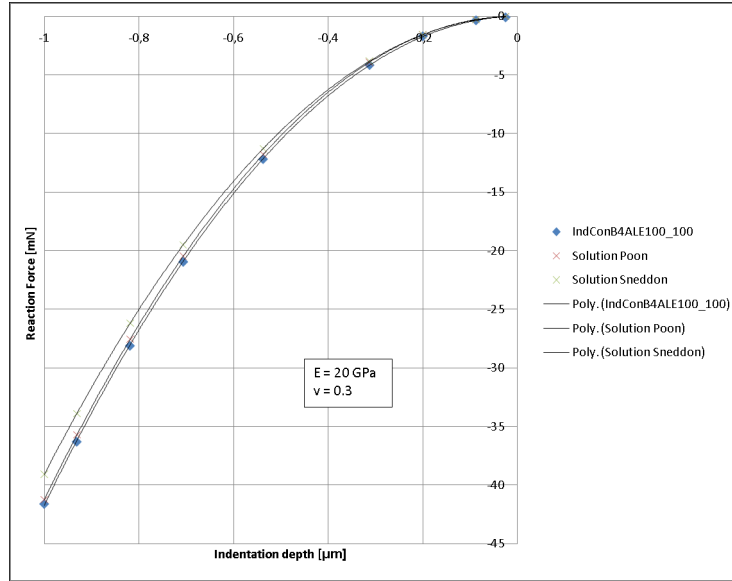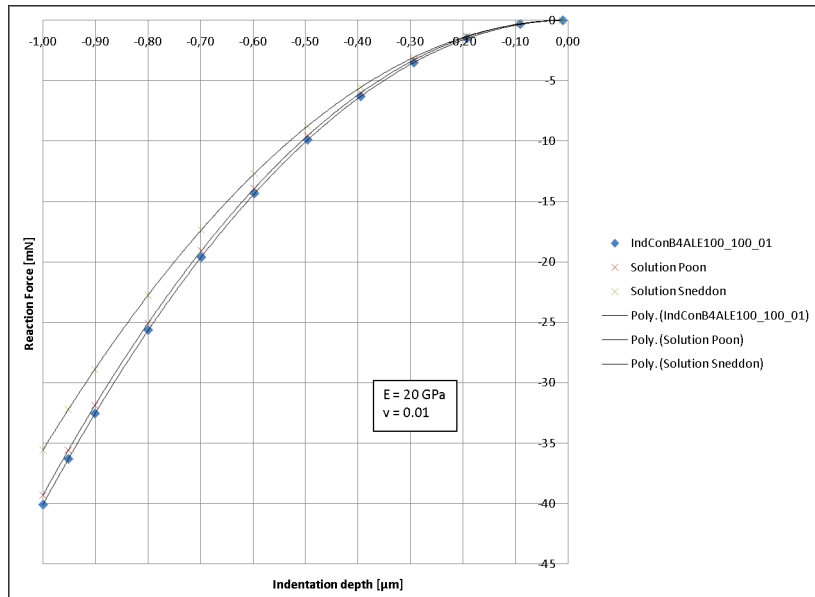

Figure 3.10: Force [mN] vs. displacement [um] for the conical indenter, the analytical solution of Sneddon [Sne48] and the empirical formula by Poon [PRR08b] for $\nu = 0.01$

The force response shows the expected behaviour. The relative error between the FE analysis and the analytical solution by Sneddon is larger than before, as Figure 3.11 shows.
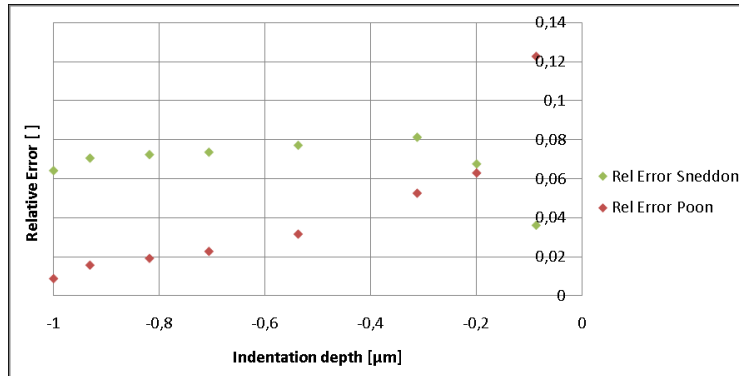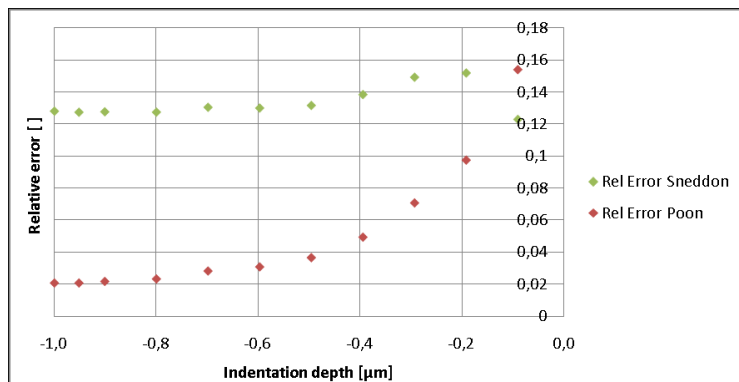

Figure 3.11: Relative error of force response [ ] vs. displacement [μm] with respect to the analytical solution of Sneddon [Sne48] and the empirical formula by Poon [PRR08b] for $\nu = 0.01$

Fig. 3.11 indicates that the error of the numerical solution compared to the analytical solution of Sneddon is approximately constant at 13% for indentation depths larger than 200nm. The relative error towards the empirical formula of Poon that corrects the analytical solution for stiffening effects of the finite tip radius and radial displacements due to the Poisson ratio is about 15% in the beginning. The FE analysis and the empirical solution of Poon [PRR08a] converge with increasing indentation depth to a constant error of 2%.

The isotropic indentation modulus was again evaluated at every increment to verify that the measured modulus is independent of the indentation depth. Fig. 3.12 shows the indentation moduli as a function of indentation depth.
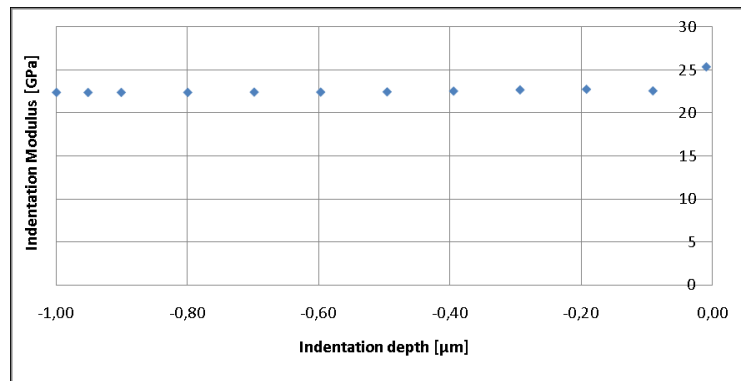
Figure 3.12: Measured indentation modulus [GPa] vs. displacement [μm] for $\nu = 0.01$

Fig. 3.12 again shows that the measured indentation modulus is independent of the indentation depth. For very small indentation depths the error is larger, as the mesh is too coarse to properly compute the exact mechanical response. For indentation depths larger than 100nm, the mesh used in these simulations gives us proper results. On Fig. 3.13 the relative error of the measured indentation moduli is shown as a function of indentation depth.
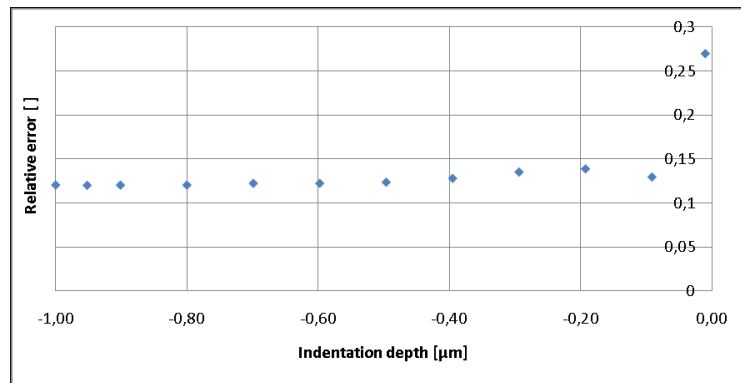
Figure 3.13: Relative measurement error of the indentation modulus [ ] vs. displacement [μm] for $\nu = 0.01$

3.1.3 ILE C

In order to show that the model is able to simulate the indentations for a wide range of Poisson ratios, another simulation using the conical indenter was performed for ILE C, which has a Poisson ratio of 0.49.
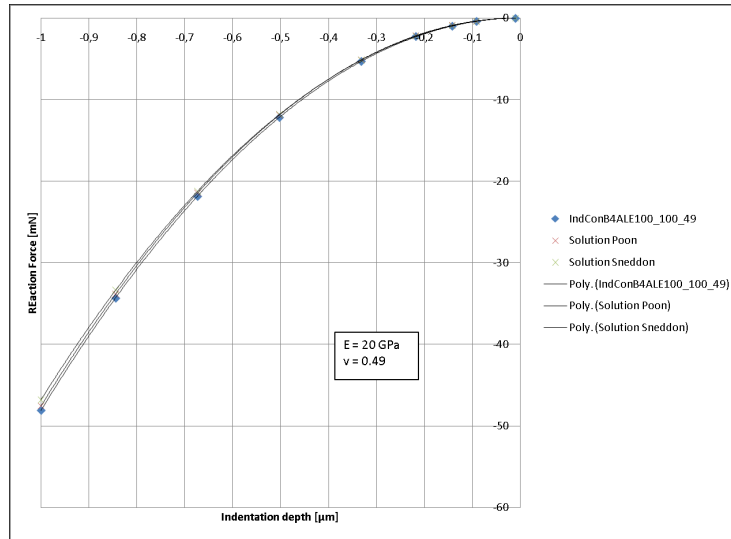
Figure 3.14: Force [mN] vs. displacement [μm] for the conical indenter, the analytical solution of Sneddon [Sne48] and the empirical formula by Poon [PRR08b] for $\nu = 0.49$

The force response shows the expected behaviour. The relative error between the FE analysis and the analytical solution by Sneddon is very small. The accuracy of the simulations is much higher for nearly incompressible materials than for smaller Poisson ratios. This effect was explained by Hay et al [HBP99] with vanishing radial displacements of the surface points inside the contact area for incompressible materials and will be addressed further in section 5.1. Fig. 3.15 shows the relative error of the force response with respect to the analytical solution of Sneddon [Sne48] and the empirical formula of Poon [PRR08a] as a function of indentation depth.
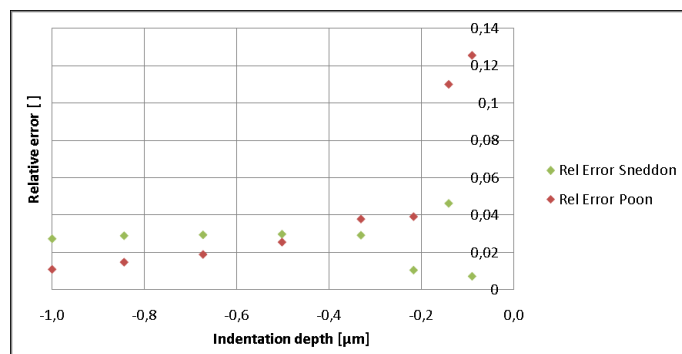
Figure 3.15: Relative error of force response [ ] vs. displacement [μm] with respect to the analytical solution of Sneddon [Sne48] and the empirical formula by Poon [PRR08b] for $\nu = 0.49$

39

Fig. 3.15 indicates that the error of the numerical solution compared to the analytical solution is very small at all indentation depths. The relative error towards the empirical formula of Poon is higher in the beginning. The FE analysis and the empirical solution of Poon [PRR08a] converge with increasing indentation depth.

The indentation modulus was evaluated at every increment one more time to verify that the measured modulus is independent of the indentation depth for this set of material parameters. Fig. 3.16 shows the measured values of the indentation modulus as a function of indentation depth.
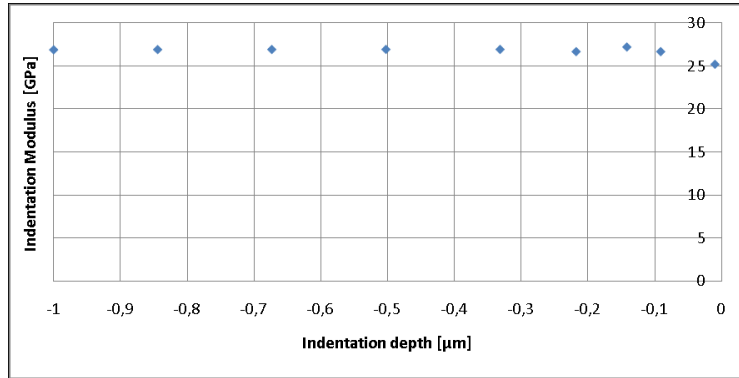
Figure 3.16: Measured indentation modulus [GPa] vs. displacement [μm] for $\nu = 0.49$

Fig. 3.12 shows no dependency of the measured indentation modulus on the indentation depth for this set of material parameters. Fig. 3.17 shows the relative error of the measured elastic moduli vs. indentation depth.
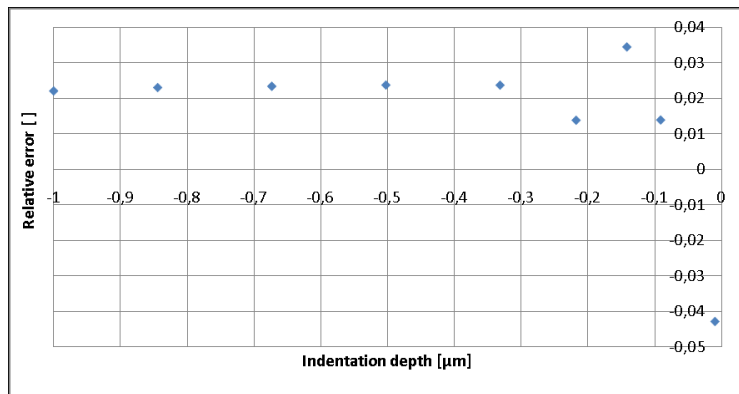
Figure 3.17: Relative measurement error of indentation modulus [ ] vs. displacement [μm] for $\nu = 0.49$

Fig. 3.17 shows no dependency of the relative error of the measured indentation modulus on the indentation depth for this set of material parameters. There is a trend in the data of increasing accuracy of the simulations with respect to the analytical solution by Sneddon [Sne48]. Fig. 3.18 shows a 3D plot of the relative error of the reaction force with respect to the analytical solution by Sneddon as a function of Poisson ratio and indentation depth.
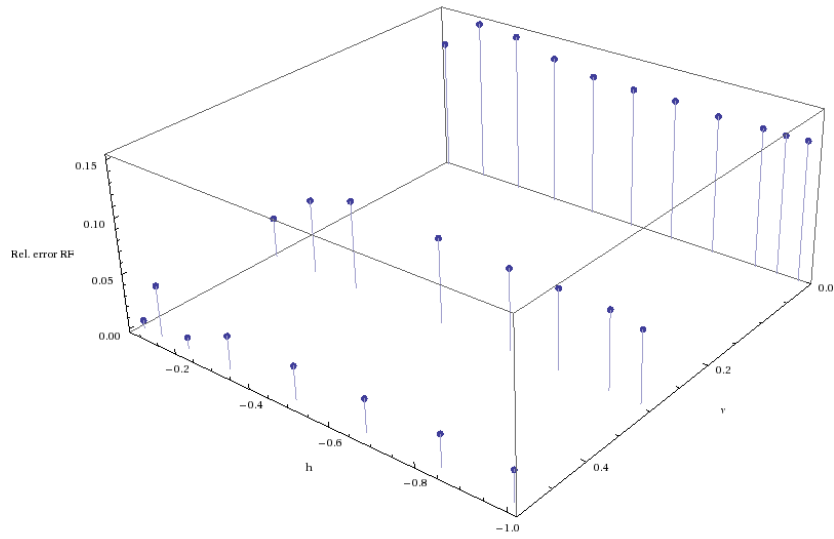
Figure 3.18: Relative error of the reaction force [ ] with respect to the analytical solution by Sneddon as a function of Poisson ratio and indentation depth

Fig. 3.18 suggests that there is a negative relationship between the relative error of the reaction force with respect to Sneddon and the Poisson ratio for all indentation depths larger than 0.2μm. The error is minimal for a Poisson ratio of 0.49. It is constant for all indentation depths larger than 0.2μm. Fig. 3.19 shows a 3D plot of the relative error of the measured indentation modulus as a function of Poisson ratio and indentation depth.
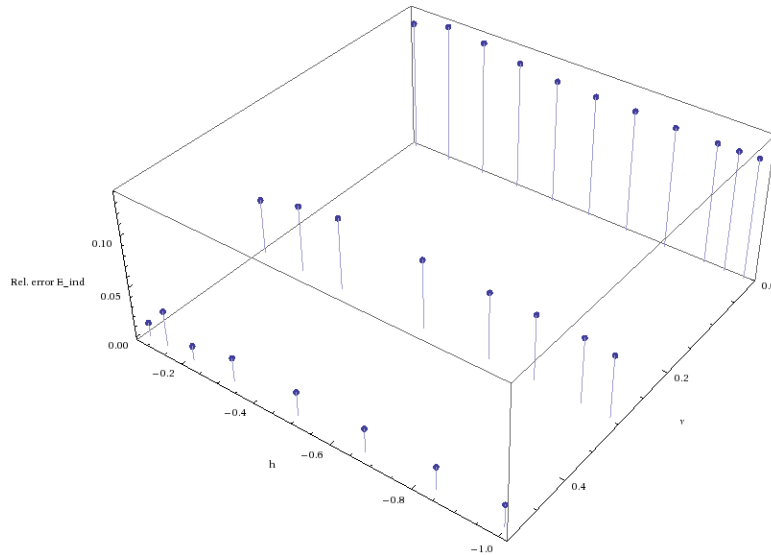
Figure 3.19: Relative error of the indentation modulus [ ] as a function of Poisson ratio and indentation depth

Fig. 3.19 suggests that there is a negative relationship between the relative error of the measured

41

indentation modulus and the Poisson ratio for all indentation depths larger than 0.2μm. The error is minimal for a Poisson ratio of 0.49. It is constant for all indentation depths larger than 0.2μm. This part of the verification showed that the mesh can simulate the mechanical response of an isotropic linearly elastic material with sufficient accuracy at indentation depths larger than 0.2μm.

3.2 Transversely isotropic linear elasticity

As the goal of this study was to use an anisotropic bone model, the mesh was validated for the anisotropic case as well. An indentation of a transverse isotropic elastic halfspace was simulated. The results were compared to the analytical solution by Swadener and Pharr [SP01].

Fig. 3.20 compares the force vs. indentation depth curves of FE simulations of indentations in axial ($\square$) and transverse ($\diamond$) direction to the analytical solution by Swadener and Pharr [SP01].
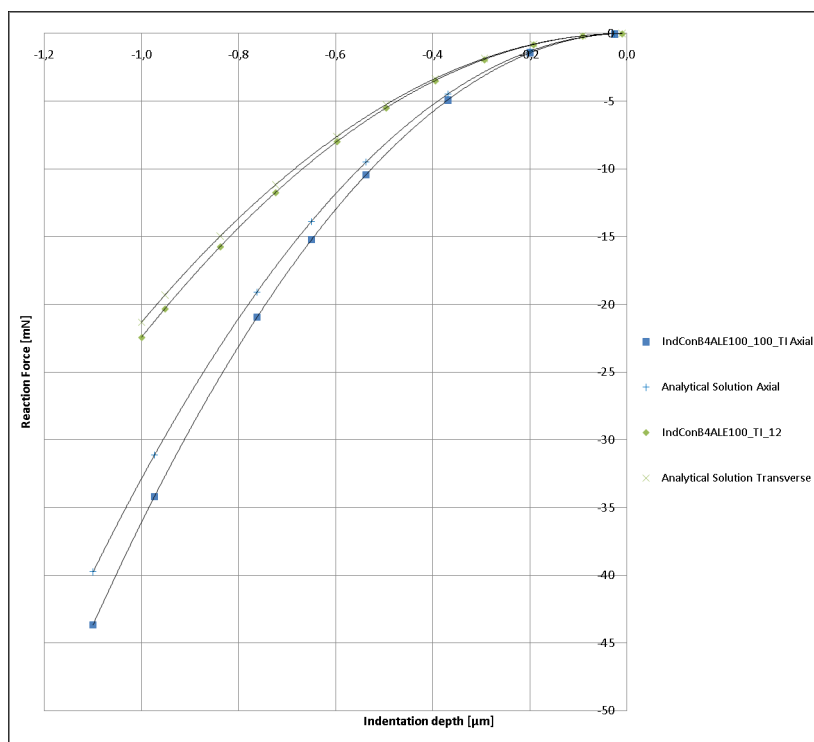
Figure 3.20: Force [mN] vs. indentation depth [μm] in axial ($\square$) and transverse ($\diamond$) direction

Figure 3.21 shows the relative error of the FE analysis in comparison to the analytical solution by Swadener and Pharr [SP01] in axial ($\square$) and transverse ($\diamond$) direction.
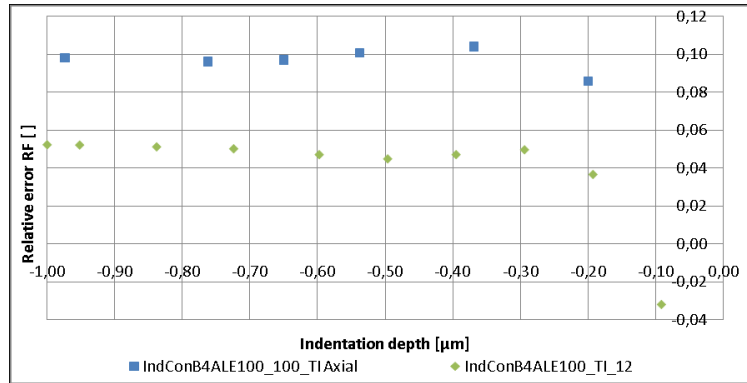
Figure 3.21: Relative error of force response [ ] vs. displacement [μm] in axial (□) and transverse (◇) direction

The relative error in the force response of the system is considerably smaller in transverse than it is in axial direction. The indentation moduli in the axial and transverse direction were extracted using the method of Oliver and Pharr [OP92]. Fig. 3.22 shows the extracted indentation modulus in axial (□) and transverse (◇) direction as a function of indentation depth.
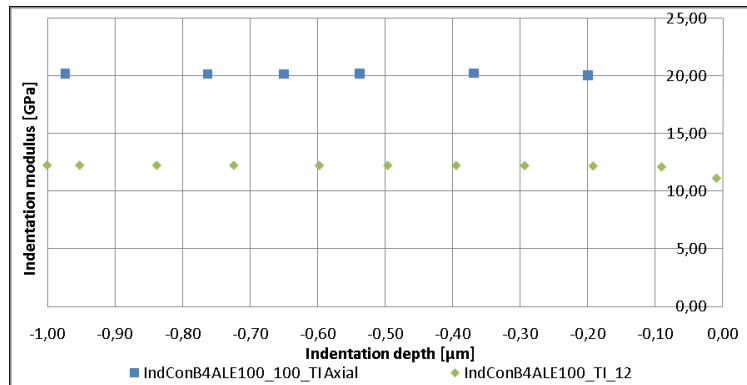
Figure 3.22: Indentation modulus [GPa] vs. indentation depth [μm] in axial (□) and transverse (◇) direction

Fig. 3.22 shows no dependency of the indentation modulus on the indentation depth for this set of material parameters. The theoretical indentation moduli for this material in axial and transverse direction were computed using the mathematical framework of Swadener and Pharr [SP01]. It is $18.48GPa$ in axial direction and $11.99GPa$ in transverse direction. As can be seen in Fig. 3.22, there is a slight overestimation of the modulus in both axial and transverse direction. The relative error was quantified as a function of indentation depth. Fig. 3.23 shows the relative error of the measurement of the indentation modulus in axial (□) and transverse (◇) direction as a function of indentation depth.

43
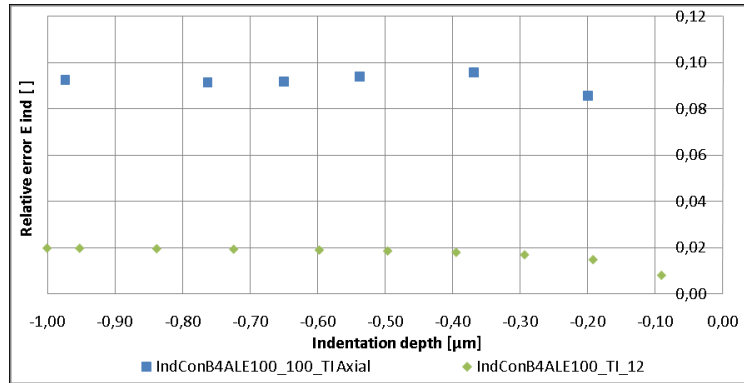
Figure 3.23: Relative error of indentation modulus [ ] vs. indentation depth [μm] in axial ($\square$) and transverse ($\diamond$) direction

Fig. 3.23 shows no dependency of the relative error of the measured indentation modulus on the indentation depth for this set of material parameters. The relative error in the extracted indentation modulus is considerably smaller in transverse than it is in axial direction. The mesh used in these simulations can simulate the mechanical response of the system properly at all indentation depths.

3.3 Isotropic elasto-plasticity

The mesh was validated for an isotropic elastic ideal plastic material law as well by comparing it to the results of a numerical study conducted by Poon [PRR08b]. The material IEP A was used, which features an elastic modulus of 50GPa, a Poisson ratio of 0.3 and ideal Mises (J2) plasticity with a yield stress of 1GPa. The finite tip radius was changed to 30nm for this experiment. The indentation depth was 600nm. This coincides with the parameters used by Poon [PRR08b] for a numerical experiment in 2008. Fig.3.24 shows the indentation curve of the simulation with 216000 elements ($\diamond$) and the convergence study with 432000 elements ($\times$).
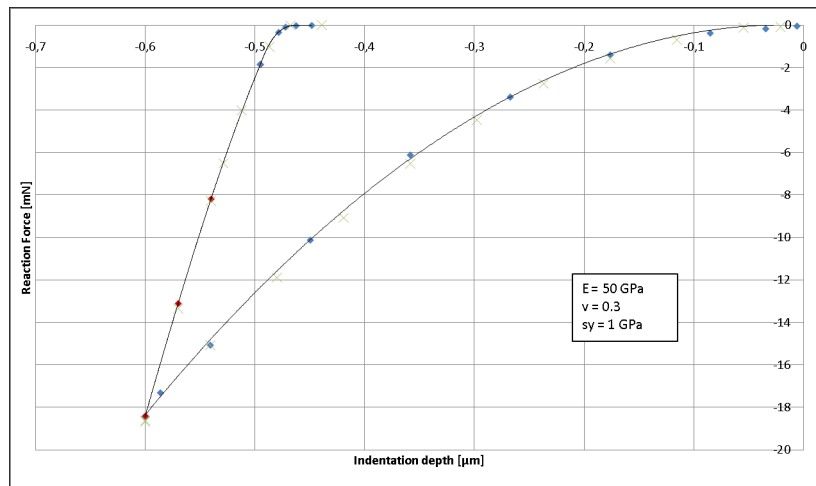
Figure 3.24: Force [mN] vs. displacement [μm] of the simulation ($\diamond$) and the convergence study ($\times$)

44

The elastic modulus was extracted at the beginning of the unloading phase using the method proposed by Oliver and Pharr 1992 [OP92] assuming a Poisson's ratio of 0.3. It was compared to the original value of 50GPa used for the material definition in Abaqus. The extracted modulus was 57.48GPa at a depth of 600nm. This corresponds to a relative error of 14.96%. The extracted modulus reported by Poon [PRR08b] was 56.7GPa, which corresponds to a relative error of 13.3%. The relative error in the extraction of the modulus of the simulations performed in this study to the reported values of Poon was 1.377%. A convergence study was done by refining the mesh by a factor of two. 432000 elements were used instead of 216000. Table 3.3 compares the results of this study and those obtained by Poon [PRR08b] with the original modulus of the material. The results of the convergence study can be seen as well.

	h_{max}	E [GPa]	Rel. error
Orig.		50.0	
Poon	0.6	56.7	+13.3
IEP A	0.6	57.5	+14.96
Conv. St.	0.6	57.1	+14.23

Table 3.1: Extracted elastic moduli [GPa] and relative error of moduli reported by Poon [PRR08b], for IEP A and the convergence study

The results of the simulations using the material IEP A were very similar to those obtained by Poon. The convergence study showed only minor differences in the indentation curves. The relative error in the maximum force was 1.13% in the convergence study. The relative difference in the extracted modulus was 0.6% between the simulations with 216000 and 432000 elements. Therefore there is no significant increase in solution accuracy with decreased element size. The computation time and memory consumption however increased significantly. Therefore it was concluded that the mesh is able to simulate indentations on isotropic elasto-plastic material with a sufficient accuracy.

3.4 Anisotropic elasto-plasticity and damage

As material laws for the materials AEPDI and AEPDE are not included in the Abaqus material, a new user subroutine (UMAT) had to be implemented in FORTRAN for each of them. In order to verify the correct function of the algorithm, single element tests in ABAQUS were compared to results for homogeneous strain fields obtained in Mathematica (Wolfram Research, Champaign, IL, USA). Periodic boundary conditions were used in order to achieve a homogeneous strain state inside the element for the Abaqus single element tests. For the Mathematica calculations, the strain state was assumed to be homogeneous. For more information on the Mathematica code, see Appendix B. Fig. 3.25 shows the stress strain curve for a uniaxial compression cycle on the material AEPDI.
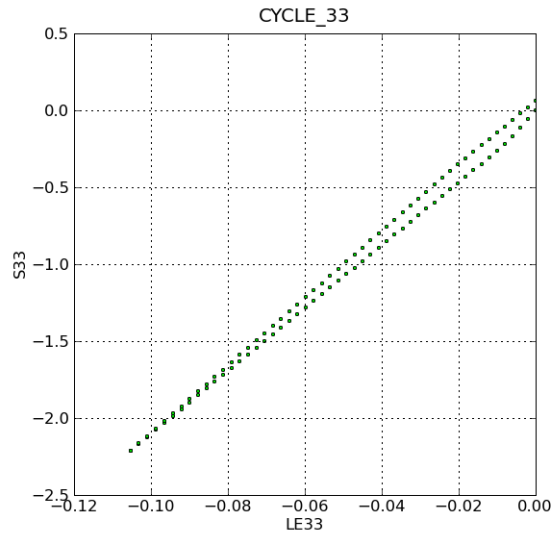
Figure 3.25: Stress [GPa] vs. strain [ ] for an uniaxial compression cycle

As can be seen in Fig. 3.25, the material shows considerable hardening in uniaxial compression. This result was expected, as the constant part of the stiffness matrix has non-zero elements only in the first quadrant of the 6x6 stiffness matrix. The shape of the stress-strain curve was verified in Mathematica. As the shear components of the stiffness matrix can be fully damaged, a simple shear test was performed next in order to visualize the elasto-plastic behaviour with damage. Fig. 3.26 shows the stress strain curve for a simple shear cycle on the material AEPDI.
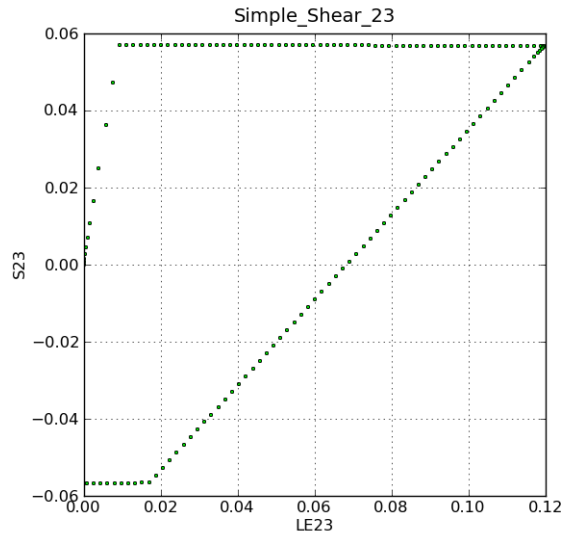
Figure 3.26: Stress [GPa] vs. strain [ ] for a simple shear cycle with ideal plasticity

As can be seen in Fig. 3.26, there is a residual strain showing the influence of the plasticity. As expected for ideal plasticity, no hardening occurs. The stiffness decreases in the course of the loading cycle showing the influence of damage accumulation. The shape of the stress-strain curve was verified in Mathematica. In order to show that a subsequent loading path will follow the preceding unloading path in the elastic case, multiple simple shear cycles were performed. Fig. 3.27 shows the stress strain curve for multiple simple shear cycles on the material AEPDE.
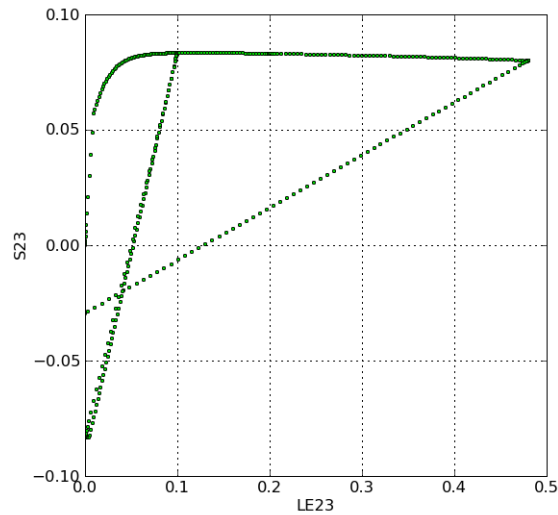
Figure 3.27: Stress [GPa] vs. strain [ ] for multiple simple shear cycles with exponential hardening

As can be seen in Fig. 3.27, a residual strain remains after unloading showing the influence of plasticity. The exponential form hardening curve is very clear. The stiffness decreases in the course of the loading cycles showing the influence of damage accumulation. The subsequent loading path followed the preceding unloading path until the yield criterion was reached. The shape of the stress-strain curve was verified in Mathematica. Fig. 3.28 shows the linear elastic response of the material AEPDE to the eigentensorial state as described in section 2.4.5.
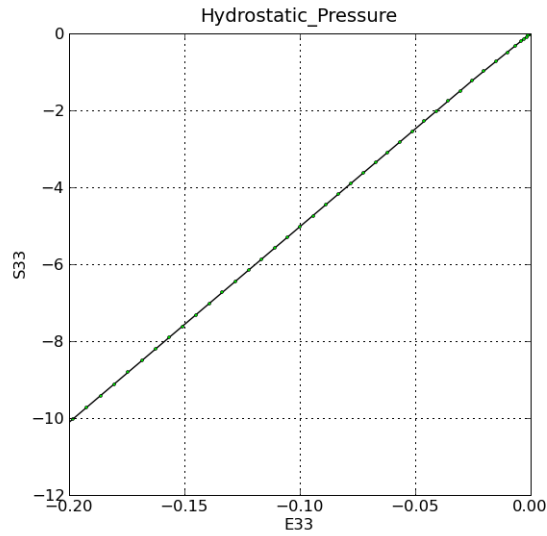
Figure 3.28: Stress [GPa] vs. strain [ ] for eigentensorial state

The mechanical response to the eigentensorial state was strictly linearly elastic, as expected from this particular material model. Multiple more tests were performed and compared quantitatively to the results computed in Mathematica in order to verify the implementation of the algorithm. The results were identical. The convergence rate of the material was tested in another simulation. A cubic sample with 125 elements was tested under unconfined compression. The residual force reported in the msg file decreased by a minimum factor of 10^2 per increment. The convergence rate was quadratic. This result was expected for the full Newton algorithm. Therefore the implementation of the tangent stiffness operator seems to work properly. These tests showed that the implementation of the material law in FORTRAN is working with sufficient accuracy and at a proper convergence rate.

Chapter 4

Results

4.1 Isotropic elasto-plasticity

First, cortical bone was modeled as an isotropic elastic ideal plastic material. The material IEP B was used for this part of the study. It features an elastic modulus of 20GPa, a Poisson ratio of 0.3 and a yield stress of 175MPa in tension and compression. Simulations with different indenter shapes were performed and the results were compared to each other.

4.1.1 Conical indenter

For the conical indenter, simulations of indentations to depths of 600nm and 1μm were performed in order to show the influence of indentation depth on the extracted elastic properties. The elastic modulus was extracted at the beginning of the unloading phase using the method of Oliver and Pharr [OP92] assuming a Poisson's ratio of 0.3. The elastic modulus was chosen in this case in order to be able to compare the results to the study by Poon. Fig.4.1 shows the indentation curves for the indentations to depths of 600nm and 1μm.
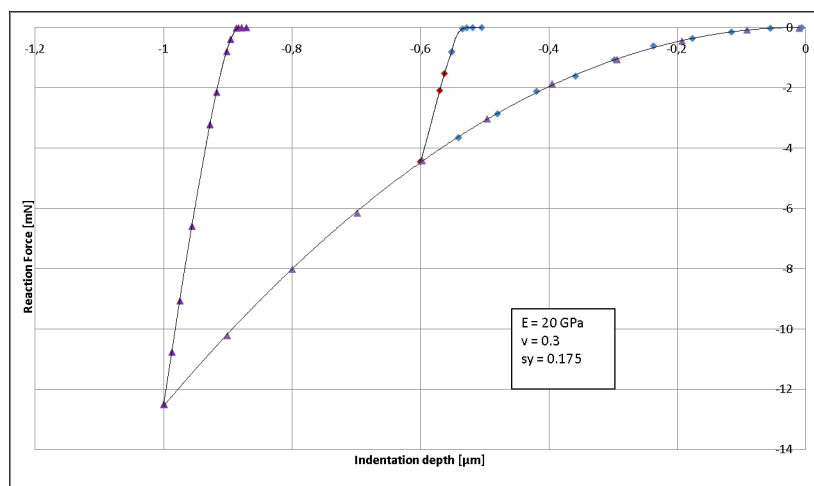
Figure 4.1: Force [mN] vs. Displacement [μm]

The extracted elastic modulus at a depth of 600nm was 24.986GPa. This corresponds to a

relative error of 24.93%. At a depth of 1μm, the extracted modulus was 26.11GPa. This corresponds to a relative error of 30.54%. Table 4.1.1 shows the results of the study.

h_{max}	h_f/h_{max}	h_c	E	Rel. error
0.6	0.840	0.563	24.986	+24.93%
1.0	0.871	0.940	26.11	+30.54%

Table 4.1: Extracted elastic moduli as a function of indentation depth for IEP B ($E/\sigma_y = 114.28$)

The relative error of the extracted moduli were significantly higher for the Material IEP B than for IEP A. For an indentation depth of 0.6μm, 14.96% were reported for IEP A and 24.93% for IEP B. This is a significant increase in measurement error. Similar findings were reported by Poon [PRR08b]. Poon reported a dependency of the measurement error on the ratio of the elastic modulus and the yield strength $\frac{E}{\sigma_y}$. This ratio was 50 for IEP A and 114.28 for IEP B. This coincides very well with data by Poon [PRR08b], who reported a measurement error of 13.3% for $\frac{E}{\sigma_y} = 50$ and 22.5% for $\frac{E}{\sigma_y} = 100$ for materials with a Poisson ratio of 0.3 at an indentation depth of 0.6μm. Bolshakov et al reported similar results [BP98]. For materials with a ratio of h_f/h_{max} larger than 0.7, as it is the case in this study, Bolshakov et al reported considerable overestimation of the elastic modulus due to the increased contact area because of material pile-up. Table 4.1.1 compares the results reported in this study to those of Poon.

	E/σ_y	Rel. error
IEP A	50	14.96%
Poon A	50	13.3%
IEP B	114.28	24.93%
Poon B	100	22.5%

Table 4.2: Measurement error of elastic moduli and $\frac{E}{\sigma_y}$ of this study and reported by Poon [PRR08b]

Contour plots of the von Mises stress and the plastic equivalent strain on the deformed shape at a depth of 1μm were plotted. Fig.4.2 shows the contour plot of the von Mises stresses on the deformed mesh.
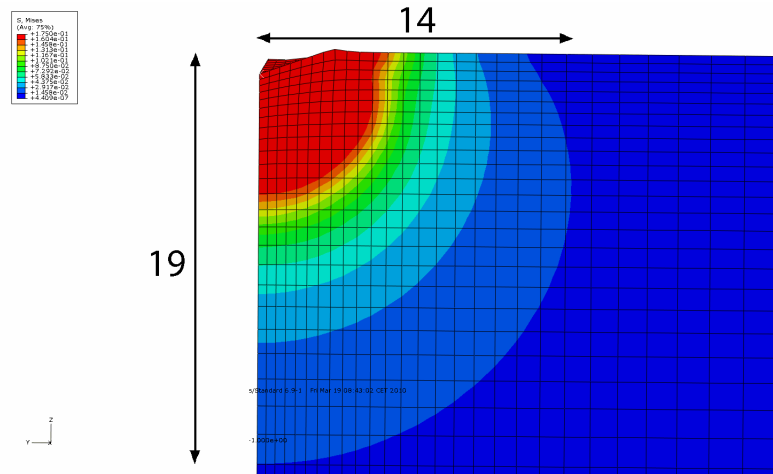
Figure 4.2: Von Mises stress [GPa] on deformed shape (Max: 175MPa, Min: 14.5MPa)

The maximum stress under the indenter is 175MPa. This result was expected, as IEP B features perfect plasticity with a yield stress of 175MPa. The stress at a depth of 19μm and at 14μm distance from the indentation center is still 14.5MPa. The plastic zone stretches further than the contact zone of the indenter resulting in a considerable amount of pile-up. This coincides very well with the results of Bolshakov et al [BP98]. The stress field is axisymmetric and about 30% longer in axial direction than in radial direction. Fig.4.3 shows the contour plot of the plastic equivalent strains on the deformed mesh.
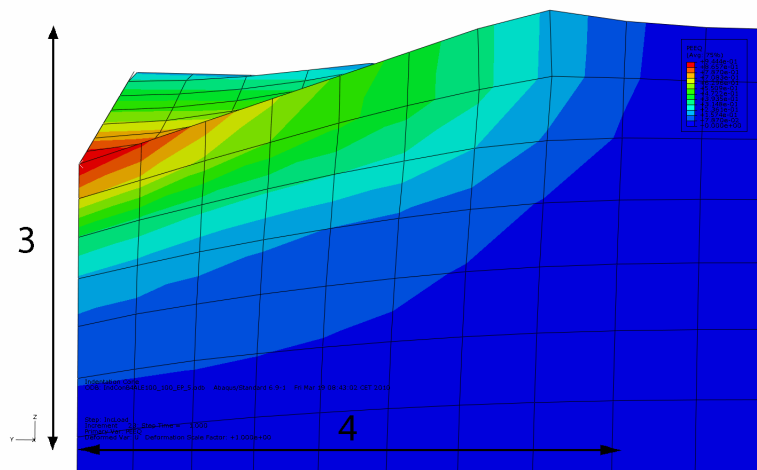
Figure 4.3: Plastic equivalent strain on deformed shape (Max: 0.944, Min: 0.079)

The maximum equivalent plastic strain under the indenter tip is 0.944. The equivalent plastic strain at a depth of 3μm and at 4μm distance from the indentation center is still 0.079. The plastic strain field is axisymmetric and about 25% shorter in axial direction than in radial direction. There is a considerable amount of material pile-up around the indenter. This effect was also reported by Poon [PRR08b] and Mullins et al. [MBM09]. The height of the pile-up is constant around the perimeter. It should be noted that the Material IEP B used in this simulation features perfect

plasticity, which might play a decisive role for the amount of pile-up around the indentation as reported by Bolshakov et al [BP98]. Also, contour plots of the residual von Mises stress and the plastic equivalent strain after retraction of the indenter were plotted. Fig.4.4 shows the contour plot of the residual von Mises stresses on the deformed mesh.
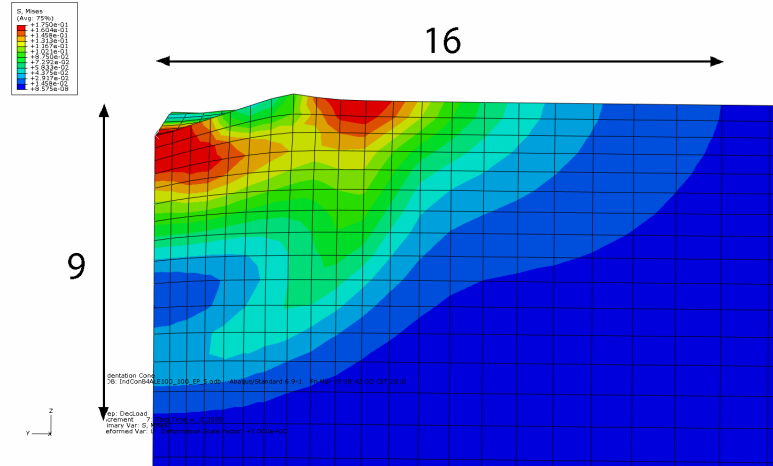
Figure 4.4: Residual von Mises stress [GPa] (Max: 175MPa, Min: 14.5MPa)

The maximum residual von Mises stress is 175MPa. This is equivalent to the yield stress of the material IEP B. The yield stress is reached under the indenter tip as well as at about 5μm distance from the indentation center right next to the remaining pile-up at the vicinity of the plastic imprint. The stress at a depth of 9μm and at 16μm distance from the indentation center is still 14.5MPa. The stress field is axisymmetric and about half as long in axial direction as in radial direction. The shape of the stress field changed significantly during unloading. Fig.4.5 shows the contour plot of the plastic equivalent strains on the deformed mesh.
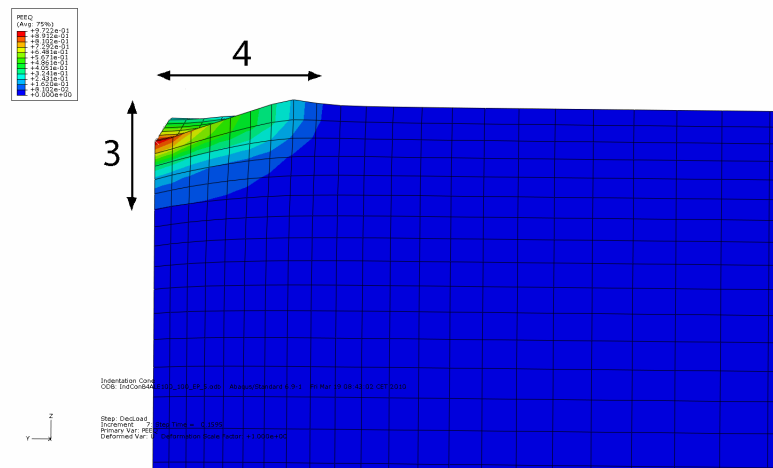
Figure 4.5: Residual plastic equivalent strain (Max: 0.972, Min: 0.081)

The maximum residual equivalent plastic strain under the indenter tip is 0.972. The residual

equivalent plastic strain at a depth of 3μm and at 4μm distance from the indentation center is still 0.081. The plastic strain field is axisymmetric and about 25% shorter in axial direction than in radial direction. It should be noted that the residual equivalent plastic strain increased by about 3% during unloading. This result was not expected, as the unloading curve is supposed to be purely elastic according to Oliver and Pharr [OP92]. The shape of the plastic strain field remained approximately the same. It should be noted that even though Fig. 4.4 suggests that the yield stress is reached in the area at about 5μm distance from the indentation center right next to the pile-up at the vicinity of the residual plastic imprint, there is no significant residual plastic strain reported in this area.

4.1.2 Berkovich indenter

For the Berkovich indenter, a simulation to a depth of 600nm was performed and compared to the solution of the conical indenter. This was done to assess whether the conical indenter with equal projected area is an appropriate substitute in simulations for the Berkovich indenter. The elastic modulus was extracted at the beginning of the unloading phase using the method of Oliver and Pharr [OP92] assuming a Poisson's ratio of 0.3. Fig.4.6 compares the indentation curves for the indentations of the Berkovich indenter ($\diamond$) and of the conical indenter ($\triangle$) to a depth of 600nm.
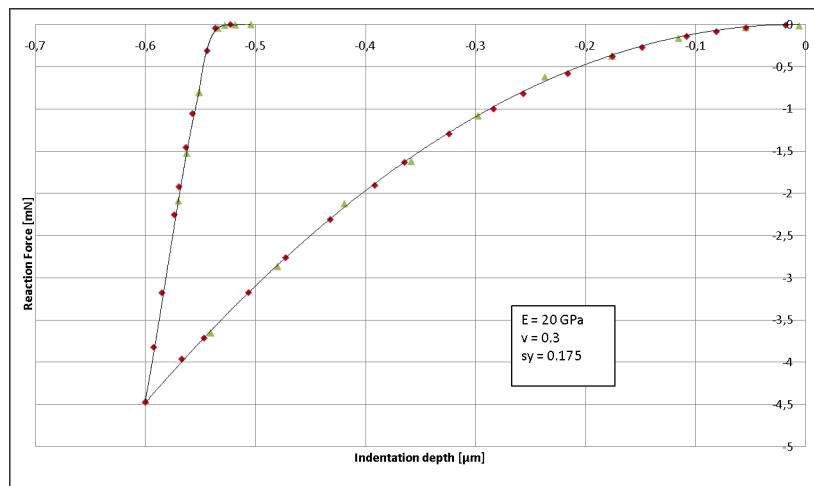
Figure 4.6: Force [mN] vs. displacement [μm] of the Berkovich indenter ($\diamond$) and of the conical indenter ($\triangle$)

As you can see in Fig.4.6, the force-displacement curves coincide very well for the two indenter shapes. The elastic modulus was extracted using the method of Oliver and Pharr. Table 4.1.2 compares important measurements of the indentations for the conical and the Berkovich indenter.

Ind.shape	h_{max}	h_f/h_{max}	h_c	E	Rel. error
Conical	0.6	0.840	0.563	24.986	+24.93%
Berkovich	0.6	0.870	0.564	24.812	+24.06%

Table 4.3: Comparison of indentations on IEP B ($E/\sigma_y = 114.28$) with a conical and a Berkovich indenter

The extracted moduli are almost identical for both indenters, if the empirical correction factor β [PRR08b] is used. The depth of the residual plastic imprint h_f is very similar for both indenters. Note that the ratio $h_f/hmax$ is larger than 0.7 for both indenters. The contact depth h_c at h_{max} is almost equal for the Berkovich and the conical indenter. This suggests that the assumption of the conical indenter with equivalent projected area being a good substitute to the Berkovich indenter in simulations was reasonable. The local stress distribution in close proximity of the indenter tip is very different for the Berkovich indenter. However, at a short distance from the indenter the stress state is axisymmetric. This will be presented on the following pages. Fig.4.7 shows the contour plot of the von Mises stress on the deformed mesh at an indentation depth of $0.6\mu m$.
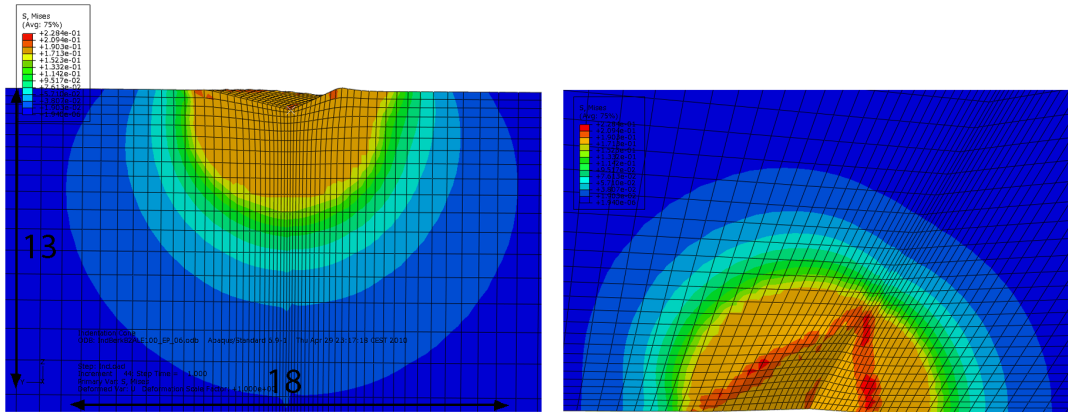
Figure 4.7: Contour plot of the von Mises stress [GPa] on the deformed shape (side and top view, Max: 228.4MPa, Min: 19.0MPa)

The maximum von Mises stress under the indenter tip is 228.4MPa. The von Mises stress at a depth of $13\mu m$ and at $9\mu m$ distance from the indentation center is still 19MPa. The far stress field is approximately axisymmetric and about 25% longer in axial direction than in radial direction. It should be noted that the pile-up around the Berkovich indenter has a considerably different shape than around the conical indenter. There is considerable pile-up in the middle of each side of the indenter. This is similar to the results of the conical indenter. However, the pile-up decreases dramatically from the middle of the sides towards the edges. Right at the edges, slight sink-in could be seen. Fig.4.8 shows the contour plot of the plastic equivalent strain on the deformed mesh at an indentation depth of $0.6\mu m$.
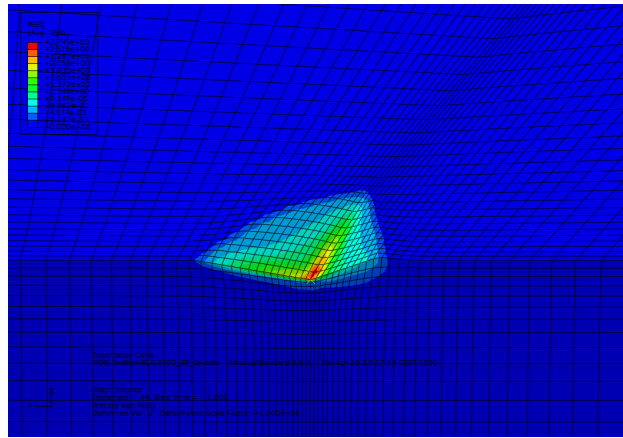
Figure 4.8: Contour plot of the plastic equivalent strain [ ] on the deformed shape (Max: 2.75, Min: 0.23)

The maximum equivalent plastic strain under the indenter tip is 2.75. The equivalent plastic strain at a depth of about 1μm and at 4μm distance from the indentation center is still 0.23. Fig.4.9 shows the contour plot of the residual von Mises stress on the deformed mesh after unloading.
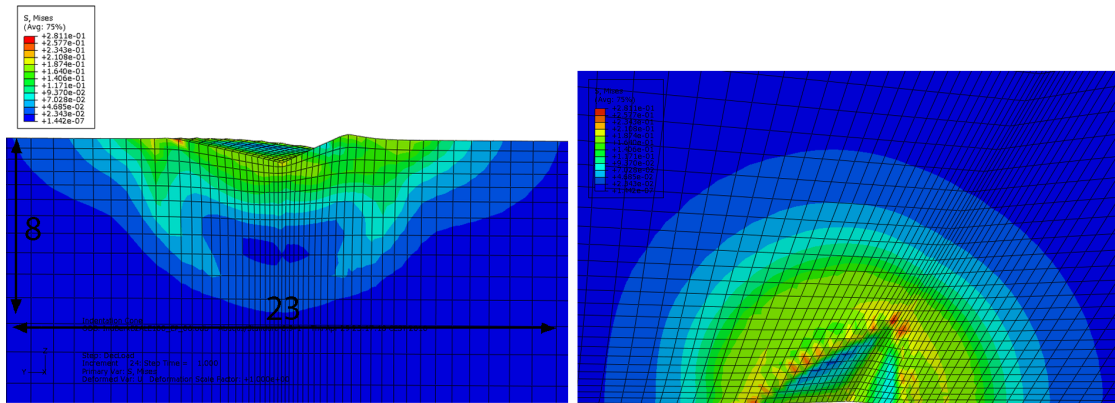
Figure 4.9: Contour plot of the residual von Mises stress [GPa] on the deformed shape (side and top view, Max: 281.1MPa, Min: 23.4MPa)

The maximum residual von Mises stress under the indenter tip is 281.1MPa. The residual von Mises stress at a depth of 8μm and at 12μm distance from the indentation center is still 23.4MPa. The far stress field is approximately axisymmetric and about 50% shorter in axial direction than in radial direction. The indentation curves of the two indenters are practically identical. The error in the measured modulus is negligible. This shows that the assumption of the conical indenter with equivalent projected area being a good substitute to the Berkovich indenter in simulations is reasonable, at least for isotropic elasto-plasticity.

4.2 Anisotropic elasto-plasticity

Two simulations of indentations in axial and transverse direction were performed for the anisotropic elastic ideal plastic material AEP. Fig. 4.10 shows the reaction force vs. indentation depth of the axial tests to an indentation depth of $0.6\mu m$ and $1.0\mu m$, respectively.
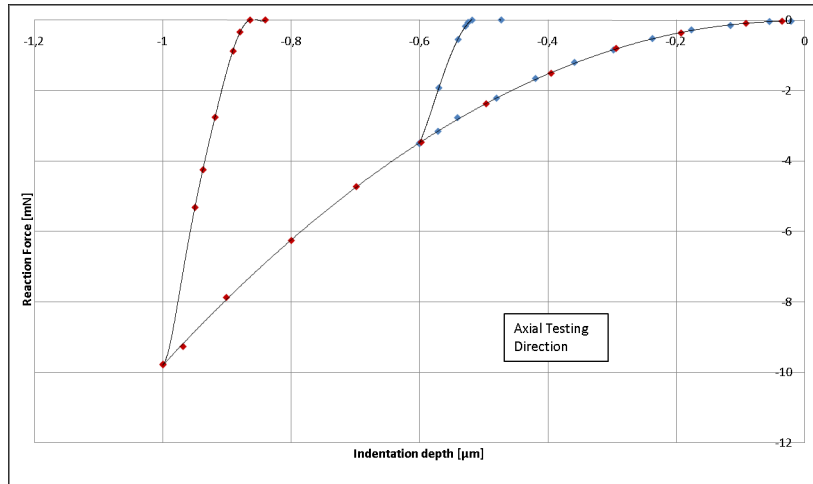
Figure 4.10: Force [mN] vs. displacement [μm] of axial indentation

The indentation moduli in axial direction were extracted from these curves using the method of Oliver and Pharr [OP92]. Using the original stiffness matrix from the Abaqus material definition and the theoretical framework of Swadener and Pharr [SP01], theoretical indentation moduli were calculated for the axial and transverse direction. The experimental results were then compared to the theoretical values. Table 4.2 shows the extracted indentation modulus in axial direction and the relative error with respect to the theoretical modulus as a function of indentation depth.

h_{max}	h_f/h_{max}	h_c	E_i	Rel. Error
Orig.			15.49	
0.6	0.788	0.556	18.51	$+19.51\%$
1.0	0.841	0.929	19.09	$+23.26\%$

Table 4.4: Extracted axial indentation modulus and relative error for AEP ($E_0/\sigma_{y,0} = 88.5$)

The relative error in the measurement of the indentation moduli is smaller for the material AEP in axial direction than in the isotropic case. The ratio h_f/h_{max} is larger than 0.7 for both indentation depths in axial direction. However, the ratio is smaller than in the isotropic case. This correlates well with studies performed by Bolshakov er al [BP98] with isotropic materials, who predict an increase of the relative measurement error of the indentation modulus with increasing h_f/h_{max}. Fig. 4.11 shows the von Mises stress distribution and the deformed shape in the 1-3 and the 2-3 plane in axial direction to an indentation depth of $1\mu m$.

56
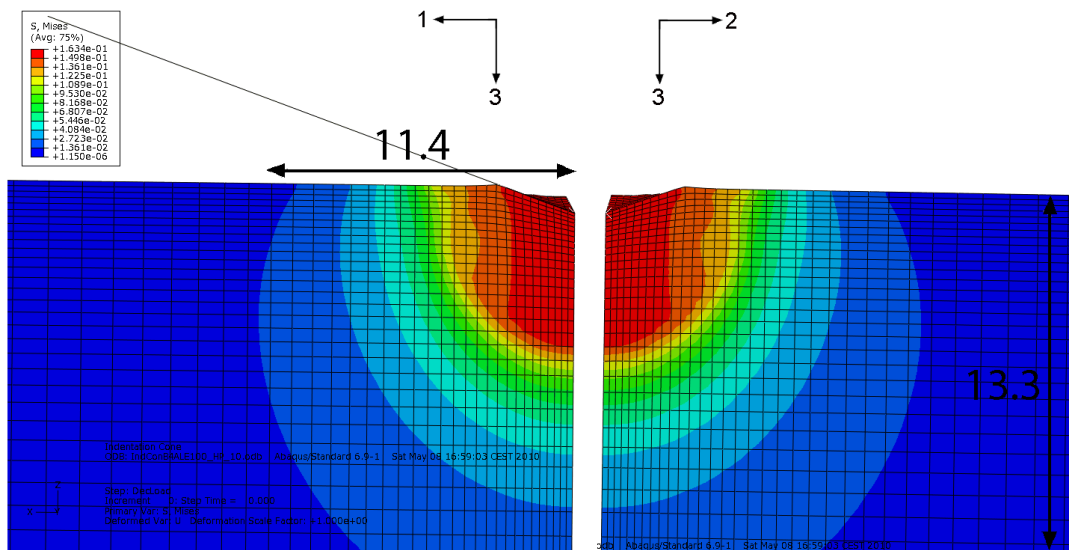
Figure 4.11: Contour plot of von Mises stress distribution $[GPa]$ for an indentation in axial direction on deformed shape in the 1-3 (left) and 2-3 (right) plane (Max: 163.4MPa, Min: 13.6MPa)

The figure clearly shows that the shape of the contact area of the indentation is axisymmetric. The contact depth is constant. The maximum von Mises stress under the indenter tip is 163.4MPa. The von Mises stress at a depth of 13.3μm and at 1.4μm distance from the indentation center is still 13.6MPa. The stress field is axisymmetric. There is some pile-up visible around the indenter. The amount of pile-up is considerably smaller than in the isotropic case. This correlates very well with findings of Bolshakov er al [BP98], who predict an decrease of pile-up with decreasing h_f/h_{max}. The height of the pile-up is constant around the perimeter, as the indentation direction is normal to the plane of isotropy. It should be noted that the Material AEP used in this simulation features ideal plasticity, which might play a decisive role for the amount of pile-up around the indentation as reported for isotropic elasto-plasticity by Bolshakov et al [BP98].

Fig. 4.12 shows the reaction force vs. indentation depth of the tests in transverse direction until a indentation depths of 0.6μm and 1.0μm.
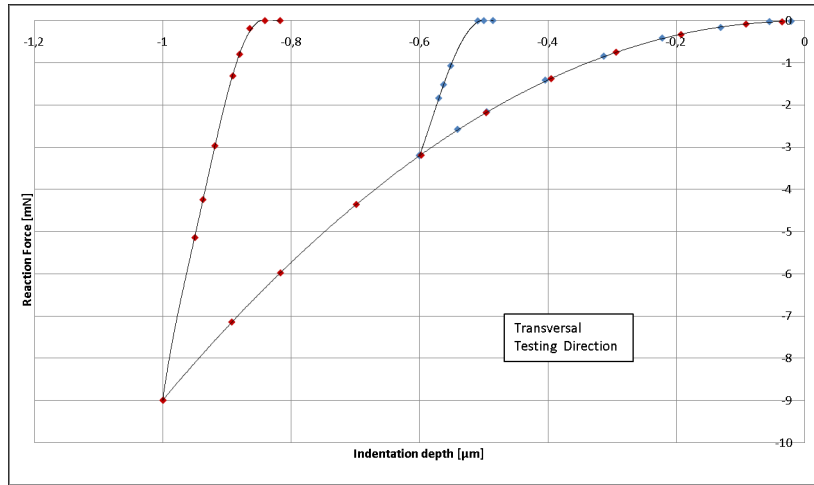
Figure 4.12: Force [mN] vs. Displacement [μm] of transverse indentation

The indentation moduli were extracted in transverse direction as well using the method of Oliver and Pharr [OP92]. Using the original stiffness matrix from the Abaqus material definition and the mathematical framework of Swadener and Pharr [SP01], indentation moduli were calculated for the transverse direction once again. The experimental results were then compared to the theoretical values. Table 4.2 shows the extracted indentation modulus in transverse direction and the relative error with respect to the theoretical modulus as a function of indentation depth.

h_{max}	h_f/h_{max}	h_c	E_i	Rel. Error
Orig.			13.21	
0.6	0.808	0.556	16.73	+26.68%
1.0	0.817	0.925	16.77	+26.99%

Table 4.5: Extracted transverse indentation modulus and relative error for AEP ($E_0/\sigma_{y,0} = 88.5$)

The relative error in the measurement of the indentation moduli was about the same for the material AEP in transverse direction as in the isotropic case. The ratio h_f/h_{max} is larger than 0.7 for both indentation depths in transverse direction. The relative error of the extracted indentation moduli is in the range of 19 to 27%. There is a significant increase in the overestimation of the indentation modulus with increasing indentation depth in axial direction. There is no remarkable trend in the transverse direction. The relative error was considerably larger in transverse direction than in axial direction. Fig. 4.13 shows the von Mises stress distribution and the deformed shape in the 1-2 (right) and the 2-3 plane (left) for the indentation in transverse direction to an indentation depth of $1\mu m$.

Figure 4.13: Contour plot of von Mises stress distribution $[GPa]$ for an indentation in transverse direction on deformed shape in the 1-2 (left) and 2-3 (right) plane (Max: 161.8MPa, Min: 13.5MPa)

The figure clearly shows that the shape of the contact area of the indentation is not axisymmetric. The contact depth is varying over the perimeter. The highest stress is not centered under the indenter tip, but displaced by about 4μm in the material's 3 direction. This is most probably an effect of the anisotropy of the material. The pile-up at the edges of the indentation is considerably larger in the plane of isotropy (1-2 plane) than in the 2-3 plane. There is a stress concentration visible in the 2-3 plane at a distance of about 4μm that stretches from the surface to a depth of about 5μm. The maximum von Mises stress under the indenter tip is 134.8MPa. The maximum von Mises stress at the stress concentration in the 2-3 plane is 161.8MPa. The von Mises stress at a depth of about 14μm and at 10.2μm distance from the indentation center in the 2-3 plane and 11.3μm distance from the indentation center in the 1-2 plane is still 13.5 MPa. The stress field is not axisymmetric.

The contact shape of the indenter is approximately an ellipse in the indentation of a conical indenter into an anisotropic half space as predicted in theory by Swadener and Pharr [SP01]. The contact depth varies around the perimeter. In the case of the axial indentation on an transversely isotropic half-space the contact shape is circular and the contact depth is constant. In transverse direction the pile-up at the edges of the is considerably larger in the directions with smaller elastic modulus.

4.3 Anisotropic elasto-plasticity and damage

Indentations were performed on two different materials using the conical indenter model. First, the material AEPDI featuring ideal plasticity was indented in axial (3) and transverse (1) direction. Then, exponential hardening was introduced.

4.3.1 Perfect plasticity

Two simulations of conical indentations in axial and one transverse direction were performed for the anisotropic elasto-plastic material with damage accumulation AEPDI to an indentation depth of

0.6μm. Fig. 4.14 shows the reaction force vs. indentation depth of the axial test to an indentation depth of 0.6μm.
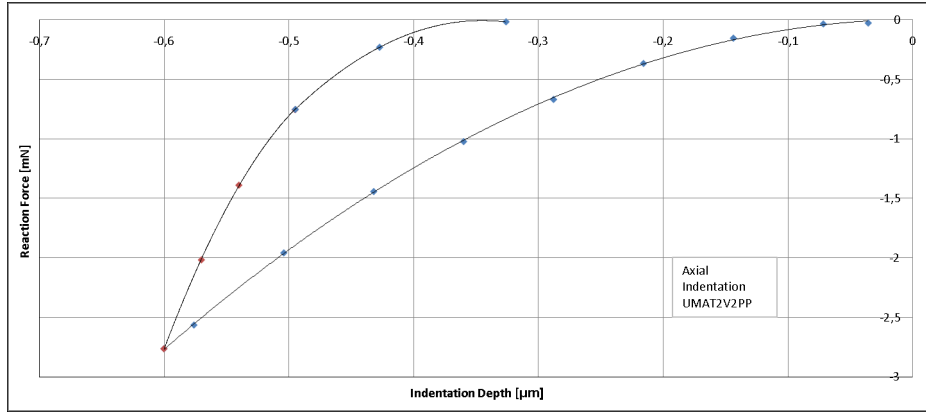
Figure 4.14: Reaction Force [mN] vs. Displacement [μm] for axial indentation of a conical indenter

This indentation curve looks qualitatively much more similar to experimental indentation curves on bone than Fig. 4.10. The indentation moduli were extracted as well. Using the original stiffness matrix from the Abaqus material definition and the mathematical framework of Swadener and Pharr [SP01], exact indentation moduli were calculated for the Material AEPDI. The results of the simulation were then compared to the theoretical value. Table 4.3.1 shows the extracted indentation modulus in axial direction and the relative error with respect to the theoretical modulus.

h_{max}	h_f/h_{max}	h_c	E_i	Rel. Error
Orig.			19.50	
0.6	0.207	0.528	9.40	-51.81%

Table 4.6: Extracted axial indentation modulus and relative error for ideal plasticity

The extracted indentation modulus is heavily underestimated in axial direction. The ratio h_f/h_{max} is considerably smaller than 0.7 in axial direction. The ratio is also much smaller than for the simulations featuring anisotropic elasto-plasticity. Fig. 4.15 shows the reaction force vs. indentation depth of the test in transverse (1) direction to an indentation depth of 0.6μm.
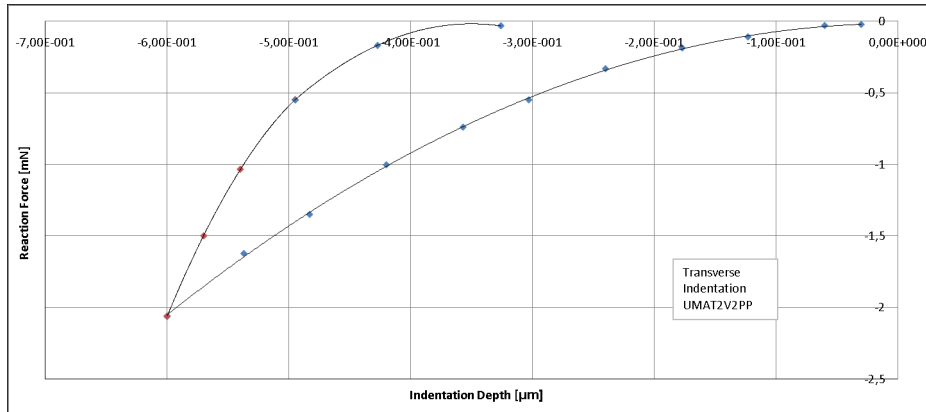
Figure 4.15: Reaction Force [mN] vs. Displacement [μm] for transverse indentation with perfect plasticity

Table 4.3.1 shows the extracted indentation modulus in transverse (1) direction and the relative error with respect to the theoretical modulus for the elastic ideal plastic material AEPDI with damage.

h_{max}	h_f/h_{max}	h_c	E_i	Rel. Error
Orig.			14.37	
0.6	0.375	0.528	6.98	-51.40%

Table 4.7: Extracted transverse indentation modulus and relative error for ideal plasticity

The extracted modulus is also heavily underestimated in transverse direction. The ratio h_f/h_{max} is considerably smaller than 0.7 in transverse direction. The ratio is much smaller than for the results of this study for materials featuring anisotropic elasto-plasticity.

The extracted indentation moduli underestimated the stiffness of the material by approximately 50% for the elastic ideal plastic material AEPDI featuring damage. There was no significant difference in relative error of the extracted indentation modulus between the axial (3) and the transverse (1) direction.

4.3.2 Exponential hardening

Two simulations of conical indentations in axial (3) and transverse (1) direction were performed for the anisotropic elasto-plastic material with damage accumulation AEPDE. Fig. 4.14 shows the reaction force vs. indentation depth of the axial tests (in direction 3) until an indentation depth of 0.6μm.
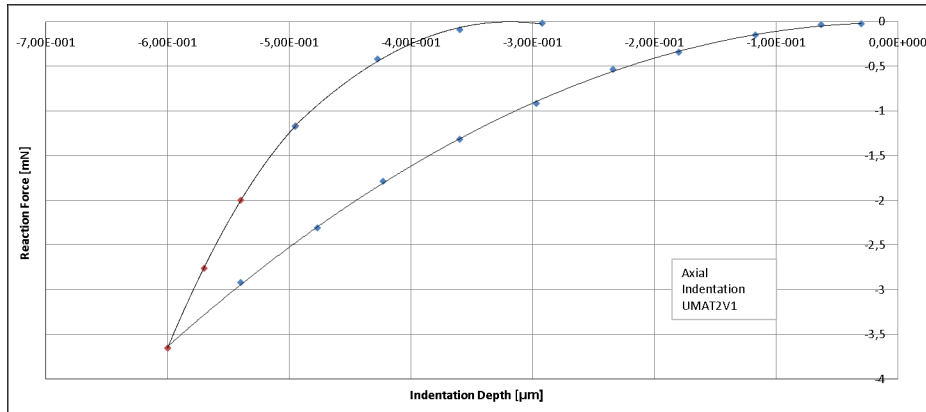
Figure 4.16: Reaction Force [mN] vs. Displacement [μm] for axial indentation of a conical indenter

This indentation curve looks qualitatively very similar to experimental indentation curves on bone. The indentation moduli were extracted as well using the method of Oliver and Pharr [OP92]. Using the original stiffness matrix from the Abaqus material definition and the theoretical framework of Swadener and Pharr [SP01], mathematically exact indentation moduli were calculated. The results of the simulation were then compared to the theoretical values. Table 4.3.2 shows the extracted indentation modulus in axial (3) direction and the relative error with respect to the theoretical modulus.

h_{max}	h_f/h_{max}	h_c	E_i	Rel. Error
Orig.			19.50	
0.6	0.488	0.505	9.83	-49.61%

Table 4.8: Extracted axial indentation modulus and relative error for exponential hardening

The extracted modulus is again heavily underestimated in axial direction. The ratio h_f/h_{max} is considerably smaller than 0.7 in axial direction. The ratio is also much smaller than for anisotropic elasto-plasticity. Fig. 4.17 shows a contour plot of the von Mises stress distribution in [GPa] for an indentation in axial direction on the deformed shape.
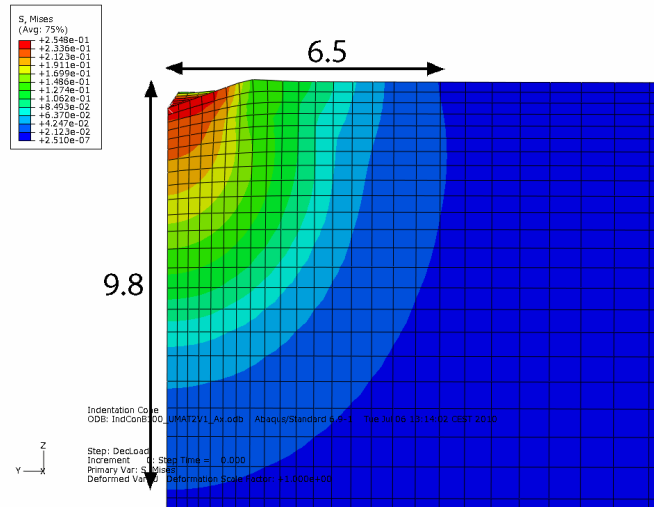
Figure 4.17: Contour plot of the von Mises stress distribution in $[GPa]$ for an indentation in axial direction at 0.6μm indentation depth (Max: 254.8MPa, Min: 21.2MPa)

The maximum von Mises stress is 254.8MPa. The stress at a depth of 9.8μm and at 6.5μm distance from the indentation center is still 21.2MPa. The stress field is axisymmetric and about 30% longer in axial direction than in radial direction. Fig. 4.18 shows a contour plot of the cumulated damage $D = 1 - f(\alpha)$ for an indentation in axial direction on the deformed shape. In the undamaged state, D is equal to 0, in the case of complete failure D equals 1.
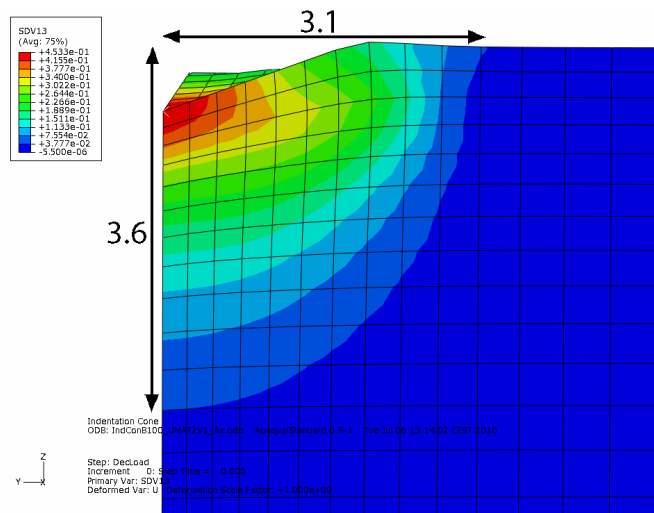
Figure 4.18: Contour plot of the cumulated damage D on the deformed shape for an indentation in axial direction at 0.6μm indentation depth (Max: 0.99, Min: 0.32)

The maximum damage is 0.99. This means almost complete failure of the material. The damage at a depth of 3.6μm and at 3.1μm distance from the indentation center is still 0.32. The damage field is axisymmetric and about 20% longer in axial direction than in radial direction. The shape

of the stress field changed significantly during unloading. Fig. 4.19 shows a contour plot of the residual von Mises stress distribution in $[GPa]$ for an indentation in axial direction on the deformed shape after unloading.
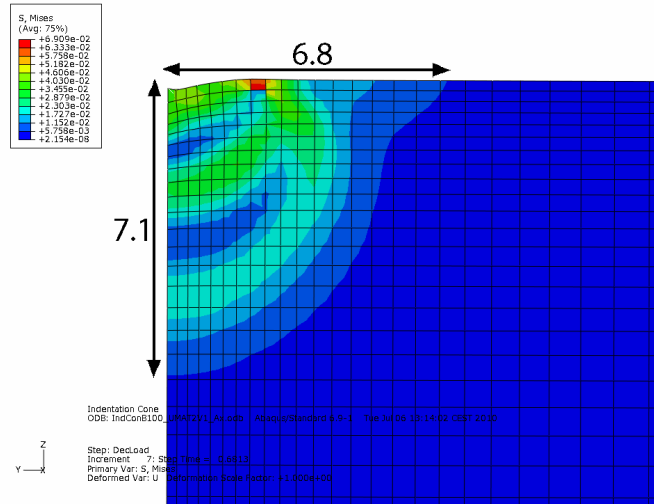
Figure 4.19: Contour plot of the residual von Mises stress distribution $[GPa]$ for an indentation in axial direction (Max: 69.1MPa, Min: 5.75MPa)

The maximum residual von Mises stress is 69.1MPa. The stress at a depth of 7.1μm and at 6.8μm distance from the indentation center is still 14.5MPa. The stress field is axisymmetric and about 5% longer in axial direction than in radial direction. The shape of the stress field changed significantly during unloading. Fig. 4.20 shows the reaction force vs. indentation depth of the transverse tests (in direction 1) to an indentation depth of 0.6μm.
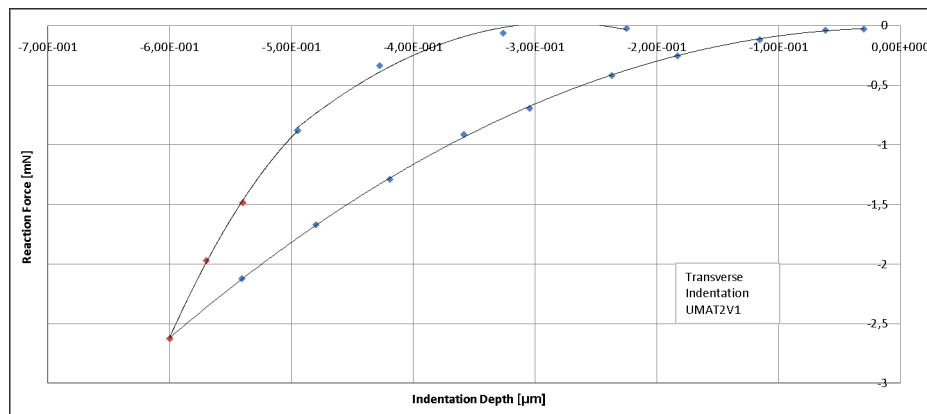
Figure 4.20: Reaction Force [mN] vs. Displacement [μm] for transverse indentation with exponential hardening

Table 4.3.2 shows the extracted indentation modulus in transverse direction and the relative error with respect to the theoretical modulus.

h_{max}	h_f/h_{max}	h_c	E_i	Rel. Error
Orig.			14.37	
0.6	0.375	0.517	7.86	-45.28%

Table 4.9: Extracted transverse indentation modulus and relative error for exponential hardening

The measured indentation modulus is also heavily underestimated in transverse direction. The ratio h_f/h_{max} is considerably smaller than 0.7 in transverse direction. The ratio is also much smaller than the simulations for anisotropic elasto-plasticity. Bolshakov et al. [BP98] found out that the method of Oliver and Pharr [OP92] works very accurately for isotropic elasto-plastic materials, if the ratio h_f/h_{max} is smaller than 0.7. This is not the case in the presence of damage in the material, as the results of this study show.

The extracted indentation moduli underestimated the stiffness of the material by approximately 45% to 49% for the elasto-plastic material AEPDE featuring exponential hardening and damage. There was only a small difference in relative error of the extracted indentation modulus between the axial (3) and the transverse (1) direction. Fig. 4.21 shows a contour plot of the von Mises stress distribution in $[GPa]$ for an indentation in transverse direction on the deformed shape in the 1-3 and 1-2 plane, respectively. There was no significant change in the depth of the remaining imprint when introducing exponential hardening.
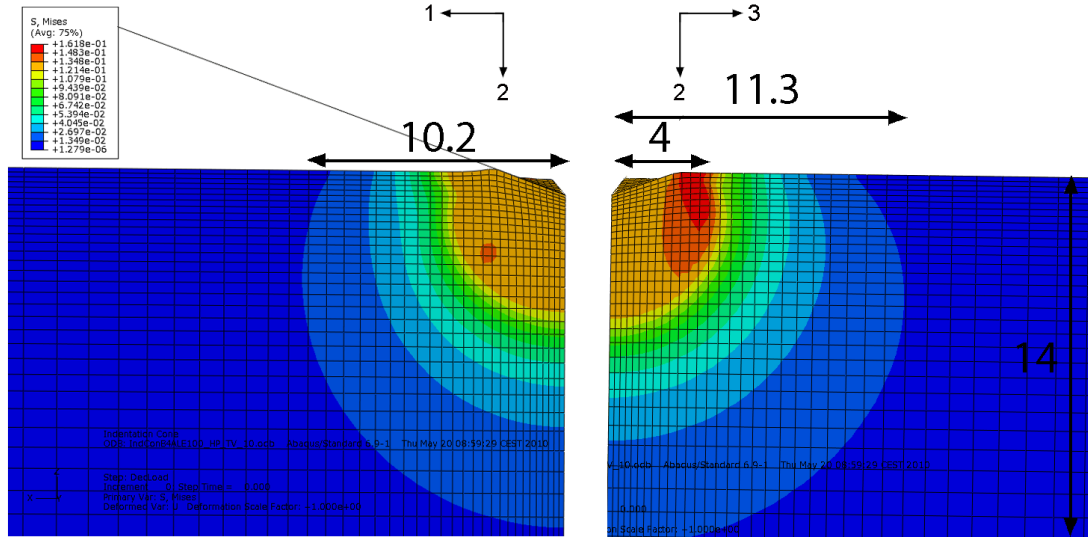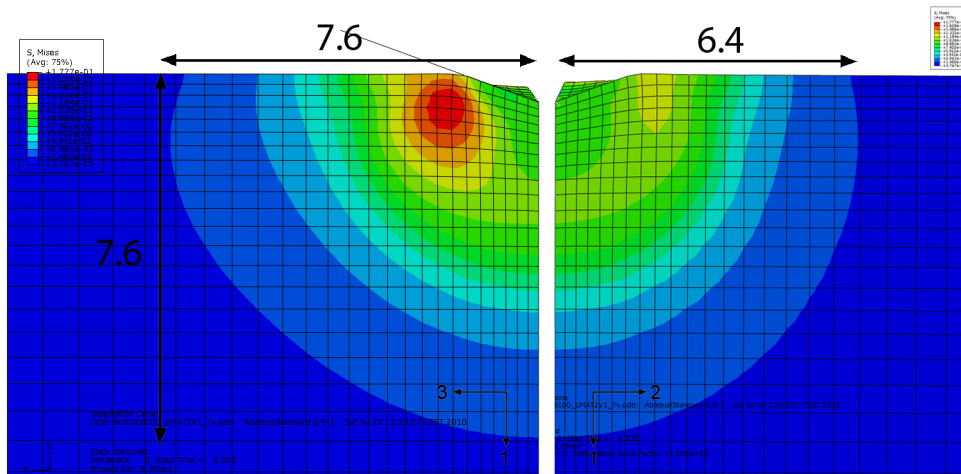

Figure 4.21: Contour plot of the von Mises stress distribution $[GPa]$ for an indentation in transverse direction on the deformed shape in the 1-3 (left) and 1-2 (right) plane at $0.6\mu m$ indentation depth (Max: 177.7MPa, Min: 14.8MPa)

The figure clearly shows that the shape of the contact area of the indentation is not axisymmetric. The contact depth is varying slightly over the perimeter. The highest stress is not centered under the indenter tip, but displaced by about $2\mu m$ in the material's 3 direction. This is most probably an effect of the anisotropy of the material. There is very little pile-up at the edges of the indentation in the 1-2 plane. There is slight sink-in in the 1-3 plane. There is a stress concentration visible in the 1-3 plane at a distance of about $2\mu m$ that stretches from the surface to a depth of about $3\mu m$. The

maximum von Mises stress under the indenter tip is 103.6MPa. The maximum von Mises stress at the stress concentration in the 1-3 plane is 177.7MPa. The von Mises stress at a depth of about 7.6μm and at 7.6μm distance from the indentation center in the 1-3 plane and 6.4μm distance from the indentation center in the 1-2 plane is still 14.8 MPa. The stress field is not axisymmetric. Fig. 4.22 shows a contour plot of the cumulated damage $D = 1 - f(\alpha)$ for an indentation in transverse direction on the deformed shape. In the undamaged state, D is equal to 0, in the case of complete failure D equals 1.
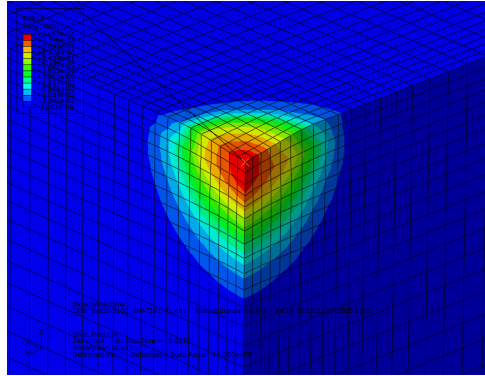
Figure 4.22: Contour plot of the cumulated damage D on the deformed shape for an indentation in transverse direction at 0.6μm indentation depth (Max: 0.975, Min: 0.265)

The maximum damage is 0.975. This means almost complete failure of the material. The damage at a depth of 3μm and at 2.5μm distance from the indentation center is still 0.265. The damage field is approximately axisymmetric and about 20% longer in axial direction than in radial direction. Fig. 4.23 shows a contour plot of the residual von Mises stress distribution in $[GPa]$ for an indentation in transverse direction on the deformed shape in the 1-3 and 1-2 plane.
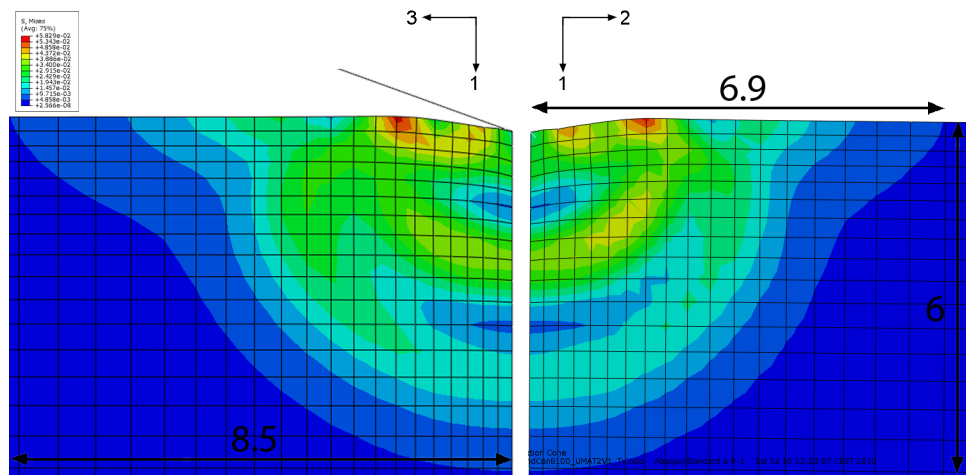
Figure 4.23: Contour plot of the residual von Mises stress distribution $[GPa]$ for an indentation in transverse direction on deformed shape in the 1-3 (left) and 1-2 (right) plane (Max: 58.3MPa, Min: 4.86MPa)

The maximum residual von Mises stress under the indenter tip is 38.9MPa. The maximum von Mises stress at the stress concentrations near the edges of the imprint is 58.3MPa. The von Mises stress at a depth of about 6μm and at 8.5μm distance from the indentation center in the 1-3 plane and 6.9μm distance from the indentation center in the 1-2 plane is still 4.86MPa. The stress field is not axisymmetric.

The extracted indentation moduli underestimated the stiffness of the material by approximately 45% to 51% depending on the type of hardening implemented in the material model. The error was slightly smaller for exponential hardening than for ideal plasticity. There was only small difference in relative error of the extracted indentation modulus between the axial (3) and the transverse (1) direction for exponential hardening and no significant difference for ideal plasticity. The damage ranged from 25% in transverse and 32% in axial direction at the vicinity of the indentation to 97% in transverse and 99% in axial direction at the indenter tip. While there was some minimal circular pile-up visible at the vicinity of the indentation in axial direction, there was almost no pile-up in transverse direction for exponential hardening. Also, the contact depth varied over the perimeter of the indentation in transverse direction. The slope of the unloading curve and the depth of the remaining imprint was considerably smaller for the damage model than for the purely elasto-plastic materials.

Chapter 5

Discussion

Detailed and extensive verification showed that the developed finite element mesh is able to simulate indentations in a wide range of different material models with sufficient accuracy. The mesh was tested for isotropic linear elasticity, anisotropic linear elasticity and isotropic ideal Mises plasticity. An anisotropic elasto-plastic material damage with damage was implemented in Fortran. Subsequently, single element tests were performed in order to verify the accuracy and convergence of the material models AEPDI and AEPDE. Based on this knowledge, multiple simulations were performed featuring different material models often used to model bone properties. First, isotropic elasto-plasticity with a Mises yield surface was simulated, then anisotropic elasto-plasticity based on a Hill yield surface. The final simulations were done featuring an elastic ideal plastic constitutive model with incorporated damage accumulation. Finally, exponential hardening was introduced into this model as well. The verification of the mesh showed some interesting results, especially for isotropic linear elasticity and anisotropic linear elasticity. Therefore the results of the verification will be discussed shortly as well.

5.1   Isotropic linear elasticity

The verification of the mesh showed that the model can simulate indentations on isotropic elastic halfspaces with great accuracy. A range of Poisson ratios from 0.01 to 0.49 was tested. The accuracy of the model with respect to the analytical solution by Sneddon [Sne48] increased with increasing Poisson ratio. For a Poisson ratio of 0.01, a considerable overestimation of the reaction force as well as the indentation modulus was reported (about 12% for both reaction force and modulus at all indentation depths larger than 200nm). For a Poisson ratio of 0.49, there was only an average error of 3% for the reaction force and 2% for the indentation modulus at an indentation depth of more than 200nm. When comparing the force-displacement curve to the empirical formula by Poon [PRR08a], the relative error was constant for indentation depths larger than 200nm and smaller than 1% for every tested Poisson ratio. The formula by Poon takes into account the finite tip radius as well as a stiffening effect based on the Poisson ratio. This effect is also described by Hay et al [HBP99]. According to Hay et al., in the solution of Sneddon of the Bousinnesq problem, the surface points inside the circle of contact are displaced radially during the indentation. This may be seen in eq. (1.8) describing the shape of the indentation for the solution of Sneddon. The radial displacements are always negative, which means that they point toward the center of the conical tip. They only vanish for a Poisson ratio of 0.5 or a indenter angle of 90°. Therefore in most practical cases, the shape of the deformed surface inside the contact area is not exactly conical for the problem modeled by Sneddon [Sne48], but cusp-shaped. This leads to an inaccuracy of the solution when

comparing it to a simulation of an indentation of a rigid cone. A higher load is needed for the indentation of a truly rigid cone with repect to the solution by Sneddon because the curved contact surface has to be pushed outside from the cusp-shaped profile in order to conform with the conical indenter according to Hay et al [HBP99]. This effect vanishes for incompressible materials, which explains the higher accuracy of the simulations with respect to the analytical solution by Sneddon when using the material ILE C featuring a Poisson ratio of 0.49 compared to lower Poisson ratios. The relative error of the reaction force and the indentation modulus was constant for indentation depths larger than 0.2 μm. This result was expected, as for linear elastic solids the indentation modulus should be insensitive to indentation depth according to Sneddon [Sne48].

5.2   Anisotropic linear elasticity

The verification of the mesh showed that the model can simulate indentations on anisotropic elastic half-spaces with reasonable accuracy. There was a certain overestimation of reaction force and indentation modulus of the model with respect to the analytical solution by Swadener and Pharr [SP01] in both axial and transverse direction. In axial direction, a considerable overestimation of the reaction force as well as the indentation modulus was reported (about 10% for both reaction force and modulus at indentation depths greater than 200nm). In transverse direction, the reported relative error was much smaller. There was only an average error of 5% for the reaction force and 2% for the indentation modulus at all indentation depths larger than 200nm. The large error with respect to the analytical solution might suggest that there is a similar effect based on radial displacements of the surface points inside the contact area as reported by Hay et al for isotropic elastic materials [HBP99]. No mention of this problem was found in the literature for anisotropic materials, though. The relative error of the reaction force and the indentation modulus was nearly constant for indentation depths larger than 200nm. This result was expected, as for linear elastic solids the indentation modulus should be insensitive to indentation depth according to Sneddon [Sne48].

5.3   Isotropic elasto-plasticity

First, cortical bone was modeled as an isotropic elastic ideal plastic material. For the conical indenter, simulations of indentations to depths of 600nm and 1μm were performed in order to show the influence of indentation depth on the extracted elastic properties. The indentation modulus was extracted at the beginning of the unloading phase using the method of Oliver and Pharr [OP92]. The same procedure was performed for an indentation using a Berkovich tip.

The reported relative error in the extracted elastic properties increased significantly with increasing indentation depth. This result was not expected, as theoretically the indentation modulus should be insensible to the indentation depth, as it is extracted during the purely elastic unloading phase. Recent numerical studies by Poon [PRR08b] showed that the unloading phase is indeed purely elastic for isotropic Mises plasticity. When reloading the specimen, the reloading path followed exactly the unloading path until the preceding maximum force was reached. Poon also showed in his study that the measurement error of the elastic modulus during a nanoindentation experiment is a function of the Poisson ratio ν of the material as well as the ratio of elastic modulus and yield strength $\frac{E}{\sigma_y}$. According to Poon, the Poisson ratio is an important factor for the amount of residual stresses at the indentation site. When ν approaches 0.5, the residual stresses are significantly smaller at the indentation site [PRR08b]. Poon interprets this as a decrease of residual elastic stresses in the plastic imprint with increasing Poisson ratio. This might partly explain the overestimation of the elastic modulus for IEP B with a Poisson ratio of 0.3. It should be noted that

an overestimation of the indentation modulus of about 10% was reported for a linearly elastic solid featuring the same elastic properties as IEP B. Therefore the overestimation is most probably only partly due to the plasticity in the material model. Bolshakov et al [BP98] and Hay et al [HBP99] give a more detailed analysis of the problem than Poon. According to Hay and Bolshakov, there is also a systematic error due to radial displacements of the surface points inside the contact area in Sneddon's solution that are not accounted for in the data analysis. It vanishes when ν approaches 0.5. This phenomenon is described in more detail in section 5.1. The direct use of the solution of Sneddon [Sne48] without correcting for this error leads to an overestimation of the elastic properties. However, the reported relative error of the extracted moduli were significantly higher for the Material IEP B than for IEP A, even though the Poisson ratio is 0.3 in both materials. For an indentation depth of 0.6μm, 14.96% were reported for IEP A and 24.93% for IEP B. This is a significant increase in measurement error. This may be explained by the difference in the ratio E/σ_y. This ratio was 50 for IEP A and 114.28 for IEP B. This coincides very well with data by Poon [PRR08b], who reported a measurement error of 13.3% for a ratio $E/\sigma_y = 50$ and 22.5% for $E/\sigma_y = 100$ for materials with a Poisson ratio of 0.3. According to Poon, as E/σ_y is a measure of the influence of plasticity. An increase of the ratio E/σ_y leads to an increase of material pile-up around the indenter. Therefore, the contact area is underestimated when using the Oliver and Pharr method and the elastic modulus is significantly overestimated. Bolshakov et al reported similar results [BP98] and gave some more insight into the problem. For elastic ideal plastic materials with a ratio of of the depth of the residual imprint to the maximum indentation depth h_f/h_{max} larger than 0.7, the influence of material pile-up was significant in the measurement of the elastic modulus. An underestimation of the contact area of up to 60% was reported for ideal plasticity leading to significant overestimation of the elastic modulus. In this study, the ratio h_f/h_{max} was larger than 0.7 for both isotropic elastic ideal plastic materials IEP A and IEP B. For this case, Bolshakov et al reported considerable overestimation of the elastic modulus due to the increased contact area due to material pile-up. The results of this study also showed that the analytical estimation of h_c severly underestimated the contact area. Poon [PRR08b] was also able to show that the measurement error of the elastic modulus is considerably smaller and a function of the Poisson ratio for isotropic elasto-plastic materials if the contact area is exactly known during the measurement, which further proves the point that material pile-up is a decisive factor in the estimation of the elastic modulus of elastic ideal plastic materials. This suggests that the remaining error is due to residual stresses in the plastic imprint of the indenter reported by Poon [PRR08b] and the radial displacements reported by Hay et al [HBP99]. When considering bone as an elasto-plastic material, the influence of damage accumulation due to microcracking is not taken into account. This effect might lead to a local decrease in stiffness which would reduce the overestimation of the extracted modulus.

When comparing the force-displacement curves for the conical indentation and the Berkovich indentation, no significant difference occurred. The measured elastic moduli did not differ significantly. The depth of the residual imprint was very similar. The contact depth was almost equal for both indenters. The contour plots of the stress and plastic strain distributions look qualitatively similar at some distance of the indenter tip. However, the distributions are not exactly the same. This can be explained with the principle of St. Venant: The structural response is equivalent for the conical indenter and the Berkovich indenter, as the projected area and therefore the integral over the surface stress distribution is equivalent. However, the stress distribution in close vicinity of the indentation is very different. The contour plots showed that the far-field stresses remained axisymmetric even for the non-axisymmetric Berkovich indenter. The shape of the indentation curve, the measured modulus and the depth of the remaining plastic imprint were very similar for both indenters. The conical model therefore yields very accurate results in the far stress field and the structural response when compared to the Berkovich indenter, at least for isotropic materials. The local fields however may differ significantly for the two indenters. Because of the additional computational cost and numerical instabilities of the Berkovich model, it was therefore not used

in further simulations. The problems encountered most probably occurred due to numerical instabilities at the sharp edges of the Berkovich indenter, as Abaqus provided corresponding warning messages throughout the simulations.

The data suggests that the method by Oliver and Pharr leads to a considerable overestimation of the elastic properties when analyzing indentation experiments of homogeneous isotropic elastoplastic materials mainly due to material pile-up that is not accounted for in the data analysis and an inaccuracy of Sneddons solution of the Boussinesq problem. The study showed that the conical indenter is an appropriate substitute for the Berkovich indenter for simulations of nanoindentations. Compact bone is not a homogeneous material due to its osteonal structure and different levels of mineralization inside the tissue. However, the assumption of homogeneity seems to be reasonable considering that the size of the bone structural unit (BSU) is considered to be approximately 60μm, which is considerably larger than the indentation depth. The assumption of isotropy is not very reasonable for bone due to its osteonal and lamellar structure which leads to an anisotropy with distinct material directions.

In nanoindentation experiments on bone tissue, no considerable pile-up of material at the edges has been reported according to Mullins et al. [MBM09]. This is contrary to the results of this study when indenting a material model using ideal Mises plasticity with a conical indenter. There was considerable pile-up around the edges of the indentation. It should also be noted that the Material IEP B used in this simulation features perfect plasticity, which plays a decisive role for the amount of pile-up around the indentation as reported by Bolshakov et al [BP98]. According to Bolshakov, the introduction of a hardening function will reduce the pile-up around the indentation and therefore the overestimation of the elastic properties. As there is no significant pile-up reported for indentations in bone, according to Mullins et al. [MBM09] we can conclude that isotropic Mises plasticity with perfect plasticity is not an appropriate material model for the mechanical behaviour of bone on the lamellar level, as it cannot model the local deformation around the conical indenter accurately. It should be noted that the pile-up around the Berkovich indenter has a considerably different shape than around the conical indenter. There is some pile-up in the middle of each side of the indenter. The pile-up decreases from the middle of the sides towards the indenter edges. Right at the edges, slight sink-in could be seen. This shows that the deformations around the conical indenter should be interpreted very carefully, as they are not equivalent to the deformations around the Berkovich indenter according to the principle of St. Vernant. Further examination of indentations of isotropic elasto-plastic materials featuring different hardening functions with a Berkovich indenter would be very interesting.

5.4 Anisotropic elasto-plasticity

Then, cortical bone was modeled as a transversely isotropic elastic ideal plastic material. With the conical indenter, simulations of indentations to depths of 600nm and 1μm were performed in order to show the influence of indentation depth on the extracted elastic properties. The indentation modulus was extracted at the beginning of the unloading phase using the method of Swadener and Pharr [SP01].

The relative error of the extracted indentation moduli is in the range of 19.5 to 27%. There is a significant increase in the overestimation of the indentation modulus with increasing indentation depth in axial direction. There is no remarkable trend in the transverse direction. The relative error was considerably larger in transverse direction than in axial direction. The relative error in the measurement of the indentation moduli was smaller for the material AEP in axial direction than in the isotropic case, in transverse direction it was about the same. The ratio of the depth of the residual imprint to the maximum indentation depth h_f/h_{max} is larger than 0.7 for both indentation depths in axial and transverse direction. Bolshakov et al reported a severe overestimation of the

indentation modulus [BP98] for isotropic elastic ideal plastic materials with a ratio of of the depth of the residual imprint to the maximum indentation depth h_f/h_{max} larger than 0.7. In this study, the ratio h_f/h_{max} was larger than 0.7 for both indentation directions. For this case, Bolshakov et al reported considerable overestimation of the indentation modulus due to the increased contact area due to material pile-up when using the standard method of Oliver and Pharr [OP92]. The data of this study seems to suggests that this problem exists in the anisotropic case as well. The analytical estimation of h_c lead to a severe underestimation of the actual contact area. Poon also reported that the amount of pile-up is a function of the ratio E/σ_y for isotropic materials. The ratio $E_0/\sigma_{y,0}$ was 88.5 for AEP, the measurement error at 0.6μm was 19.5% in axial direction. This coincides very well with data by Poon [PRR08b], who reported a measurement error of 22.5% for $E/\sigma_y = 100$ at an indentation depth of 0.6μm for isotropic materials. This suggests that there is a similar phenomenon in the anisotropic case. The contact shape of the indenter is approximately an ellipse in the indentation of a conical indenter into an anisotropic half space as predicted in theory by Swadener and Pharr [SP01]. The contact depth varies around the perimeter. In the case of the axial indentation on an transversely isotropic half-space the contact shape is circular and the contact depth is constant. In transverse direction the pile-up at the edges of the indentation is considerably larger in the directions with smaller elastic modulus. There is an off-center stress concentration in the 2-3 plane visible at the contact edge in the contour plots. For the indentation of a conical indenter in transverse direction, an axisymmetric deformation is forced on an anisotropic material with a stiff distinct axial direction. Therefore the stresses in the 2-3 plane are higher than in the isotropic transverse plane. Fig. 5.4 explains this phenomenon graphically.
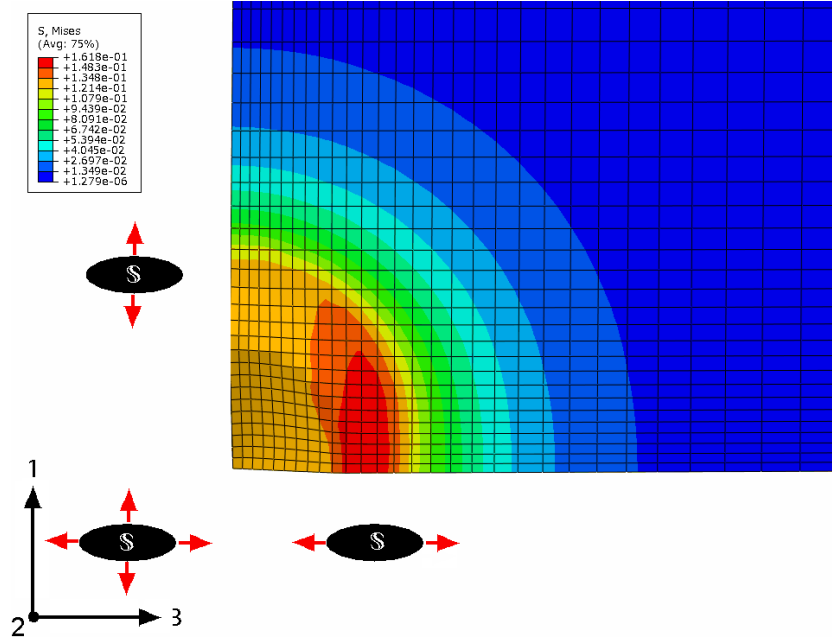
Figure 5.1: Explanation of the off-center stress concentration at the edge of the indentation for a transverse indentation in an anisotropic material

Under the indenter there is high pressure. Plastic flow occurs mainly in the indentation (2) direction, which has a lower yield stress than the 3 direction. There is an off-center stress concentration with a maximum Mises stress at the vicinity of the indentation. At this position, there is only low pressure. Plastic flow takes place mainly in the 3 direction with a high stiffness and a higher yield

strength. Therefore the Mises stress is higher at this position than in the surrounding area where plastic flow in 1 and 2 directions with lower yield strengths dominate. There is some pile-up visible around the indenter. The amount of pile-up is considerably smaller than in the isotropic case. This correlates very well with findings of Bolshakov er al [BP98], who predict an decrease of pile-up and relative error of the measured indentation modulus with decreasing h_f/h_{max} for isotropic materials. The results of this study suggest that there is a similar trend between the measurement error of the indentation modulus and the ratio h_f/h_{max} for anisotropic elastic ideal plastic materials as well.

The data suggests that the method by Oliver and Pharr [OP92] leads to a considerable overestimation of the elastic properties when analyzing indentation experiments of homogeneous transversely isotropic materials featuring ideal Hill plasticity. The assumption of transverse isotropy seems reasonable for compact bone due to its osteonal structure leading to anisotropy with a distinct axial direction and isotropy in the transverse plane. Compact bone is not a homogeneous material due to its osteonal structure and different levels of mineralization inside the tissue. However, this assumption seems to be reasonable considering that the size of the bone structural unit (BSU) is considered to be approximately 60μm, which is considerably larger than the maximum indentation depth in the numerical experiments. It should be noted that there was an overestimation of the indentation modulus of about 10% in axial direction and about 2% in transverse direction for a linear elastic solid featuring the same elastic properties as AEP. Therefore the overestimation of the indentation modulus might only partly be due to the plastic pile-up. There is some indication in the data that there might also be a systematic error due to radial displacements in Sneddon's solution that are not accounted for in the anisotropic case similar to the results reported by Bolshakov et al [BP98] and Hay et al [HBP99] for isotropic materials. No explicit mention of this problem in anisotropic materials was found in the literature, though. When considering bone as an elasto-plastic material, the influence of damage accumulation due to micro-cracking is not taken into account. This effect might lead to a local decrease in stiffness which would reduce the overestimation of the extracted modulus.

When indenting bone tissue, no considerable pile-up of material at the edges has been reported. The pile-up found when using the anisotropic Hill plasticity model was not constant around the perimeter of the indentation. The pile-up was smaller in directions with a higher elastic modulus than in the transverse direction. The material model used in this study featured ideal plasticity. According to Bolshakov et al [BP98], for isotropic elastic ideal plastic materials, the introduction of a hardening function will reduce the pile-up around the indentation and therefore the overestimation of the elastic properties. The overall amount of pile-up seemed to be smaller than in the isotropic case. The Hill plasticity model therefore seems to be able to give a significantly better explanation of the mechanical behaviour of bone on the lamellar and BSU level than isotropic Mises plasticity. It should be noted that the pile-up around the Berkovich indenter might have a considerably different shape than around the conical indenter. Therefore the deformations around the conical indenter should be interpreted very carefully, as they are not equivalent to the deformations around the Berkovich indenter according to the principle of St. Vernant. Further examination of indentations of anisotropic elasto-plastic materials featuring different hardening functions with a Berkovich indenter would be very interesting.

5.5 Anisotropic elasto-plasticity and damage

5.5.1 Perfect plasticity

Then, cortical bone was modeled as an orthotropic elastic ideal plastic material with damage. With the conical indenter, simulations of indentations to depths of 600nm were performed in axial (3) and transverse (1) direction. The indentation modulus was extracted at the beginning of the unloading

phase using the method of Oliver and Pharr [OP92] and compared to theoretical values computed in the mathematical framework developed by Swadener and Pharr [SP01]. Originally, it was planned to include simulations of indentations to 1μm as well in order to assess the influence of the indentation depth on the extracted indentation modulus. However, severe convergence problems of the model were encountered at indentation depths larger than 600nm. Therefore only results of simulations to 0.6μm were included in this study.

The extracted indentation moduli underestimated the stiffness of the material by approximately 51%. This was a very interesting finding, as the results of this study showed that both the purely elastic material models and the elasto-plastic models tended to overestimate the indentation modulus. There was no difference in relative error of the extracted indentation modulus between the axial (3) and the transverse (1) direction for ideal plasticity. The slope of the unloading curve and the depth of the remaining imprint was considerably smaller for the damage model than for the purely elasto-plastic materials. The measured indentation modulus was heavily underestimated in both axial and transverse direction. The ratio of the depth of the plastic imprint to the maximum h_f/h_{max} was considerably smaller than 0.7 for all simulations using the continuum damage model. The ratio was also much smaller than for the simulations featuring ideal anisotropic elasto-plasticity. Bolshakov et al. [BP98] reported that the method of Oliver and Pharr [OP92] yields very accurate results for isotropic elasto-plastic materials if the ratio h_f/h_{max} is smaller than 0.7. This is not the case in the presence of damage in the material, as the results of this study show. The assumption of intact unloading elasticity is not justified in the presence of damage under the indenter tip as the results of this study showed large damaged areas with a cumulated damage D of 0.25 to 0.97. A cumulated damage D 0f 0.97 corresponds to an almost complete loss of cohesion in the material. In reality, in the corresponding areas the high concentration of the microcracks would most probably lead to disintegration of the material. The stress and damage fields were qualitatively similar to the results reported by Zheng et al [ZMKO10] for an isotropic elasto-plastic continuum damage model.

The data suggests that the local damage accumulation under the indenter leads to a significant underestimation of the global undamaged mechanical properties. There was an underestimation of about 51% in both tested indentation directions. There is a somehow unrealistic deformation pattern in the center of the indentation when compared to actual indentations. This is the area of the highest damage with almost complete failure of the material. The influence of this effect seems to be negligible, as the affected area is very small compared to the indentation site. Also, the extremely high level of damage present in this area (about 97%) leading to almost complete failure suggests that continuum mechanics might not yield accurate results in the affected elements anymore. The problem might diminish with finer discretization of the material, as the mesh is too coarse to model the exact deformations and stresses right under the indenter tip.

5.5.2   Exponential hardening

Last, cortical bone was modeled as an orthotropic elastic plastic material with exponential hardening and damage. This type of plasticity is able to describe the macroscopic mechanical behaviour of bone very well as shown in previous studies [Zys94]. With the conical indenter, simulations of indentations to depths of 600nm in axial (3) and transverse (1) direction were performed. The indentation modulus was extracted at the beginning of the unloading phase using the method of Oliver and Pharr [OP92] and compared to theoretical values computed in the mathematical framework developed by Swadener and Pharr [SP01]. Originally, it was planned to include simulations of indentations to 1μm as well in order to assess the influence of the indentation depth on the extracted indentation modulus. However, severe convergence problems of the model were encountered at indentation depths larger than 600nm. Therefore only results of simulations to 0.6μm were included in this study.

The extracted indentation moduli underestimated the stiffness of the material by approximately

45% to 51% with respect to the theoretical values depending on the type of hardening implemented in the material model. This was a most interesting result, as earlier results of this study showed that both the purely elastic material models and the elasto-plastic models tended to overestimate the indentation modulus. The error was slightly smaller for exponential hardening than for ideal plasticity. There was only small difference in relative error of the extracted indentation modulus between the axial (3) and the transverse (1) direction for exponential hardening and no significant difference for ideal plasticity. The damage ranged from 25% in transverse and 32% in axial direction at the vicinity of the indentation to 97% in transverse and 99% in axial direction at the indenter tip. While there was some minimal circular pile-up visible at the vicinity of the indentation at maximum indentation depth in axial direction, there was almost no pile-up in transverse direction for exponential hardening. Also, the contact depth varied over the perimeter of the indentation in transverse direction. There is an off-center stress concentration in the 2-3 plane visible at the contact edge in the contour plots. For the indentation of a conical indenter in 1 direction, an axisymmetric deformation is forced on an anisotropic material with a three distinct material direction. Therefore the stresses in the 1-3 plane are higher than in the 1-2 transverse plane. Under the indenter there is high pressure. Plastic flow occurs mainly in the indentation (1) direction, which has the lowest elastic modulus of the three main material directions. There is an off-center stress concentration with a maximum Mises stress at the vicinity of the indentation in the 1-3 plane. At this position, there is only low pressure. Plastic flow takes place mainly in the 3 direction with a high stiffness and strength. Therefore the Mises stress is higher at this position than in the surrounding area where plastic flow in 1 and 2 directions with lower yield strengths dominate. There is also a slightly elevated stess state in the 1-2 plane. As the stiffness and strength is greater in 2 direction than in 1 direction, the same reasoning can be used to explain this phenomenon. The slope of the unloading curve and the depth of the remaining imprint was considerably smaller for the damage model than for the purely elasto-plastic materials. The measured indentation modulus was heavily underestimated in both axial and transverse direction. The analytical estimation of h_c seemed to be reasonable in all cases. The ratio h_f/h_{max} was considerably smaller than 0.7 for all simulations. The ratio was also much smaller than for the simulations featuring anisotropic elasto-plasticity. Bolshakov et al. [BP98] reported that the method of Oliver and Pharr [OP92] works accurately for isotropic elastic ideal plastic materials if the ratio h_f/h_{max} is smaller than 0.7. This is not the case in the presence of damage in the material, as the results of this study clearly show. The assumption of intact unloading elasticity is not justified as the results of this study showed large damaged areas with a cumulated damage D of 0.32 to 0.99 under the indenter tip. A cumulated damage D of 0.99 corresponds to an almost complete loss of cohesion in the material. In reality, in the corresponding areas the high concentration of the microcracks would most probably lead to a complete disintegration of the material. The shape of the stress and damage fields were qualitatively similar to the results reported by Zheng et al [ZMKO10] for an isotropic elasto-plastic continuum damage model.

The data obtained in the course of this study shows that the local damage accumulation under the indenter leads to a significant underestimation of the global undamaged mechanical properties. There was an underestimation of about 45 to 51% in depending on the indentation direction. The type of hardening implemented in the material model seems to be an important factor for the determination of the measured indentation modulus. The underestimation of the indentation modulus was slightly smaller in both indentation directions for exponential hardening than for perfect plasticity (about 2-6%), probably because less damage accumulates during the course of the experiment due to hardening of the material. Therefore the remaining stiffness in the material under the indenter tip is higher than for perfect plasticity. Only the deviatoric part of the stiffness matrix is affected by damage accumulation. There is a somehow unrealistic deformation pattern visible in the center of the indentation when compared to actual indentations. This is the area of the maximum damage with almost complete failure of the material. The influence of this effect

seems to be negligible, as the affected area is very small compared to the indentation site. Also, the high amount of damage present in this area (about 97 to 99%) leading to almost complete failure suggests that continuum mechanics might not yield accurate results in the affected elements anymore. The problem might diminish with finer discretization of the material, as the mesh is too coarse to model the exact deformations and stresses right at the indenter tip.

5.6 Conclusion

This study was conducted in order to be able to quantify the error made when analyzing nanoindentation experiments on bone tissue depending on different parameters including indenter geometry, indentation depth and constitutive mechanical behaviour of the indented half-space.

The results of this study indicate clearly that the indentation modulus is insensible to indentation depth for purely elastic materials. The analytical solution by Sneddon does not account for finite tip radii. However, the effect of the radius diminishes with growing indentation depth. Also, there is a stiffening effect based on the Poisson ratio for elastic materials reported by Poon [PRR08b]. Poon implemented an empirical formula that coincides with the data obtained during the course of this study very well. This effect is also described by Hay et al [HBP99]. According to Hay, there is also a systematic error due to radial displacements of the surface points inside the contact area in Sneddon's solution that are not accounted for in the data analysis. It vanishes only for a Poisson ratio of 0.5 or a indenter angle of 90°. Therefore in most practical cases, a higher load is needed for the indentation of a truly rigid cone with respect to the solution by Sneddon because the curved contact surface has to be pushed outside from the cusp-shaped profile in order to conform with the conical indenter [HBP99].

For materials featuring nonlinear effects like plasticity or even damage there is clear indication in the data that the indentation depth has indeed an effect on the measured indentation modulus. For elastic ideal plastic materials the initial unloading phase is purely elastic [PRR08b]. However, there is a serious overestimation of the indentation modulus due to material pile-up. Bolshakov et al reported similar results [BP98]. For elastic ideal plastic materials with a ratio of of the depth of the residual imprint to the maximum indentation depth h_f/h_{max} larger than 0.7, the influence of material pile-up was significant in the measurement of the elastic modulus. In this study, the ratio h_f/h_{max} was larger than 0.7 for both isotropic elastic ideal plastic materials IEP A and IEP B. For this case, Bolshakov et al reported considerable overestimation of the elastic modulus due to the increased contact area due to material pile-up. Poon [PRR08b] was also able to show that the measurement error of the elastic modulus is considerably smaller and a function of the Poisson ratio for isotropic elasto-plastic materials if the contact area is exactly known during the measurement. This suggests that the remaining error is due to residual stresses in the plastic imprint of the indenter reported by Poon [PRR08b] and the radial displacements of the surface points in the contact area reported by Hay et al [HBP99]. Mullins et al [MBM09] performed simulations of indentations using an axisymmetric model. The goal was to find a material model that could describe the shape parameters of the indentation curve as well as the indentation geometry such as pile-up and elastic recovery. According to Mullins, no considerable pile-up was reported for nanoindentations on bone [MBM09]. This seems to be a promising technique. However, it only works for experiments using conical or spheroconical tips, as the pile-up around the Berkovich indenter might have a considerably different shape than around the conical indenter in the anisotropic case. The shape of the pile-up differed significantly between the two indenters for isotropic elasto-plasticity. Therefore the deformations around the conical indenter should be interpreted very carefully, as they might not be equivalent to the deformations around the Berkovich indenter according to the principle of St. Vernant. In the course of this study, a first attempt was made to model the 3D geometry of the actual Berkovich indenter. It was shown that while the conical indenter is an excellent model

for the Berkovich indenter in the far stress field and the structural response, the local stress and strain state in close vicinity to the indenter differs significantly. This result is in accordance with the principle of St. Venant stating that the reaction to a statically equivalent load at a sufficient distance will be the same independent of the exact load distribution.

In the case of anisotropic elastic ideal plastic materials, the data suggests that the method by Oliver and Pharr [OP92] leads to a considerable overestimation of the elastic properties when analyzing indentation experiments. The reported error of the extracted indentation moduli was in the range of 19 to 27%. There is a significant increase in the overestimation of the indentation modulus with increasing indentation depth in axial direction. There is no remarkable trend in the transverse direction. The relative error was considerably larger in transverse direction than in axial direction. The relative error in the measurement of the indentation moduli was smaller for the material AEP in axial direction than in the isotropic case, in transverse direction it was about the same. The ratio of the depth of the residual imprint to the maximum indentation depth h_f/h_{max} is larger than 0.7 for both indentation depths in axial and transverse direction. Bolshakov et al reported a severe overestimation of the indentation modulus [BP98] for isotropic elastic ideal plastic materials with a ratio of of the depth of the residual imprint to the maximum indentation depth h_f/h_{max} larger than 0.7. In this study, the ratio h_f/h_{max} was larger than 0.7 for both indentation directions. For this case, Bolshakov et al reported considerable overestimation of the indentation modulus due to material pile-up when using the standard method of Oliver and Pharr [OP92]. The data of this study seems to suggests that this problem exists in the anisotropic case as well. The contact shape of the indenter is approximately an ellipse in the indentation of a conical indenter into an anisotropic half space as predicted in theory by Swadener and Pharr [SP01]. The contact depth varies around the perimeter. In the case of the axial indentation on an transversely isotropic half-space the contact shape is circular and the contact depth is constant. In transverse direction the pile-up at the edges of the indentation is considerably larger in the directions with smaller elastic modulus. There is an off-center stress concentration visible in the 2-3 plane because of the forced axisymmetric deformation of the anisotropic material. There is some pile-up visible around the indenter. The amount of pile-up is considerably smaller than in the isotropic case. This correlates very well with findings of Bolshakov er al [BP98], who predict an decrease of pile-up and relative error of the measured indentation modulus with decreasing h_f/h_{max} for isotropic materials. The data of this study also correlated well with results by Poon, who reported that the amount of pile-up is a function of the ratio E/σ_y for isotropic materials. This suggests that there is a similar phenomenon in the anisotropic case. The results of this study suggest that there might be a similar trend between the measurement error of the indentation modulus and the ratio h_f/h_{max} as well as the ratio $E_0/\sigma_{y,0}$ for anisotopic elastic ideal plastic materials.

When damage accumulation is considered in an elasto-plastic material, the shape of the indentation curve was qualitatively very similar to experimental results for nanoindentation experiments on bone tissue. However, the measured indentation modulus was considerably smaller than expected. There was an underestimation of about 45 to 51% in modulus depending on the indentation direction. The type of hardening implemented in the material model seems to be an important factor for the determination of the measured indentation modulus. The underestimation was slightly smaller in both indentation directions for exponential hardening than for perfect plasticity, as less damage accumulates due to hardening of the material. Therefore the remaining stiffness in the material under the indenter tip is higher than for perfect plasticity. The damage ranged from 25% in transverse and 32% in axial direction at the vicinity of the indentation to 97% in transverse and 99% in axial direction at the indenter tip. While there was some minimal circular pile-up visible at the vicinity of the indentation at maximum indentation depth in axial direction, there was almost no pile-up in transverse direction for exponential hardening. Also, the contact depth varied over the perimeter of the indentation in transverse direction. The slope of the unloading curve and the depth of the remaining imprint was considerably smaller for the damage model than for the purely elasto-plastic

materials. The measured indentation modulus was heavily underestimated in both axial and transverse direction. The ratio h_f/h_{max} was considerably smaller than 0.7 for all simulations. The ratio was also much smaller than for the simulations featuring anisotropic elasto-plasticity. Bolshakov et al. [BP98] reported that the method of Oliver and Pharr [OP92] works very accurately for isotropic elastic ideal plastic materials if the ratio h_f/h_{max} is smaller than 0.7. This is not the case in the presence of damage in the material, as the results of this study show. The assumption of intact unloading elasticity is not justified, as the results of this study showed large damaged areas with a cumulated damage D of 0.32 to 0.99. A cumulated damage D of 0.99 corresponds to an almost complete loss of cohesion in the material. In reality, in the corresponding areas the high concentration of the microcracks would most probably lead to disintegration of the material. This suggests that continuum mechanics might not yield accurate results in the affected areas of extremely high damage. The shape of the stress and damage fields were qualitatively similar to the results reported by Zheng et al [ZMKO10] for an isotropic elasto-plastic continuum damage model. The data obtained in the course of this study shows that the local damage accumulation under the indenter leads to a significant underestimation of the global undamaged mechanical properties. There is a somehow unrealistic deformation pattern visible in the center of the indentation when compared to actual indentations. This is the area of the maximum damage with almost complete failure of the material. The influence of this effect seems to be negligible, as the affected area is very small compared to the indentation site. Also, the high amount of damage present in this area (about 97 to 99%) leading to almost complete failure suggests that continuum mechanics might not yield accurate results in the affected elements anymore. The problem might diminish with finer discretization of the material, as the mesh is too coarse to model the exact deformations and stresses right at the indenter tip.

In the course of this study only simulations to an indentation depth of 0.6μm were performed using the continuum damage model. In order to verify that there is a sensibility of the measured modulus to the indentation depth in the damage model as well, more simulations would need to be performed. Unfortunately, there was not enough time to perform these simulations, as problems with element distortion and non-convergence of the model occurred at indentation depths deeper than 0.6μm. Also, no time- or rate-dependent effects were accounted for in the course of this study. Only rate-independent material models were used. As bone shows visco-elastic behavior such as creep and relaxation, the behavior of bone could not be modeled to a full degree. As a next step, the introduction of time-dependent effects into the different material models would give a better correlation to experimental data and more insight into the behavior of bone during nanoindentation experiments.

Appendix A

Implementation in Fortran

```fortran
      SUBROUTINE UMAT(STRESS,STATEV,DDSDDE,SSE,SPD,SCD,
     1 RPL,DDSDDT,DRPLDE,DRPLDT,STRAN,DSTRAN,
     2 TIME,DTIME,TEMP,DTEMP,PREDEF,DPRED,MATERL,NDI,NSHR,NTENS,
     3 NSTATV,PROPS,NPROPS,COORDS,DROT,PNEWDT,CELENT,
     4 DFGRD0,DFGRD1,NOEL,NPT,KSLAY,KSPT,KSTEP,KINC)
C
      INCLUDE 'ABA_PARAM.INC'
C
      CHARACTER*80 CMNAME
      DIMENSION STRESS(NTENS),STATEV(NSTATV),
     1 DDSDDE(NTENS,NTENS),DDSDDT(NTENS),DRPLDE(NTENS),
     2 STRAN(NTENS),DSTRAN(NTENS),TIME(2),PREDEF(1),DPRED(1),
     3 PROPS(NPROPS),COORDS(3),DROT(3,3),DFGRD0(3,3),DFGRD1(3,3)
      PARAMETER (ONE=1.0D0,TWO=2.0D0,THREE=3.0D0,SIX=6.0D0)
      DATA NEWTON,TOLER,TOLERH/30,1.D-08,1.D-08/
      DOUBLE PRECISION MM1,MM2,MM3,RHO,ALPHAF,GMAX,YSIG
      DOUBLE PRECISION EEEE(NTENS,NTENS),SSSS(NTENS,NTENS)
      DOUBLE PRECISION EEEC(NTENS,NTENS),EEED(NTENS,NTENS)
      DOUBLE PRECISION SSSC(NTENS,NTENS),SSSD(NTENS,NTENS)
      DOUBLE PRECISION ETOT0(NTENS),ETOT1(NTENS),EELAS0(NTENS)
      DOUBLE PRECISION EPLAS0(NTENS),ALPHAG
      DOUBLE PRECISION TEMP1(NTENS),TEMP2,TEMP3(NTENS,NTENS)
      DOUBLE PRECISION ALPHA0,FA0,GA0,STR(NTENS)
      DOUBLE PRECISION STRD(NTENS),DFA1,DGA1,DFA0,DGA0,GA1,FA1
      INTEGER ITER
      DOUBLE PRECISION YSTR,LAM,DLAM,FACTOR,SSD(NTENS)
      DOUBLE PRECISION DSYY0(NTENS,NTENS),DSYY0I(NTENS,NTENS)
      DOUBLE PRECISION TEMP4(NTENS,NTENS),TEMP5(NTENS,NTENS)
      DOUBLE PRECISION EPLAS1(NTENS),EELAS1(NTENS)
      DOUBLE PRECISION ALPHA1,SS1(NTENS)
      DOUBLE PRECISION TEMP6(NTENS),TEMP7,TANM(NTENS,NTENS)

C
C     _____
C
```

```
C
C     PARAMETERS FROM INPUT FILE
C
         RHO=PROPS(1)
        MM1=PROPS(2)
        MM2=PROPS(3)
        MM3=PROPS(4)
C     ------------------------------------------------------------------
C
C     TENSOR INITIALISATION
C
      DO 20 K1=1,NTENS
        DO 10 K2=1,NTENS
           DDSDDE(K1,K2)=0.0D0
           EEEE(K1,K2)=0.0D0
           EEEC(K1,K2)=0.0D0
           EEED(K1,K2)=0.0D0
           SSSS(K1,K2)=0.0D0
           SSSC(K1,K2)=0.0D0
           SSSD(K1,K2)=0.0D0
           TEMP3(K1,K2)=0.0D0
           TEMP4(K1,K2)=0.0D0
           TEMP5(K1,K2)=0.0D0
           DSYY0(K1,K2)=0.0D0
           DSYY0I(K1,K2)=0.0D0
           TANM(K1,K2)=0.0D0
 10     CONTINUE
 20     CONTINUE
C
C     VECTOR INITIALISATION
C
      DO K1=1,NTENS
 TEMP1(K1)=0.0D0
         TEMP6(K1)=0.0D0
 ETOT0(K1)=0.0D0
 ETOT1(K1)=0.0D0
 EELAS0(K1)=0.0D0
 EPLAS0(K1)=0.0D0
 STR(K1)=0.0D0
 STRD(K1)=0.0D0
 EPLAS1(K1)=0.0D0
 EELAS1(K1)=0.0D0
 SS1(K1)=0.0D0
      ENDDO
C
C     SCALAR INITIALISATION
C
      ALPHAF=0.0D0
      YSIG=0.0D0
      GMAX=0.0D0
```

```fortran
      ALPHAG=0.0D0
      FA0=1.0D0
      DFA0=0.0D0
      GA0=0.0D0
      DGA0=0.0D0
      TEMP2=0.0D0
      YSTR=0.0D0
      LAM=0.0D0
      DLAM=0.0D0
      FA1=1.0D0
      DFA1=0.0D0
      GA1=0.0D0
      DGA1=0.0D0
      ALPHA1=0.0D0
      ALPHA0=0.0D0
      TEMP7=0.0D0
      FACTOR=0.0D0
C     ----------------------------------------------------------------
C
C     MATERIAL PROPERTIES
C
      ALPHAF=0.098979291D0
      YSIG=0.022768399D0
      GMAX=0.010751744D0
      ALPHAG=0.026246905D0
C     ----------------------------------------------------------------
C
C     ORTHOTROPIC SYMMETRIC COMPLIANCE TENSOR EEEE
C
      EEEE(1,1)=0.0833333D0
      EEEE(2,2)=0.0746269D0
      EEEE(3,3)=0.05D0
      EEEE(4,4)=0.110375D0
      EEEE(5,5)=0.0891266D0
      EEEE(6,6)=0.0802568D0
      EEEE(2,1)=-0.0314129D0
      EEEE(3,1)=-0.018525D0
      EEEE(3,2)=-0.0175187D0
      EEEE(1,2)=EEEE(2,1)
      EEEE(1,3)=EEEE(3,1)
      EEEE(2,3)=EEEE(3,2)
C
C     CONSTANT PART OF DECOMPOSITION OF EEEE
C
      EEEC(1,1)=0.0055887D0
      EEEC(2,2)=0.00661628D0
      EEEC(3,3)=0.0109815D0
      EEEC(2,1)=0.00608082D0
      EEEC(3,1)=0.00783406D0
      EEEC(3,2)=0.0085239D0
```

```
      EEEC(1,2)=EEEC(2,1)
      EEEC(1,3)=EEEC(3,1)
      EEEC(2,3)=EEEC(3,2)
C
C     DAMAGEABLE PART OF DECOMPOSITION OF EEEE
C
      EEED(1,1)=0.0777446D0
      EEED(2,2)=0.0680106D0
      EEED(3,3)=0.0390185D0
      EEED(4,4)=0.110375D0
      EEED(5,5)=0.0891266D0
      EEED(6,6)=0.0802568D0
      EEED(2,1)=-0.0374938D0
      EEED(3,1)=-0.0263591D0
      EEED(3,2)=-0.0260426D0
      EEED(1,2)=EEED(2,1)
      EEED(1,3)=EEED(3,1)
      EEED(2,3)=EEED(3,2)
C     ----------------------------------------------------------------
C
C     ORTHOTROPIC SYMMETRIC STIFFNESS TENSOR SSSS
C
      SSSS(1,1)=18.0203D0
      SSSS(2,2)=20.1202D0
      SSSS(3,3)=27.5329D0
      SSSS(4,4)=9.06D0
      SSSS(5,5)=11.22D0
      SSSS(6,6)=12.46D0
      SSSS(2,1)=9.97294D0
      SSSS(3,1)=10.1708D0
      SSSS(3,2)=10.7446D0
      SSSS(1,2)=SSSS(2,1)
      SSSS(1,3)=SSSS(3,1)
      SSSS(2,3)=SSSS(3,2)
C
C     CONSTANT PART OF DECOMPOSITION OF SSSS
C
      SSSC(1,1)=10.3954D0
      SSSC(2,2)=12.3067D0
      SSSC(3,3)=20.4264D0
      SSSC(2,1)=11.3107D0
      SSSC(3,1)=14.5719D0
      SSSC(3,2)=15.855D0
      SSSC(1,2)=SSSC(2,1)
      SSSC(1,3)=SSSC(3,1)
      SSSC(2,3)=SSSC(3,2)
C
C     DAMAGEABLE PART OF DECOMPOSITION OF SSSS
C
      SSSD(1,1)=7.62495D0
```

```
         SSSD(2,2)=7.81349D0
         SSSD(3,3)=7.10646D0
         SSSD(4,4)=9.06D0
         SSSD(5,5)=11.22D0
         SSSD(6,6)=12.46D0
         SSSD(2,1)=-1.33781D0
         SSSD(3,1)=-4.40111D0
         SSSD(3,2)=-5.11049D0
         SSSD(1,2)=SSSD(2,1)
         SSSD(1,3)=SSSD(3,1)
         SSSD(2,3)=SSSD(3,2)
C
C      ----------------------------------------------------------------
C
C      RECOVER TOTAL, ELASTIC AND PLASTIC STRAINS, DAMAGE VARIABLE ALPHA0
C
       DO 30 K1=1,NTENS
          EELAS0(K1)=STATEV(K1)
          EPLAS0(K1)=STATEV(K1+NTENS)
          ETOT0(K1)=STRAN(K1)
          ETOT1(K1)=STRAN(K1)+DSTRAN(K1)
 30    CONTINUE
C
       ALPHA0=STATEV(13)
C      ----------------------------------------------------------------
C
C      CONVERT INITIAL STRAIN MEASURES TO VOITH-MANDL NOTATION
C
       DO K1=4,6
          EELAS0(K1)=EELAS0(K1)/SQRT(2.0D0)
          EPLAS0(K1)=EPLAS0(K1)/SQRT(2.0D0)
          ETOT0(K1)=ETOT0(K1)/SQRT(2.0D0)
          ETOT1(K1)=ETOT1(K1)/SQRT(2.0D0)
       ENDDO
C      ----------------------------------------------------------------
C
C      INITIAL STATE OF HARDENING AND DAMAGE
C
       FA0=EXP(-ALPHA0/ALPHAF)
       DFA0=-1.0D0/ALPHAF*EXP(-ALPHA0/ALPHAF)
       GA0=GMAX*(1-EXP(-ALPHA0/ALPHAG))+YSIG
       DGA0=GMAX/ALPHAG*EXP(-ALPHA0/ALPHAG)
C      ----------------------------------------------------------------
C
C      TRIAL ELASTIC STRESS
C
          DO 50 K1=1,NTENS
            FACTOR=0.0D0
            DO 40 K2=1,NTENS
               FACTOR=FACTOR+SSSC(K1,K2)*(ETOT1(K2)-EPLAS0(K2))+FA0
```

```
      1                   *SSSD(K1,K2)*(ETOT1(K2)-EPLAS0(K2))
 40          CONTINUE
             STR(K1)=FACTOR
 50        CONTINUE
C
C     TRIAL ELASTIC STRESS PRIME
C
           DO 51 K1=1,NTENS
             FACTOR=0.0D0
             DO 41 K2=1,NTENS
                 FACTOR=FACTOR+FA0*SSSD(K1,K2)*(ETOT1(K2)-EPLAS0(K2))
 41          CONTINUE
             STRD(K1)=FACTOR
 51        CONTINUE
C     ------------------------------------------------------------------
C
C     YIELD CRITERION FOR TRIAL ELASTIC STRESS
C
      TEMP2=0.0D0
C     SUBROUTINE FOR TEMP1(NTENS)=E'S
      CALL MATVEC(EEED,STR,TEMP1,NTENS)
C     SUBROUTINE FOR TEMP2=S:E'SC
      CALL SCALPROD(STR,TEMP1,TEMP2,NTENS)
C
      YSTR=SQRT(ABS(TEMP2))-GA0
C     ------------------------------------------------------------------
C
C
C     %ELASTIC CASE%
C     ------------------------------------------------------------------
C
      IF (YSTR.LE.0.0D0) THEN
C
C        UPDATE STATE VARIABLES
C
         DO K1=1,NTENS
           EPLAS1(K1)=EPLAS0(K1)
           EELAS1(K1)=ETOT1(K1)-EPLAS0(K1)
         ENDDO
C
         ALPHA1=ALPHA0
C
C        ELASTIC STRESS UPDATE
C
         DO K1=1,NTENS
           SS1(K1)=STR(K1)
         ENDDO
C
C        ELASTIC JACOBIAN
C
         DO 70 K1=1,NTENS
```

```
            DO 60 K2=1,NTENS
                TANM(K1,K2)=SSSC(K1,K2)+FA0*SSSD(K1,K2)
 60        CONTINUE
 70      CONTINUE
C
      ENDIF
C    ----------------------------------------------------------------
C
C    %INELASTIC CASE%
C    ----------------------------------------------------------------
C
C    TEMP1(NTENS)=E'STR'
C    TEMP2=STR':E'STR'
C    TEMP3(NTENS,NTENS)=E'S ox E'S
C    TEMP5=DSYY0I*(E'S ox E'S)*DSYY0I
C    TEMP7=E'S:DSYY0I*E'S
C
      IF (YSTR.GT.0.0D0) THEN
C
            ITER=0
            LAM=0.0D0
            DLAM=0.001D0
C
C         SOUBROUTINE FOR TEMP1(NTENS)=E'STR'
            CALL MATVEC(EEED,STRD,TEMP1,NTENS)
C
C         SUBROUTINE FOR TEMP2=STR':E'STR'
            TEMP2=0.0D0
            CALL SCALPROD(STRD,TEMP1,TEMP2,NTENS)
C
            ALPHA1=ALPHA0
C
            FA1=EXP(-ALPHA1/ALPHAF)
            DFA1=-1.0D0/ALPHAF*EXP(-ALPHA1/ALPHAF)
            GA1=GMAX*(1-EXP(-ALPHA1/ALPHAG))+YSIG
            DGA1=GMAX/ALPHAG*EXP(-ALPHA1/ALPHAG)
C
C         IMPLICIT ITERATIVE BACKPROJECTION ON YIELD SURFACE
C
            DO WHILE (ABS(DLAM).GT.TOLER.AND.ITER.LE.NEWTON)
C
              ITER=ITER+1
C
C             h(lambda)
C
              H=(SQRT(ABS(TEMP2))-LAM*FA0)*FA1-FA0*GA1
C
C             dh/dlambda
C
                DHDL=(SQRT(ABS(TEMP2))-LAM*FA0)*DFA1-FA0*FA1-FA0*DGA1
```

```
C
C             RECURRENCE FORMULA LAMBDA(I+1)-LAMBDA(I)
C
              DLAM=-H/DHDL
C     ------------------------------------------------------------------
C
C             UPDATE LAMBDA
C
              LAM=LAM+DLAM
C     ------------------------------------------------------------------
C
              IF (ITER.GE.NEWTON) THEN
                WRITE(*,11)
 11             FORMAT(//,30X,'WARNING: ALGORITHM DID NOT CONVERGE')
              ENDIF
C
              IF (LAM.LT.0.OR.LAM.GT.1) THEN
                WRITE(*,*)"    Damage exceeded 0..1"
                WRITE(*,*)"    LAM:        ",LAM
                WRITE(*,*)"    Old Value: ",ALPHA0
                WRITE(*,*)"    Element:   ",NOEL
                WRITE(*,*)"    Int. Point:",NPT
                WRITE(*,*)"    Increment: ",KINC
                WRITE(*,*)"    Iteration: ",ITER
              ENDIF
C     ------------------------------------------------------------------
C
C             UPDATE DAMAGE VARIABLE
C
              ALPHA1=ALPHA0+LAM
C     ------------------------------------------------------------------
C
C             UPDATE DAMAGE AND HARDENING FUNCTION
C
              FA1=EXP(-ALPHA1/ALPHAF)
              DFA1=-1.0D0/ALPHAF*EXP(-ALPHA1/ALPHAF)
              GA1=GMAX*(1-EXP(-ALPHA1/ALPHAG))+YSIG
              DGA1=GMAX/ALPHAG*EXP(-ALPHA1/ALPHAG)
C
              ENDDO
C     ------------------------------------------------------------------
C
C             UPDATE DAMAGE VARIABLE
C
              ALPHA1=ALPHA0+LAM
C     ------------------------------------------------------------------
C
C             UPDATE DAMAGE AND HARDENING FUNCTION
C
              FA1=EXP(-ALPHA1/ALPHAF)
```

```
               DFA1=-1.0D0/ALPHAF*EXP(-ALPHA1/ALPHAF)
               GA1=GMAX*(1-EXP(-ALPHA1/ALPHAG))+YSIG
               DGA1=GMAX/ALPHAG*EXP(-ALPHA1/ALPHAG)
C        ----------------------------------------------------------------
C
C          FINAL STRESS PRIME SSD
C
               DO 160 K1=1,NTENS
                 SSD(K1)=STRD(K1)*FA1*GA1/(FA0*(GA1+LAM*FA1))
  160          CONTINUE
C        ----------------------------------------------------------------
C
C          UPDATE PLASTIC STRAIN
C
C          SUBROUTINE FOR TEMP1(NTENS)=E'S'
               CALL MATVEC(EEED,SSD,TEMP1,NTENS)
C
               DO 161 K1=1,NTENS
                 EPLAS1(K1)=EPLAS0(K1)+LAM*TEMP1(K1)/GA1
  161          CONTINUE
C        ----------------------------------------------------------------
C
C          UPDATE ELASTIC STRAIN
C
               DO 170 K1=1,NTENS
                 EELAS1(K1)=ETOT1(K1)-EPLAS1(K1)
  170          CONTINUE
C        ----------------------------------------------------------------
C
C          UPDATE TOTAL STRESS
C
               DO 190 K1=1,NTENS
                 FACTOR=0.0D0
                 DO 180 K2=1,NTENS
                   FACTOR=FACTOR+SSSC(K1,K2)*(ETOT1(K2)-EPLAS1(K2))
     1                   +FA1*SSSD(K1,K2)*(ETOT1(K2)-EPLAS1(K2))
  180            CONTINUE
                 SS1(K1)=FACTOR
  190          CONTINUE
C        ----------------------------------------------------------------
C
C          CONSISTENT TANGENT STIFFNESS OPERATOR MATRIX DDSDDE
C
               TEMP2=0.0D0
C          SUBROUTINE FOR TEMP1(NTENS)=E'S
               CALL MATVEC(EEED,SS1,TEMP1,NTENS)
C          SUBROUTINE FOR TEMP2=S:E'SC
               CALL SCALPROD(SS1,TEMP1,TEMP2,NTENS)
C          SUBROUTINE FOR DYADIC PRODUCT TEMP3=E'S ox E'S
               CALL VECDYAD(TEMP1,TEMP1,TEMP3,NTENS)
```

```
C
C           GRADIENT dYi/dS
C
            DO 90 K1=1,NTENS
              DO 80 K2=1,NTENS
                DSYY0(K1,K2)=EEEC(K1,K2)+EEED(K1,K2)/FA1+LAM
     1                      *(EEED(K1,K2)*ABS(TEMP2)-TEMP3(K1,K2))
     2                      /(SQRT(ABS(TEMP2*TEMP2*TEMP2)))
 80           CONTINUE
 90         CONTINUE
C
C           SUBROUTINE FOR DSYY0I=INVERSE(DSYY0)
            CALL MIGS(DSYY0,NTENS,DSYY0I)
C
C           SUBROUTINES FOR TEMP5=DSYY0I*(E'S ox E'S)*DSYY0I
            CALL MULTAB(TEMP3,DSYY0I,TEMP4,NTENS)
            CALL MULTAB(DSYY0I,TEMP4,TEMP5,NTENS)
C
C           SUBROUTINES FOR TEMP7=E'S:DSYY0I*E'S
            TEMP7=0.0D0
            CALL MATVEC(DSYY0I,TEMP1,TEMP6,NTENS)
            CALL SCALPROD(TEMP1,TEMP6,TEMP7,NTENS)
C
            DO 210 K1=1,NTENS
              DO 200 K2=1,NTENS
                TANM(K1,K2)=DSYY0I(K1,K2)-TEMP5(K1,K2)/(TEMP7+
     1                      (FA1*FA1)/(FA1*FA1-DFA1)*GA1
     2                      *SQRT(ABS(TEMP2)))
 200          CONTINUE
 210        CONTINUE
C
      ENDIF

C     ----------------------------------------------------------------
C
C     CONVERT TANGENT STIFFNESS OPERATOR MATRIX TO ABAQUS CONVENTION
C
      DO K1=4,6
        DO K2=4,6
          TANM(K1,K2)=TANM(K1,K2)/2.0D0
          TANM(K1-3,K2)=TANM(K1-3,K2)/SQRT(2.0D0)
          TANM(K1,K2-3)=TANM(K1,K2-3)/SQRT(2.0D0)
        ENDDO
      ENDDO
C     ----------------------------------------------------------------
C
C     CONVERT STRESSES AND STRAINS TO ABAQUS CONVENTION
C
      DO K1=4,6
        EELAS1(K1)=EELAS1(K1)*SQRT(2.0D0)
```

```
         EPLAS1(K1)=EPLAS1(K1)*SQRT(2.0D0)
         SS1(K1)=SS1(K1)/SQRT(2.0D0)
       ENDDO
C      ------------------------------------------------------------------
C
C      UPDATE OF FIELD VARIABLES
C
       DO K1=1,NTENS
 STRESS(K1)=SS1(K1)
 STATEV(K1)=EELAS1(K1)
         STATEV(K1+NTENS)=EPLAS1(K1)
       ENDDO
C
       DO 230 K1=1,NTENS
         DO 220 K2=1,NTENS
           DDSDDE(K1,K2)=TANM(K1,K2)
 220     CONTINUE
 230   CONTINUE
C
       STATEV(13)=ALPHA1
C
       RETURN
       END
C      -------------------------------------------------------------------
C
C      SUBROUTINES FOR MATRIX CALCULATION
C      -------------------------------------------------------------------
C
       SUBROUTINE MULTAB(A,B,X,N)
C      MULTIPLIES A AND B WITH DIMENSION N*N
       INCLUDE 'ABA_PARAM.INC'
       DIMENSION A(N,N),B(N,N),X(N,N)
       DO I=1,N
         DO J=1,N
           RCSUM=0.0D0
           DO K=1,N
             RCSUM=RCSUM+A(I,K)*B(K,J)
           END DO
           X(I,J)=RCSUM
         END DO
       END DO
       RETURN
       END
C
C      -------------------------------------------------------------------
C
       SUBROUTINE MATVEC(A,C,X,N)
C      PRODUCT OF VECTOR C AND MATRIX A WITH DIMENSION N*N
       INCLUDE 'ABA_PARAM.INC'
       DIMENSION A(N,N),X(N),C(N)
```

89

```
          DO I=1,N
             RCSUM=0.0D0
             DO J=1,N
                RCSUM=RCSUM+A(I,J)*C(J)
             END DO
             X(I)=RCSUM
          END DO
          RETURN
          END
C
C     ------------------------------------------------------------------
C
      SUBROUTINE VECDYAD(A,B,X,N)
C     DYADIC PRODUCT AB' OF VECTORS A AND B WITH DIMENSION N*1
      INCLUDE 'ABA_PARAM.INC'
      DIMENSION A(N),B(N),X(N,N)
      DO I=1,N
         DO J=1,N
            X(I,J)=A(I)*B(J)
         END DO
      END DO
      RETURN
      END
C
C     ------------------------------------------------------------------
C
      SUBROUTINE SCALPROD(A,B,X,N)
C     SCALAR PRODUCT OF 2 VECORS A AND B WITH DIMENSION N
      INCLUDE 'ABA_PARAM.INC'
      DIMENSION B(N)
      DOUBLE PRECISION X,A(N)
C
      X=0.0
      DO 240 I=1,N
       X=X+A(I)*B(I)
 240  CONTINUE
      RETURN
      END
C
C     ------------------------------------------------------------------
C
C ****************************************************************
C
      SUBROUTINE MIGS(A,N,X)
C
C Subroutine to invert matrix A(N,N) with the inverse stored
C in X(N,N) in the output. A is stored in STOA and is resituted
C as outpout
C
      INCLUDE 'ABA_PARAM.INC'
```

90

```fortran
      DOUBLE PRECISION A(N,N),STOA(N,N),B(N,N),X(N,N)
      INTEGER INDX(N)
C
      DO 140 I=1,N
        DO 130 J=1,N
          STOA(I,J)=A(I,J)
          B(I,J)=0.0D0
  130   CONTINUE
  140 CONTINUE
      DO 150 I=1,N
        B(I,I)=1.0D0
  150 CONTINUE
C
      CALL ELGS(A,N,INDX)
C
      DO 180 I=1,N-1
        DO 170 J=I+1,N
          DO 160 K=1,N
            B(INDX(J),K)=B(INDX(J),K)
    1                    -A(INDX(J),I)*B(INDX(I),K)
  160     CONTINUE
  170   CONTINUE
  180 CONTINUE
C
      DO 210 I=1,N
        X(N,I)=B(INDX(N),I)/A(INDX(N),N)
        DO 200 J=N-1,1,-1
          X(J,I)=B(INDX(J),I)
          DO 190 K=J+1,N
            X(J,I)=X(J,I)-A(INDX(J),K)*X(K,I)
  190     CONTINUE
          X(J,I)= X(J,I)/A(INDX(J),J)
  200   CONTINUE
  210 CONTINUE
C
C Restitution of A
      DO 230 I=1,N
        DO 220 J=1,N
          A(I,J)=STOA(I,J)
  220   CONTINUE
  230 CONTINUE
C
      RETURN
      END
C
C *************************************************************
C
      SUBROUTINE ELGS(A,N,INDX)
C
C Subroutine to perform the partial-pivoting Gaussian elimination.
```

```fortran
C A(N,N) is the original matrix in the input and transformed
C matrix plus the pivoting element ratios below the diagonal in
C the output.  INDX(N) records the pivoting order.
C
      INCLUDE 'ABA_PARAM.INC'
      DOUBLE PRECISION A(N,N),C(N)
      INTEGER INDX(N)
      DOUBLE PRECISION C1,PI1,PI,PJ
      INTEGER K,ITMP
C
C Initialize the index
C
      DO 240 I=1,N
        INDX(I)=I
  240 CONTINUE
C
C Find the rescaling factors, one from each row
C
        DO 260 I=1,N
          C1=0.0D0
          DO 250 J=1,N
            C1=DMAX1(C1,ABS(A(I,J)))
  250     CONTINUE
          C(I)=C1
  260   CONTINUE
C
C Search the pivoting (largest) element from each column
C
      DO 300 J=1,N-1
        PI1=0.0D0
        DO 270 I=J,N
          PI=ABS(A(INDX(I),J))/C(INDX(I))
          IF (PI.GT.PI1) THEN
            PI1=PI
            K=I
          ELSE
          ENDIF
  270   CONTINUE
C
C Interchange the rows via INDX(N) to record pivoting order
C
        ITMP=INDX(J)
        INDX(J)=INDX(K)
        INDX(K)=ITMP
        DO 290 I=J+1,N
          PJ=A(INDX(I),J)/A(INDX(J),J)
C
C Record pivoting ratios below the diagonal
C
          A(INDX(I),J)=PJ
```

92

```
C
C Modify other elements accordingly
C
          DO 280 K=J+1,N
            A(INDX(I),K)=A(INDX(I),K)-PJ*A(INDX(J),K)
  280     CONTINUE
  290   CONTINUE
  300 CONTINUE
C
      RETURN
      END
C
C ****************************************************************
```

Appendix B

Implementation in Mathematica

```
(*UMAT*)

(*Input of F*)

FF = {{1, 0, 0}, {0, 1, 0.12}, {0, 0, 1}}

{{1, 0, 0}, {0, 1, 0.12}, {0, 0, 1}}

MatrixForm[FF]

(*Compliance matrix*)

(*Ashman elastic constants*)

E1 = 12.0

E2 = 13.4

E3 = 20.0

G12 = 4.53

G13 = 5.61

G23 = 6.23

nu12 = 0.376

nu13 = 0.222

nu23 = 0.235

nu21 = 0.422

nu31 = 0.371
```

```
nu32 = 0.350

(*Construction of the Compliance Matrix*)

EEEE = ConstantArray[0, {6, 6}]

EEEE[[1, 1]] = 1/E1

EEEE[[2, 2]] = 1/E2

EEEE[[3, 3]] = 1/E3

EEEE[[2, 1]] = -nu21/E2

EEEE[[1, 2]] = -nu12/E1

EEEE[[3, 1]] = -nu31/E3

EEEE[[1, 3]] = -nu13/E1

EEEE[[3, 2]] = -nu32/E3

EEEE[[2, 3]] = -nu23/E2

EEEE[[4, 4]] = 1/(2*G12)

EEEE[[5, 5]] = 1/(2*G13)

EEEE[[6, 6]] = 1/(2*G23)

MatrixForm[EEEE]

(*Symmetrization of the Compliance Matrix*)

EEEEsym = 0.5*(EEEE + Transpose[EEEE])

{{0.0833333, -0.0314129, -0.018525, 0, 0, 0}, {-0.0314129,
  0.0746269, -0.0175187, 0, 0, 0}, {-0.018525, -0.0175187, 0.05, 0, 0, 0}, {0,
   0, 0, 0.110375, 0, 0}, {0, 0, 0, 0, 0.0891266, 0}, {0, 0, 0, 0, 0,
  0.0802568}}

MatrixForm[EEEEsym]

(*Eigenvalue and Eigenvector analysis of the Compliance Matrix*)

Eigenvalues[EEEEsym]

Eigenvectors[EEEEsym]
```

```
{valsE, vecsE} = Eigensystem[EEEEsym]

{{0.110813, 0.110375, 0.0891266, 0.0802568, 0.0739607,
  0.0231865}, {{0.76578, -0.641269, -0.0485406, 0., 0., 0.}, {0., 0., 0., 1.,
   0., 0.}, {0., 0., 0., 0., 1., 0.}, {0., 0., 0., 0., 0.,
   1.}, {-0.415391, -0.550839, 0.723897, 0., 0., 0.}, {0.49095, 0.534182,
   0.688199, 0., 0., 0.}}}

(*Decomposition of the Compliance Matrix*)

(*Constant Part*)

EEEC = valsE[[6]]*dyad[vecsE[[6]], vecsE[[6]]]

{{0.0055887, 0.00608082, 0.00783406, 0., 0., 0.}, {0.00608082,
  0.00661628, 0.0085239, 0., 0., 0.}, {0.00783406, 0.0085239,
  0.0109815, 0., 0., 0.}, {0., 0., 0., 0., 0., 0.}, {0., 0., 0., 0.,
  0., 0.}, {0., 0., 0., 0., 0., 0.}}

MatrixForm[EEEC]

(*Damageable Part*)

EEED = EEEEsym - EEEC

{{0.0777446, -0.0374938, -0.0263591, 0., 0., 0.}, {-0.0374938,
  0.0680106, -0.0260426, 0., 0., 0.}, {-0.0263591, -0.0260426,
  0.0390185, 0., 0., 0.}, {0., 0., 0., 0.110375, 0., 0.}, {0., 0., 0.,
   0., 0.0891266, 0.}, {0., 0., 0., 0., 0., 0.0802568}}

MatrixForm[EEED]

(*Stiffness matrix*)

SSSSsym = Inverse[EEEEsym]

{{18.0203, 9.97294, 10.1708, 0., 0., 0.}, {9.97294, 20.1202, 10.7446,
  0., 0., 0.}, {10.1708, 10.7446, 27.5329, 0., 0., 0.}, {0., 0., 0.,
  9.06, 0., 0.}, {0., 0., 0., 0., 11.22, 0.}, {0., 0., 0., 0., 0.,
  12.46}}

MatrixForm[SSSSsym]

(*Eigenvector and Eigenvalue analysis of the Stiffness Matrix*)

Eigenvectors[SSSSsym]

Eigenvalues[SSSSsym]

{valsS, vecsS} = Eigensystem[SSSSsym]
```

```
{{43.1285, 13.5207, 12.46, 11.22, 9.06,
  9.02421}, {{-0.49095, -0.534182, -0.688199, 0., 0.,
   0.}, {-0.415391, -0.550839, 0.723897, 0., 0., 0.}, {0., 0., 0., 0., 0.,
   1.}, {0., 0., 0., 0., 1., 0.}, {0., 0., 0., 1., 0.,
   0.}, {0.76578, -0.641269, -0.0485406, 0., 0., 0.}}}
```

(*Decomposition of the Stiffness Matrix*)

(*Constant Part*)

SSSC = valsS[[1]]*dyad[vecsS[[1]], vecsS[[1]]]

```
{{10.3954, 11.3107, 14.5719, 0., 0., 0.}, {11.3107, 12.3067, 15.855,
  0., 0., 0.}, {14.5719, 15.855, 20.4264, 0., 0., 0.}, {0., 0., 0.,
  0., 0., 0.}, {0., 0., 0., 0., 0., 0.}, {0., 0., 0., 0., 0., 0.}}
```

MatrixForm[SSSC]

(*Damageable Part*)

SSSD = SSSSsym - SSSC

```
{{7.62495, -1.33781, -4.40111, 0., 0., 0.}, {-1.33781,
  7.81349, -5.11049, 0., 0., 0.}, {-4.40111, -5.11049, 7.10646, 0.,
  0., 0.}, {0., 0., 0., 9.06, 0., 0.}, {0., 0., 0., 0., 11.22,
  0.}, {0., 0., 0., 0., 0., 12.46}}
```

MatrixForm[SSSD]

(*DEFINITIONS UMAT*)

(*Computation YSIG*)

SSmax = {0.0, 0.0, 0.115265, 0.0, 0.0, 0.0}

{0., 0., 0.115265, 0., 0., 0.}

TEMP1 = EEED.SSmax

{-0.00303828, -0.0030018, 0.00449746, 0., 0., 0.}

TEMP2 = SSmax.TEMP1

0.0005184

YSIG = Sqrt[TEMP2]

0.0227684
```

```
(*Material Parameters*)

ALPHAF = 0.098979291

0.0989793

GMAX = 0.010751744

0.0107517

ALPHAG = 0.026246905

0.0262469

(*Definition of damage and plastic hardening function*)

FA[alpha_] = Exp[-alpha/ALPHAF]

E^(-10.1031 alpha)

FA'[alpha]

-10.1031 E^(-10.1031 alpha)

GA[alpha_] = YSIG + GMAX*(1 - Exp[-alpha/ALPHAG])

0.0227684 + 0.0107517 (1 - E^(-38.0997 alpha))

GAid[alpha_] = YSIG

0.0227684

GAlin[alpha_] = YSIG + 0.1*alpha

0.0227684 + 0.1 alpha

GA'[alpha]

0.409639 E^(-38.0997 alpha)

(*Definition yield criterion*)

y0[alpha_, SS_] = Sqrt[SS.(EEED.SS)] - GA[alpha]

(*Computation of Strain*)

GG = FF - IdentityMatrix[3]

{{0, 0, 0}, {0, 0, 0.12}, {0, 0, 0}}
```

```
NINC = 200

GGINC = 4*GG/NINC

{{0, 0, 0}, {0, 0, 0.0024}, {0, 0, 0}}

(*Table initialization*)

EPLAS1 = {0.0, 0.0, 0.0, 0.0, 0.0, 0.0}

ALPHA = 0.0

SS11 = ConstantArray[0, NINC]

LE11 = ConstantArray[0, NINC]

SS22 = ConstantArray[0, NINC]

LE22 = ConstantArray[0, NINC]

SS33 = ConstantArray[0, NINC]

LE33 = ConstantArray[0, NINC]

SS12 = ConstantArray[0, NINC]

LE12 = ConstantArray[0, NINC]

SS13 = ConstantArray[0, NINC]

LE13 = ConstantArray[0, NINC]

SS23 = ConstantArray[0, NINC]

LE23 = ConstantArray[0, NINC]

AL = ConstantArray[0, NINC]

DAM = ConstantArray[0, NINC]

yi = ConstantArray[0, NINC]

(*SINGLE ELEMENT TEST*)

For[i = 1, i < NINC, i++,
 If[i <= NINC/2, j = i, j = NINC - i];
 FF1 = IdentityMatrix[3] + GGINC*j;
 CC1 = Transpose[FF1].FF1;
 {valsC1, vecsC1} = Eigensystem[CC1];
 lnU1 = Sum[Log[Sqrt[valsC1[[i]]]]*dyad[vecsC1[[i]], vecsC1[[i]]], {i, 1, 3}];
```

```
ETOT1 = {lnU1[[1, 1]], lnU1[[2, 2]], lnU1[[3, 3]], Sqrt[2.0]*lnU1[[1, 2]],
  Sqrt[2.0]*lnU1[[1, 3]], Sqrt[2.0]*lnU1[[2, 3]]};
FF0 = IdentityMatrix[3] + GGINC*(i - 1);
CC0 = Transpose[FF0].FF0;
{valsC0, vecsC0} = Eigensystem[CC0];
lnU0 = Sum[Log[Sqrt[valsC0[[i]]]]*dyad[vecsC0[[i]], vecsC0[[i]]], {i, 1, 3}];
ETOT0 = {lnU0[[1, 1]], lnU0[[2, 2]], lnU0[[3, 3]], Sqrt[2.0]*lnU0[[1, 2]],
  Sqrt[2.0]*lnU0[[1, 3]], Sqrt[2.0]*lnU0[[2, 3]]};
EPLAS0 = EPLAS1;
ALPHA0 = ALPHA;
SSIN = SSSC.(ETOT0 - EPLAS0) + FA[ALPHA0]*SSSD.(ETOT0 - EPLAS0);
STR = SSSC.(ETOT1 - EPLAS0) + FA[ALPHA0]*SSSD.(ETOT1 - EPLAS0);
STRD = FA[ALPHA0]*SSSD.(ETOT1 - EPLAS0);
ystr = y0[ALPHA0, STR];
If[ystr <= 0.0,
 SS1 = STR; EPLAS1 = EPLAS0; ALPHA = ALPHA0,
 LAM = 0.0;
 DLAM = 0.01;
 While[DLAM > 0.000000000001,
  h0 = (Sqrt[STRD.(EEED.STRD)] - LAM*FA[ALPHA0])*FA[ALPHA0 + LAM] -
    FA[ALPHA0]*GA[ALPHA0 + LAM];
  dh0 = (Sqrt[STRD.(EEED.STRD)] - LAM*FA[ALPHA0])*FA'[ALPHA0 + LAM] -
    FA[ALPHA0]*FA[ALPHA0 + LAM] - FA[ALPHA0]*GA'[ALPHA0 + LAM];
  DLAM = -h0/dh0;
  LAM = LAM + DLAM;
  ];
 ALPHA = ALPHA0 + LAM;
 SSD = STRD*(GA[ALPHA]*FA[ALPHA])/(FA[ALPHA0]*(GA[ALPHA] + LAM*FA[ALPHA]));
 EPLAS1 = EPLAS0 + LAM/GA[ALPHA]*(EEED.SSD);
 SS1 = SSSC.(ETOT1 - EPLAS1) + FA[ALPHA]*SSSD.(ETOT1 - EPLAS1);
 ];
SS11[[i]] = SS1[[1]];
LE11[[i]] = ETOT1[[1]];
SS22[[i]] = SS1[[2]];
LE22[[i]] = ETOT1[[2]];
SS33[[i]] = SS1[[3]];
LE33[[i]] = ETOT1[[3]];
SS12[[i]] = SS1[[4]]/Sqrt[2.0];
LE12[[i]] = ETOT1[[4]]/Sqrt[2.0];
SS13[[i]] = SS1[[5]]/Sqrt[2.0];
LE13[[i]] = ETOT1[[5]]/Sqrt[2.0];
SS23[[i]] = SS1[[6]]/Sqrt[2.0];
LE23[[i]] = ETOT1[[6]]/Sqrt[2.0];
DAM[[i]] = FA[ALPHA];
AL[[i]] = ALPHA;
yi[[i]] = y0[ALPHA, SS1]
]
```

Bibliography

[ACBR84]   R.B. Ashman, S.C. Cowin, W.C. Van Buskirk, and J.C. Rice. A continuous wave technique for the measurement of the elastic properties of cortical bone. *Journal of Biomechanics*, 17(5):349 – 361, 1984.

[BP98]   A. Bolshakov and G.M. Pharr. Influences of the pileup on the measurement of mechanical properties by load and depth sensing indentation techniques. *Journal of Material Research*, 13:1049–1058, 1998.

[COZC07]   Xi Chen, Nagahisa Ogasawara, Manhong Zhao, and Norimasa Chiba. On the uniqueness of measuring elastoplastic properties from indentation: The indistinguishable mystical materials. *Journal of the Mechanics and Physics of Solids*, 55(8):1618 – 1660, 2007.

[DCVV$^+$01] M. Dao, N. Chollacoop, K. J. Van Vliet, T. A. Venkatesh, and S. Suresh. Computational modeling of the forward and reverse problems in instrumented sharp indentation. *Acta Materialia*, 49(19):3899–3918, November 2001.

[FZ09]   G. Franzoso and P. K. Zysset. Elastic anisotropy of human cortical bone secondary osteons measured by nanoindentation. *Journal of Biomechanical Engineering*, 131, 2009.

[HBP99]   J.C. Hay, A. Bolshakov, and G.M. Pharr. A critical examination of the fundamental relations used in the analysis of nanoindentation data. *Journal of Material Research*, 14:2296–2305, 1999.

[HGZG05]   C. Edward Hoffler, X. Edward Guo, Philippe K. Zysset, and Steven A. Goldstein. An application of nanoindentation technique to measure bone tissue lamellae properties. *J. Biomech. Eng.*, 127(7):1046–1053, December 2005.

[Hil98]   R. Hill. *The mathematical theory of plasticity.* Oxford University Press, 1998.

[Kri91]   R.V. Kristic. *Human Microscopic Anatomy.* Springer, 1991.

[MBM09]   L.P. Mullins, M.S. Bruzzi, and P.E. McHugh. Calibration of a constitutive model for the post-yield behaviour of cortical bone. *Journal of the Mechanical Behavior of Biomedical Materials*, 2(5):460–470, October 2009.

[OP92]   W.C. Oliver and G.M. Pharr. An improved technique for determining hardness and elastic modulus using load and displacement sensing indentation experiments. *Journal of Material Science*, 7:1564–1583, 1992.

[PRR08a]   B. Poon, D. Rittel, and G. Ravichandran. An analysis of nanoindentation in elasto-plastic solids. *International Journal of Solids and Structures*, 45(25-26):6399–6415, December 2008.

[PRR08b]   B. Poon, D. Rittel, and G. Ravichandran. An analysis of nanoindentation in linearly elastic solids. *International Journal of Solids and Structures*, 45(24):6018–6033, December 2008.

[Sne48]   Ian N. Sneddon. Boussinesq's problem for a rigid cone. *Mathematical Proceedings of the Cambridge Philosophical Society*, 44(04):492–507, 1948.

[SP01]   J. G. Swadener and G. M. Pharr. Indentation of elastically anisotropic half-spaces by cones and parabolae of revolution. *Philosophical Magazine A*, 81(2):447–466, 2001.

[ZC95]   P. K. Zysset and A. Curnier. An alternative model for anisotropic elasticity based on fabric tensors. *Mechanics of Materials*, 21(4):243 – 250, 1995.

[ZEGEH+99] Philippe K. Zysset, X. Edward Guo, C. Edward Hoffler, Kristin E. Moore, and Steven A. Goldstein. Elastic modulus and hardness of cortical and trabecular bone lamellae measured by nanoindentation in the human femur. *Journal of Biomechanics*, 32(10):1005–1012, October 1999.

[ZMKO10]   Jingzhou Zhang, Michelle M. Michalenko, Ellen Kuhl, and Timothy C. Ovaert. Characterization of indentation response and stiffness reduction of bone using a continuum damage model. *Journal of the Mechanical Behavior of Biomedical Materials*, 3(2):189–202, February 2010.

[ZNO08]   Jingzhou Zhang, Glen L. Niebur, and Timothy C. Ovaert. Mechanical property determination of bone through nano- and micro-indentation testing and finite element simulation. *J Biomech*, 41(2):267–275, January 2008.

[Zys94]   Philippe K. Zysset. *A Constitutive Law for Trabecular Bone*. PhD thesis, Ecole Polytechnique Federale de Lausanne, 1994.

[Zys09]   P.K. Zysset. Indentation of bone: a short review. *Osteoporos Int*, 20:1049–1055, 2009.